# LABORATORY STUDY INVESTIGATING THE THREE-DIMENSIONAL TURBULENCE AND KINEMATIC PROPERTIES ASSOCIATED WITH A BREAKING SOLITARY WAVE

A Thesis

by

DAVID TOWNLEY SWIGLER

Submitted to the Office of Graduate Studies of
Texas A&M University
in partial fulfillment of the requirements for the degree of

MASTER OF SCIENCE

August 2009

Major Subject: Ocean Engineering

# LABORATORY STUDY INVESTIGATING THE THREE-DIMENSIONAL TURBULENCE AND KINEMATIC PROPERTIES ASSOCIATED WITH A BREAKING SOLITARY WAVE

A Thesis

by

DAVID TOWNLEY SWIGLER

Submitted to the Office of Graduate Studies of
Texas A&M University
in partial fulfillment of the requirements for the degree of

MASTER OF SCIENCE

Approved by:

| | |
|---|---|
| Chair of Committee, | Dr. Patrick Lynett |
| Committee Members, | Dr. Billy Edge |
| | Dr. Robert Hetland |
| Head of Department, | Dr. David Rosowsky |

August 2009

Major Subject: Ocean Engineering

# ABSTRACT

Laboratory study investigating the three-dimensional turbulence and kinematic
properties associated with a breaking solitary wave. (August 2009)

David Townley Swigler, B.S., University of Florida

Chair of Advisory Committee: Dr. Patrick Lynett

A laboratory experiment was performed to investigate the three-dimensional
turbulence and kinematic properties that develop due to a breaking solitary and an
irregular shallow water bathymetry.  A large basin equipped with a piston-type
wavemaker was used to generate the wave, while the free surface elevations and fluid
velocities were measured using wave gauges and three-dimensional acoustic-Doppler
velocimeters (ADVs), respectively.  From the free surface elevations, the evolution and
runup of the wave was revealed; while from the ADVs, the velocity and turbulent energy
was determined to identify specific turbulent events and coherent structures.

It was found that shoaling was confined to areas with gentler sloping bathymetry
near the basin walls and the runup shoreward of the still water shoreline was not
uniform.  The greatest turbulent events were very well correlated to borefronts where the
greatest shear and fluid accelerations occurred.  Because of an abrupt change in the
bathymetry, a rotating eddy developed characterized by a three-dimensional flow field.

# DEDICATION

To my parents

# ACKNOWLEDGEMENTS

I sincerely thank my advisor, Dr. Patrick Lynett, for his guidance and expertise that he provided throughout the process. He created a great learning environment that allowed me to think independently and solve problems while keeping my efforts within the bounds of the research. I appreciate the time and resources that he made available to me during the study. Without them none of this would have been possible.

I would like to also express my gratitude to my committee members, Dr. Billy Edge and Dr. Robert Hetland, for their advice and knowledge they provided on the subject matter. I appreciate the staff at the O.H. Hinsdale Wave Research Laboratory who contributed countless hours toward completing the experiment in a timely fashion and obtaining good quality data.

Finally, I thank my friends, family, and office mates who supported me throughout the whole process. They motivated and encouraged me when it was critically needed.

# TABLE OF CONTENTS

# LIST OF FIGURES

# 1.0 INTRODUCTION & BACKGROUND

The study and understanding of the kinematic properties and turbulent energy associated with a breaking wave is of particular importance when trying to predict wave forces on structures, nearshore mixing and circulations, sediment transport, and ultimately coastal morphology.  There have been extensive experimental and numerical studies focused on furthering the knowledge of turbulence that develops as waves interact with an underlying bathymetry and break.  By understanding the physics behind the evolution of breaking waves and the development and advection of the turbulent structures near the surf zone, the transport of sediment can be better predicted by numerical models. Currently, numerical models can only give qualitative insight to sediment transport due turbulence, but there is a desire to have them accurately provide quantitative predictions. The goal of this laboratory study was to understand the three-dimensional turbulence and kinematic properties that developed as a solitary wave broke, evolved, and propagated over a complex bathymetry.  It has been shown that the turbulence and flow fields associated with breaking waves are of particular importance since they greatly affect the dynamic equilibrium of beaches (Dalrymple, 1992).

To understand the physics that govern the evolution of waves as they approach a shoreline, extensive experimental studies have been conducted.  The experiments have provided insight to specific phenomena that are known to occur such as shoaling, refraction, breaking, and turbulence, to name a few.  Beginning offshore where the water depth is sufficiently deep and constant, waves are found to be symmetric with respect to

the wave crest (Hsiao et al. 2008) before they began to deform due to interactions with the bathymetry.  Over a sloping bottom, waves begin to become more asymmetric resulting in a steeper front face and an increase in wave height with a decrease in water depth.  This phenomenon is known as shoaling and is directly related to bottom slope where on a gentler slope shoaling is greater as compared to a sufficiently steep slope (Grilli et al., 1994).  At a point when the slope becomes sufficiently steep, Grilli et al. found that the amount of reflection experienced by the incident wave increased causing the increase in wave height to be less noticeable.

Due to shoaling, the asymmetry of the wave reaches a point where it becomes unstable and breaking occurs.  The type of breaking (spilling, plunging, etc.) is greatly dependent on the bottom slope and describes the basic characteristics observed during the breaking process.  Spilling breakers occur on gentler slopes, while plunging breakers occur on steeper more abrupt slopes.   Specifically, plunging breakers are characterized by a very steep wave front and a jet of water to be ejected from the wave crest in the direction of wave propagation.  Lin & Hwung (1992) performed a laboratory experiment and documented that the impinging jet impacts the water surface in front of the wave causing water to be splashed up vertically.  Between the front face of the wave and the impinging jet, a tube of air becomes trapped significantly increasing the amount of air entrained in the water.

The entrained air along with the violent impact of the jet cause significant turbulence to develop within the water column as the flow transitions from irrotational to rotational motion (Ting & Kirby, 1995).   The turbulence, deviations from the mean flow, under a

plunging breaker is much greater as compared to a spilling breaker (Ting & Kirby, 1994) and greatly depends on both the deep-water wave conditions and beach slope (Ting & Kirby, 1995). The turbulent energy is dissipated within one wave cycle and transported landward by the mean flow under a plunging breaker, while under a spilling breaker the turbulent energy is dissipated at a much slower rate and transported seaward (Ting & Kirby, 1994 and 1995). Since plunging breakers (e.g. long period swell waves) transport sediment shoreward causing accretionary beach profiles and spilling breakers (e.g. short period storm waves) transport sediment seaward causing beach erosion, Ting and Kirby suggest that sediment transport is due to the transport of turbulent energy.

Behind the breaking wave crest vertically oriented vortices develop that extend from the water surface to the underlying bathymetry. These vortices are known as obliquely descending eddies (ODEs) and persist for only a short time (Nadaoka et al., 1989). The ODEs are generated by horizontal, spanwise vortices along the breaking wave crest deforming and attaching to the bottom. After attaching, the ODEs appear as pairs counter rotating vertical vortices. Due to their three-dimensionality, they are accompanied with downbursts of turbulent energy at the bottom causing sediment to become suspended (Ting 2006 and 2008).

Although the ODEs last for a short period of time, their three-dimensional flow is interesting because of recent work that reveals the three-dimensional flow field within two-dimensional coherent structures. Two-dimensional structures are characterized has having a lateral width much greater that the flow depth (Negretti et. al, 2005). In general, the flow is described as being uniform with depth given the large difference in

the horizontal and vertical length scales. Shallow water coherent structures are most likely to develop in the presence of strong transverse shear due to fluid flowing past abrupt changes in the bathymetry (Socolofsky & Jirka, 2004). Abrupt changes in the bathymetry can range from submerged reefs, sandbars, inlets, etc. Also, the rotation of the structures is stronger when the shear is created by an unsteady flow as compared to a steady flow (Signell & Geyer, 1991).

The three dimensional flow of coherent structures explains the increased mixing known to occur when they are present. Lin, Ozgoren & Rockwell (2003) identified areas of increased vorticity (vortex rings) over the water depth within the shallow water structures. By generating a coherent structure with flow through a confined orifice, strong transverse shear is present creating a pair of counter rotating vortices. Within the internal flow field of the structures, multiple vortex rings are presented and oriented in planes perpendicular to the coherent structure's axis of rotation. The vortex rings cause the flow field to be characterized by a large amount of three-dimensional turbulence and velocity. The shallow water structure contains secondary flows including upward flow near the center, inward flow near the bottom, and depth varying outward flow over much of the water column. As seen in the field with some tidal flows, strong shear within the water column helps strength these secondary flows (Geyer, 1993).

The phenomena described above were from physical studies which provide the building blocks to understanding the physics governing waves as they approach a shoreline; however, detailed investigation often requires the use of numerical models. The evolution and runup of breaking waves has been modeled extensively to accurately

predict the maximum amplitude and runup of waves as they approach a shoreline. On a sloping beach, Stoker (1957) created the first numerical model using the shallow-water wave equations. Since then, the Lax-Wendroff scheme for wave breaking has been used to model the evolution of a uniform bore over a sloping beach (Hibbert & Peregrine 1979), but the method involved artificial viscosity coefficients. To avoid using artificial coefficients, a non-breaking boundary-element method (BEM) was used and shown to agree with laboratory data, but the computational time for even a small domain was cumbersome (Grilli et al., 1994). Next, a variable grid finite-differences approximation that used the shallow-water wave equations was developed was developed reducing the computational time without (Titov & Synolakis 1995). The drawbacks of this method were that it predicted breaking earlier and predicted smaller maximum runups than observed in laboratory data.

Besides trying to model the evolution and runup of breaking waves, there has been extensive work done on modeling the flows and turbulence that are generated. The most complete approach is direct numerical simulation (DNS), but it is complex and the computational time is not yet realistic. To avoid using DNS, most models require turbulence closure models based on physical processes that are not fully resolved by introducing artificial coefficients. The depth-integrated momentum equations (Bousinesq equations) coupled with an eddy viscosity model and 'roller' model (Schaffer, Madsen, & Deigaard 1993) were used but could not determine spatial distributions of turbulence. A breaking wave model using Reynolds equations with a closure equation for turbulence does not allow complex free surface situations (Johns

1978; Johns & Jefferson 1980). Neglecting all convection processes, a k-equation model was developed using a simplified turbulent kinetic energy k-equation, but later found to overestimate the variation of turbulence vertically within the water column (Deigaard, Fredsoe, & Hedegaard 1986). A Reynolds Averaged Navier-Stokes (RANS) breaking wave model coupling the Reynolds equations with both the k-e turbulence closure model and volume of fluid (VOF) method has been compared to laboratory data and shown to be in good agreement, but still contains artificial coefficients (Lin & Liu 1998). The RANS model using both a k-l turbulence closure model and an eddy viscosity model did not consider air entrainment beneath the breaking wave (Zhao et al. 2004). A Large Eddy Simulation (LES) method which solves the Navier-Stokes equation with a turbulence model to predict turbulence on a subgrid scale was extended to include two-phase flow in order to account for the turbulence generated due to air entrainment (Lubin et al. 2006). Models which attempt to predict the free surface and flows resulting from breaking waves have been adapted and significantly improved over time. By understanding the physics of turbulence generation, the accuracy and reliability of models have evolved, but due to the persisting introduction of artificial terms, laboratory studies are needed to calibrate and verify models.

In this study, the characteristics of a breaking solitary wave will be discussed in order to validate the reliability of the data which could be used in the future when calibrating numerical models. The basin and instrument layouts used in the experiment along with the procedures are described in Sections 2 and 3. The validity of the free surface, velocity, and turbulence measurements is presented in Sections 4 and 5. The

evolution of a single solitary wave over a complex shallow water shelf and the resulting

hydrodynamic are discussed in Section 6 with the use of visual observations, wave

gauge measurements, and velocity measurements.  The refraction of the generated wave

as it encounters shallow water shelf, Section 7, and the resulting runup on a planar

beach, Section 8, reveal the relationship between the various regions of wave evolution

during breaking.  Finally, due to the additional borefronts, a coherent turbulent structure

that developed was identified and is investigated in Section 9 and 10.

# 2.0 SETUP OF LABORATORY EXPERIMENT

## 2.1 Basin Layout

To better understand the turbulence and kinematic properties associated with a breaking solitary wave, a laboratory experiment was conducted recording the free surface elevations and fluid velocities. The experiment was conducted in a large wave basin at Oregon State University's O.H. Hinsdale Wave Research Laboratory which was 48.8m long, 26.5m wide, and 2.1m deep. It was equipped with a piston-type wavemaker powered by an electric motor and a waveboard that consisted of 29 independently functioning paddles which could produce both linear and nonlinear waves up to 0.8 m in height. The walls and underlying bathymetry of the basin were made of concrete to reduce boundary effects due to friction. The coordinate system adopted for the study is the following: X=0 at the wavemaker and increases positively the length of the basin in the direction of wave propagation; Z=0 at the basin floor in the constant depth portion of the basin near the wavemaker and is positive upwards; and Y=0 at the centerline of the basin and is positive parallel to the wavemaker to agree with the right-hand rule.

Opposite the wavemaker, a complex shallow water bathymetry constructed of concrete was built, as shown in Figure 1, to force the generated wave to break symmetrically about the centerline of the basin. First, a 1:30 slope planar beach was constructed which began at X=10.2m and extended to X=31m with a height of 0.95m before becoming level and extending to the back wall of the basin. Second, beginning at

the toe of the planar beach, a three dimensional shallow water shelf was built. In planview, the shelf was triangular in shape with the apex of the triangle closest to the wavemaker and the opposite side flush with the planar beach. The top of the shelf was located at an elevation of Z=0.71m with the apex located at X=12.6m. The sides of the shelf sloped down to the underlying planar beach with the steepest slope being at the apex and becoming milder moving along the shelf edge away from the apex. The shelf edge was defined as the abrupt change in the bathymetry where the shallow water shelf began sloping toward the constant depth portion of the basin.

The still water shoreline (SWS) intersected the planar beach at X=25.75m and the water level was maintained at a depth of 0.78m (Z=0.78m) measured from the constant depth portion of the basin. The bathymetry of the basin, which was constructed with an axis of symmetry about its centerline (Y=0m), produced free surfaces and flows that were symmetric aiding in the deployment of instruments on either side of the centerline with a track mounted bridge spanning the width of the basin.
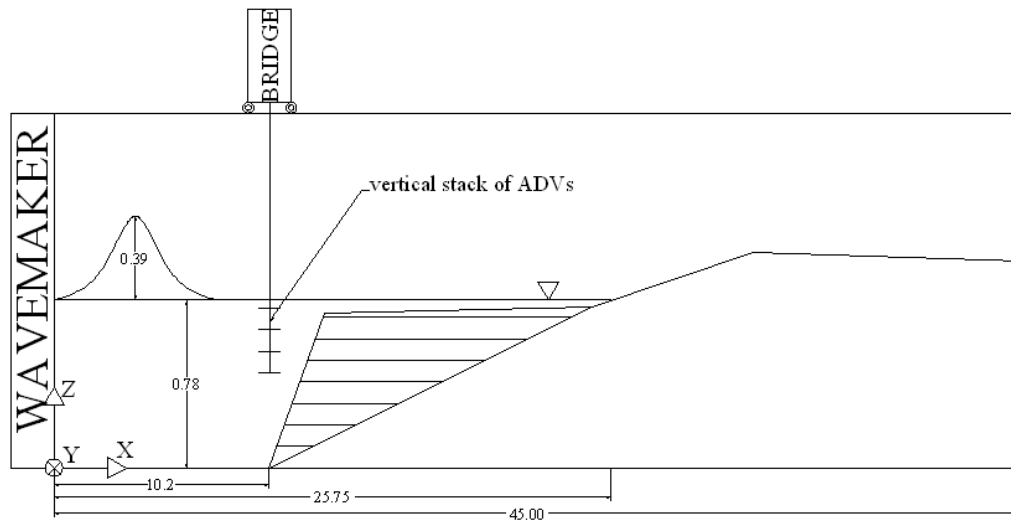
Figure 1: Elevation view of experiment setup. All dimensions are in meters.

## 2.2 Instruments and Layouts

During the experiment, a variety of instruments were used to record the free surface elevation and fluid velocities associated with a breaking solitary wave. Two types of wave gauges were used to measure the free surface, and an acoustic-Doppler velocimeter was used to measure fluid velocities. The data measured by the instruments was recorded by a data acquisition system (DAQ) which allowed measurements to be made at a sampling frequency of 50 Hz over a two minute timeseries. Instruments were mounted to the bottom with brackets and to the bridge which was positioned at various cross-shore locations to allow the basin to be methodically covered and greatly reduce the time required to relocate instruments to new measurement locations. Due to the variety and limited number of instruments available, each type of instrument was deployed separately and moved to various locations within the basin, providing a

detailed representation of the dynamics experienced during the experiment while reducing the impacts to the flow due to the obstructions.

### 2.2.1 Wave Gauges

The wave gauges were used to measure the free surface elevation, allowing the evolution of the solitary wave over the shallow water shelf and up the planar beach to be documented. To do this, two types of wave gauges were required due to the depth of water offshore and onshore of the SWS during the experiment. The two types included resistance-type, wire wave gauges (WG), which were used offshore of the SWS, and ultra sonic wave gauges (usWG), which were used onshore of the SWS.

The WGs consisted of two parallel wires that were mounted to brackets on either end and positioned vertically so that the water surface was situated between the brackets. With the bottom bracket submerged, an electrical circuit was created and the voltage through the wires was measured. As the water level changed, the voltage varied accordingly which was used to create a timeseries of the free surface the WG's location. One issue that had to be taken into consideration was clipping, meaning that the water surface could not rise above the top bracket or drop below the bottom bracket which would break the electrical circuit. The other issue was that careful attention had to be taken while deploying WGs to ensure it did not come in contact with the bathymetry, because this would allow it to become pinned, not be aligned vertically, after wave impacts.

For the study, a total of 14 WGs were used and attached to the bridge. Of the 14 WGs, seven of them were medium in length and seven were long in length, which refers

to the length of the wires and ultimately translates into the range in water level that could be recorded.  The long WGs allowed a greater range of the free surface to be measured and avoid clipping, while the medium WGs were equipped with a thinner bracket on the bottom end which allowed a smaller depth of the water to be measured and avoid clipping.  To completely document the basin's free surface and the symmetry of the wave as it evolved through the basin, the WGs were deployed in two layouts.  For Layout 1, the medium WGs were positioned on the bridge in the longshore direction at Y=-12, -11, -10, -9, -8, -7, and -6m; and the 7 long WGs were positioned at Y=0, 1, 2, 3, 4, 5, and 6m.  For Layout 2, the medium WGs were positioned at Y=-6, -5, -4, -3, -2, -1, and 0m; and the 7 long WGs were at Y=6, 7, 8, 9, 10, 11, and 12m.  For each Layout, the bridge was then positioned at multiple cross-shore locations including X=5, 7.5, 9, 11.5, 13, 15, 17, 19, 21, 23, and 25m by starting near the wavemaker and moving toward SWS.  In total, there were 275 unique WG locations throughout the basin as shown by (✱) in Figure 2.

Once the breaking wave reached the SWS, the usWGs were used to track the runup on the planar beach.  The depth of the runup was very shallow requiring the usWGs, since it would not have been possible to make accurate measurements with the WGs.  Even with the medium WGs equipped with thinner brackets, clipping would have occurred and the runup would have been greatly obstructed.  The usWGs recorded the time required for an emitted acoustic signal to return after being reflected by the water surface of the runup.  From the time, the distance could be determined and ultimately runup could be tracked.  For the experiment, five usWGs were used by positioning them

on the bridge at Y=0, 2, 5, 7, and 10m which was then positioned at X=23, 25, 27, 29, 31, 33, 35, 37, and 39m.  The first two bridge locations of the usWG layout were the same as the last two bridge locations of the WG layouts in order to co-locate the two types of instruments and compare the consistency of the timeseries of the free surface recorded.  In total, there were 45 usWG locations throughout the basin as shown by (◆) in Figure 2.

**2.2.2 Acoustic Doppler Velocimeters**

To measure the fluid velocities, eleven Nortek Vectrino 3D acoustic-Doppler velocimeters (ADV) were employed to record all three components of velocity ($U$, $V$ and $W$) simultaneously.  The ADVs worked by sending out an acoustic signal and measuring the time required for the signal to return after being reflected by particles in the water within its field-of-view.  By sending the signal out repeatedly, the Doppler shift of the particles was determined and ultimately the ADV could calculate the velocity of the fluid in all three directions.  Inherently, with this type of measurement, part of the signal became scattered by other particles in the water and introduced some level of uncertainty known as noise.  To provide some insight into the level of noise associated with data, the ADV also measured the amount of scatter which was used to identify unreliable data.

Two variations of ADVs were used to accommodate the wide range of flow depths that were measured.  Offshore of the shelf edge where the water depth was sufficiently deep, "downlooking" ADVs mounted to the bridge in vertical stacks were used.  On top of the shelf where the water depth was generally shallow, "sidelooking"

ADVs individually mounted to the basin bottom were used. The variations of the ADVs differed due to the orientation of the sensor's field-of-view with respect to its housing. The sensor's field-of-view on the "downlooking" ADV was in line with ADV's housing, while the field-of-view on the "sidelooking" ADV was at a right angle to the housing. The "downlooking" ADVs were arranged in two vertical stacks of four so that the housings were parallel to the water surface and the "sidelooking" ADVs were attached to brackets that were individually mounted to the bathymetry so that the housings were perpendicular to the water surface.

In total, eight of the ADVs were used in the two vertical stacks to obtain the vertical profile of the water column as shown hanging from the bridge in Figure 1. On the vertical stacks, the ADVs were spaced 10cm apart and were positioned in the water so that the uppermost submerged ADV was about 5 cm below the water surface. As the vertical stacks were positioned closer to the shelf, the water depth due to the bathymetry became shallower and did not allow all of the ADVs on the stack to be completely submerged. At those locations, the stacks were positioned as close to the bathymetry surface as possible without touching. The three remaining ADVs were mounted to the bathymetry on or near the shelf.

Due to the limited number of instruments, the ADVs were deployed in five configurations consisting of both the vertical stacks and bottom mounts. For Configuration #1, the bridge was located at X=9m with the vertical stacks mounted at Y=0 and 3m, while the bottom mounted ADVs were located at X=13m, Y=0m and X=15m, Y=-2m. For Configuration #2, the bridge was located at X=9m with the

vertical stacks mounted at Y=6 and 9m, while the bottom mounted ADVs were located at X=15m, Y=0m and X=17m, Y=-2m.  For Configuration #3, the bridge was located at X=11.5m with the vertical stacks mounted at Y=3 and 6m, while the bottom mounted ADVs were located at X=17m, Y=0m and X=17m, Y=-5m and X=17m, Y=-9m.  Unique to this configuration, the vertical stacks of ADVs were also positioned vertically within the water column so that the uppermost submerged ADVs were at the water surface providing an additional eight ADV measurement locations for Configuration #3.  For Configuration #4, the bridge was located at X=15m with the vertical stacks mounted at Y=6 and 9m, while the bottom mounted ADVs were located at X=21m, Y=0m and X=21m, Y=-2m.  For Configuration #5, the bridge was located at X=17m with the vertical stacks mounted at Y=9 and 12m, while the bottom mounted ADVs where located at X=21m, Y=-5m and X=21m, Y=-9m.  In total, there were 59 ADV locations throughout the basin as shown by the 21 (●) in Figure 2.  In other words, the eleven bottom mounted ADVs were located at locations where X≥13m and Y≤0m, while the other ten locations offshore of the shelf edge represent the vertically stacked bridge mounted ADVs.
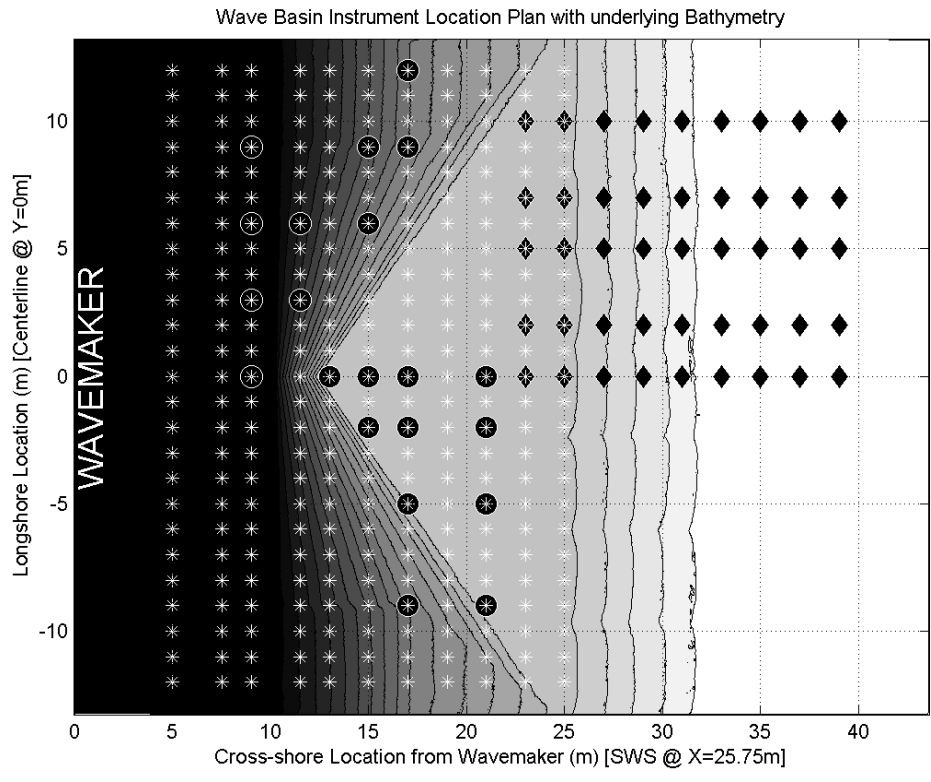
Figure 2:  ADV (●), WG (✳), and usWG (◆) instrument location plan with bathymetry.

# 3.0 EXPERIMENT PROCEDURE

For each trial of the experiment, a single solitary wave, 0.39m in height, was generated so that it propagated over the shallow water shelf to create a strongly plunging breaker. The combination of the symmetrical bathymetry and the drastic reduction in water depth on the shelf caused the wave to begin breaking violently as a plunging breaker just onshore of the shelf apex and extend laterally to the basin side wall as the wave traveled further onshore.

When the data was recorded, the wave heights and fluid velocities were measured separately, with the same initial conditions, in order to keep the quality of data collected unaffected due to the basin's dense population of instruments. For each type of measurement device, multiple trials were conducted to ensure the consistency of the data. A trial consisted of generating a single wave with the wavemaker and recording data using the DAQ for approximately two minutes. This helped to ensure that the dynamics of the basin, due to the various borefronts that developed, were sufficiently documented. After each trail, the basin was allowed to calm for about 35 minutes before another wave was generated. During this down time, the water level was maintained at 0.78m ±0.003m and the large circulations that developed had time to diminish. Also during the down time, the flat part of the beach, which intersected with the basin back wall opposite of the wavemaker, was slightly angled causing water from the runup to accumulate and drain slowly. As a result, the water had to be swept off toward the shelf

between trials to ensure that the large circulations would not persist due to the water draining along the basin side walls.

For both the WGs and usWGs, two trials were run for each location to confirm the consistency of the timeseries, as well as the repeatability of the waves generated by the wavemaker. For the ADVs, it was decided that a minimum of 20 trials were required to provide enough data to reliably quantify the turbulence and kinematic properties that were of interest. While the ADVs were deployed, the basin had to be mixed with regular waves and/or seeding particles added at the discretion of the investigators in order to keep the water evenly distributed with the particles during the down time. The seeding particles, which consisted of fine clays that were naturally in the basin and glass seeding particles that were added at the discretion of the investigator, were necessary to improve the reliability of the return signals that the ADVs used to determine the velocity of the fluid. Mixing the basin with regular waves for approximately one minute created multiple breaking waves offshore of the shelf that were characterized with more intense currents and circulations as compared to the solitary wave generated for the experiment.

# 4.0 WAVE MEASUREMENTS

After averaging the two timeseries obtained at each WG, the timeseries were compared to confirm the assumption that the wave generated by the wavemaker was repeatable and its evolution was symmetric about the basin's centerline due to the symmetric bathymetry. Confirming the repeatability was of particular importance because the method chosen to obtain turbulence hinged on the assumption that measurements from multiple trials at a specific location would yield very similar timeseries. The symmetry of the wave was of equal importance, given the assumption made when deploying the instruments that measurements could be taken on either side of the centerline and mirrored to provide a more complete representation of the basin's dynamics.

## 4.1 Repeatability

To confirm the repeatability of the generated solitary wave, the timeseries obtained from the WGs in the longshore direction closest to the wavemaker (X=5m) were analyzed. This cross-shore location was chosen in order to reduce the exposure the wave had to interactions with the basin that might have caused slight variations in the timeseries compared to other locations further shoreward. Only the timeseries from the long WGs at this cross-shore location in the longshore direction (Y=0m thru 12m) were used to assure that clipping did not occur due the large amplitude of the free surface from the generated wave. In total, 28 trials were overlaid in Figure 3 confirming the

assumption that the repeatability of the wave was realistic.  It shows that the measured

wave heights were between 0.36 and 0.38m which was very consistent over 12 meters of

the wave crest and during the multiple trials.  Other features of interest that were

revealed by the figure included the leading wave (around 1.3 seconds) followed by a

trough (around 3.0 seconds) and a secondary wave (around 3.8 seconds), which will be

discussed later.
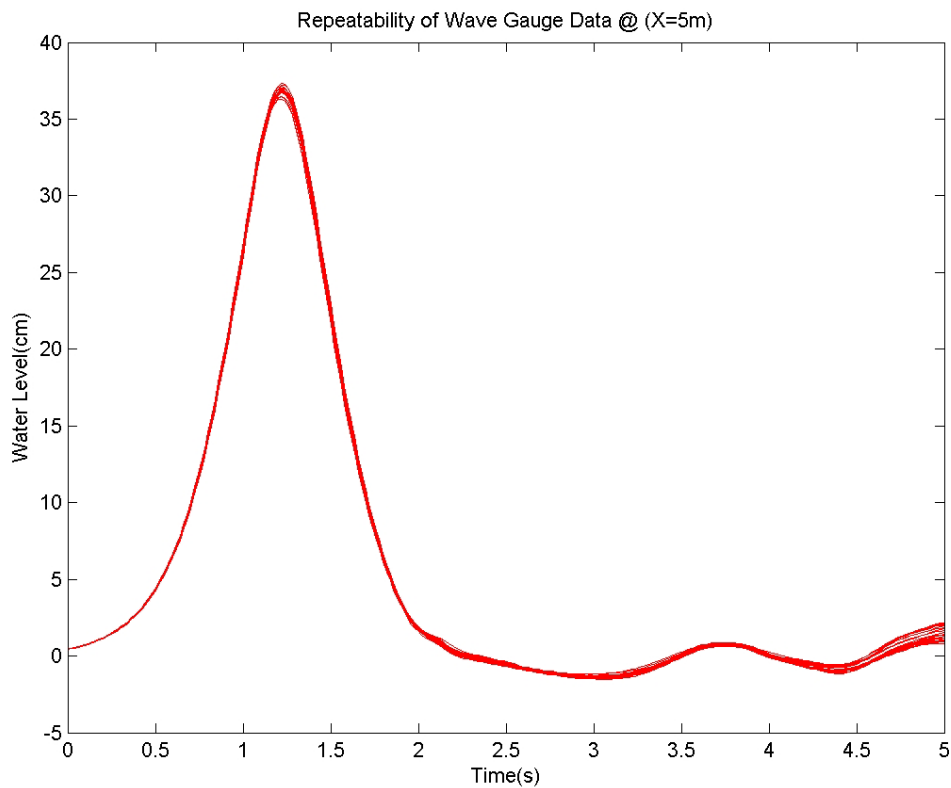


Figure 3:  WG repeatability from long WG located at X=5m.

**4.2 Symmetry**

The second assumption that the wave was symmetric as it evolved and propagated through the basin due to the symmetry of the basin was confirmed by comparing WG timeseries on either side of the centerline. The symmetry of the wave was equally important because in order to portray a more complete presentation of the free surface, turbulence, and kinematic properties during the experiment, the instruments were mirrored about the basin's centerline. For example, based on the length of the WGs and the thickness of the bottom brackets, it was concluded that the long WGs were best for describing the free surface offshore of the shelf edge while the medium WGs were best for describing the free surface shoreward of the shelf edge driving the need to prove the symmetry of the solitary wave. Also, the bridge mounted ADVs positioned at Y≥0m would need to be mirrored to describe the fluid velocities offshore of the shelf edge in relation to the bottom mounted ADVs positioned at Y≤0m.

To validate the symmetry of the wave, the timeseries from the medium and long WGs on respective sides of the centerline were compared. Offshore of the shelf, two pairs of locations were chosen between the toe of the beach and the shelf edge at X=11.5m, Y=±6m and X=13.0m, Y=±8m prior to breaking. The timeseries from these locations were in agreement as shown in Figure 4 and Figure 5, where the line represents the long WG and the dots represent the medium WG. The peak of the generated wave, which occurred at about 5 seconds, and the following disturbances in the free surface were identical. After about 27 seconds, there was some divergence in the timeseries due to the higher wave nonlinearities that were inevitably produced in the basin (Hsiao

2008), but overall the major wave motions were concluded to be similar between the two

WGs on either side of the basin's centerline.
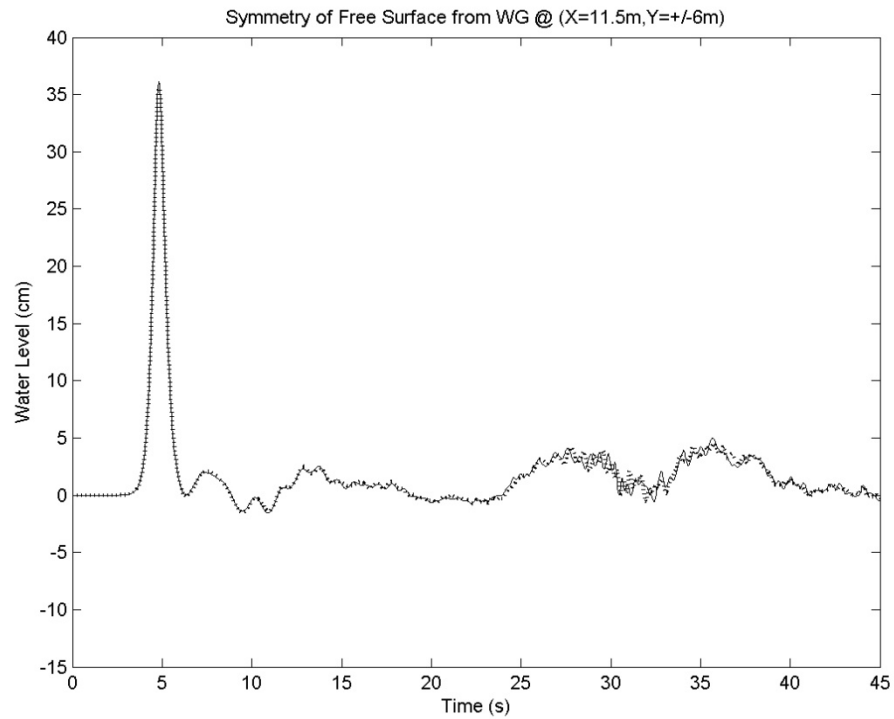


Figure 4:  Symmetry of long WG (line) and medium WG (dots) located at X=11.5, Y=+/-6m.
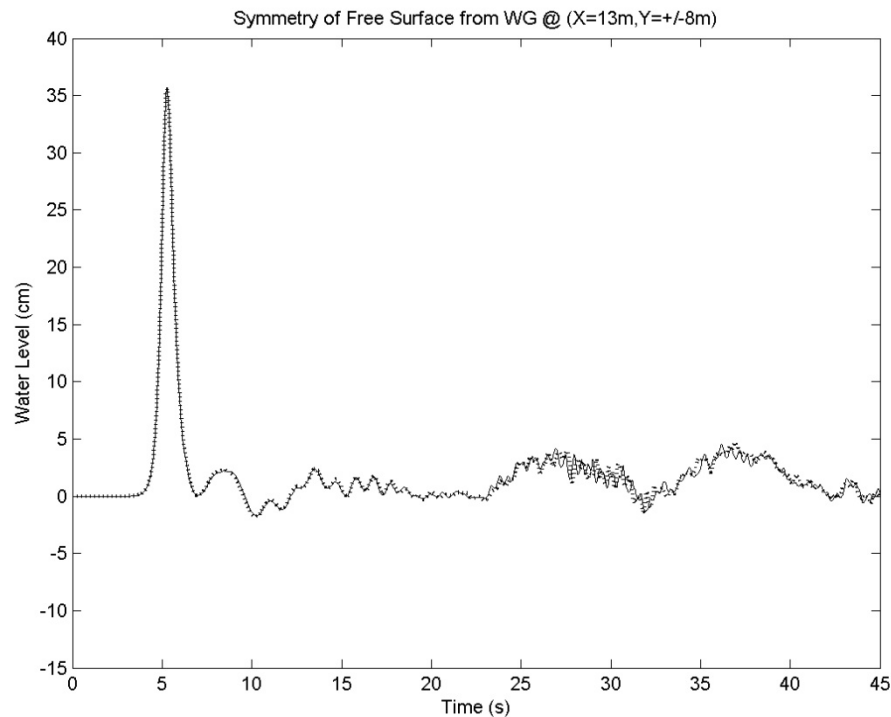
Figure 5:  Symmetry of long WG (line) and medium WG (dots) located at X=13.0, Y=+/-8m.

Onshore of the shelf edge, two pairs of locations were chosen at X=17.0m, Y=+/-1m and X=19.0m, Y=+/-2m to confirm the symmetry of the wave over the shelf after breaking.  Figure 6 and Figure 7 show the close agreement in the timeseries of the long WG represented by the line and the medium WG represented by the dots.  The generated wave in the timeseries appeared completely different, as compared to the offshore locations displayed in Figure 4 and Figure 5, due to its evolution of the wave after breaking.  As the wave passed the WGs, it more closely resembles a bore stretching the width of the shelf and traveling onshore toward the planar beach.

At X=17m in Figure 6, the wave had just broken and water had splashed up due to the jet of water being ejected by the strongly plunging breaker and impacting the water surface in front of the wave (Lin & Hwung, 1992).  The water that splashed up

during the impact was recorded by both of the WGs on either side of the centerline and can be seen as the large spike in the timeseries at about 6.5 seconds. Directly after the spike, the borefront arrived followed by multiple other borefronts. These were observed to develop due to the hydrodynamics of the basin and will be discussed in Section 6.1. Another interesting observation that was revealed in the timeseries was the clipping of the long WG about 37 seconds due to its thicker bracket in the shallow water depth. The clipping was confirmed by the fact that the medium WG recorded a lower water surface elevation as compared to the long WG. Due to the clipping, it was decided that the medium WGs were more accurate and better suit for describing the free surface over the shelf. Despite this isolated incident, the timeseries from both WGs confirm the symmetry of the wave as it evolved over the shelf.
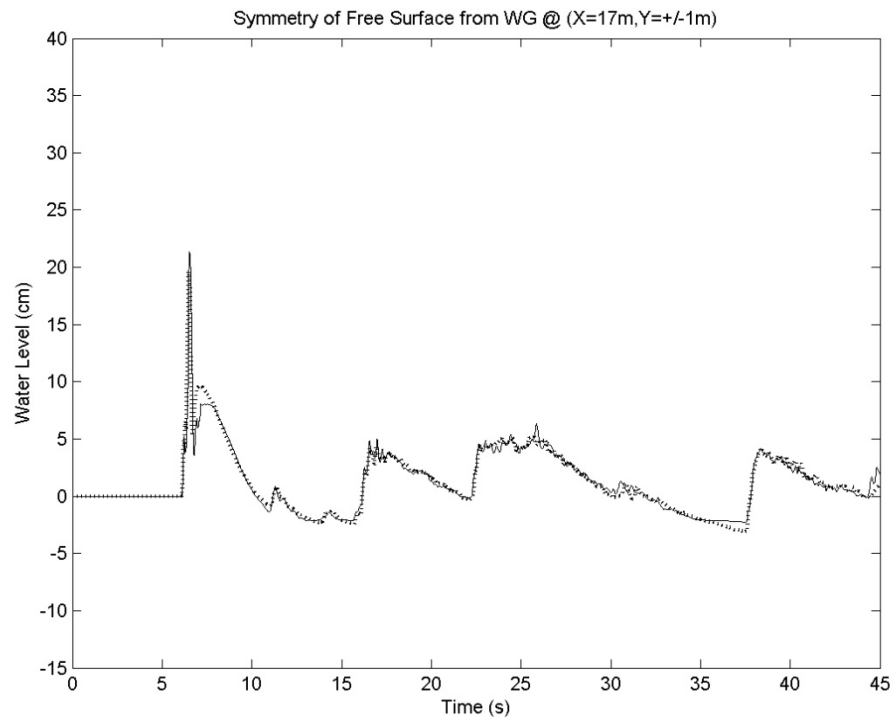
Figure 6: Symmetry of long WG (line) and medium WG (dots) located at X=17.0, Y=+/-1m.

Moving further onshore to X=19m and away from the centerline, Figure 7 shows the symmetry of the timeseries as the wave continued to evolve while traveling over the shelf. The splash up at about 8 seconds from the jet's impact on the water surface is reduced as the bore came to more closely resemble a hydraulic jump in a channel. Again, the large wave motions due to the passing of other borefronts that were observed during the experiment, along with the clipping of the long WG between 35 and 39 seconds as explained in Figure 6, were seen. The medium and long WGs timeseries at these locations further confirm the symmetry of the wave due to the basin's bathymetry.
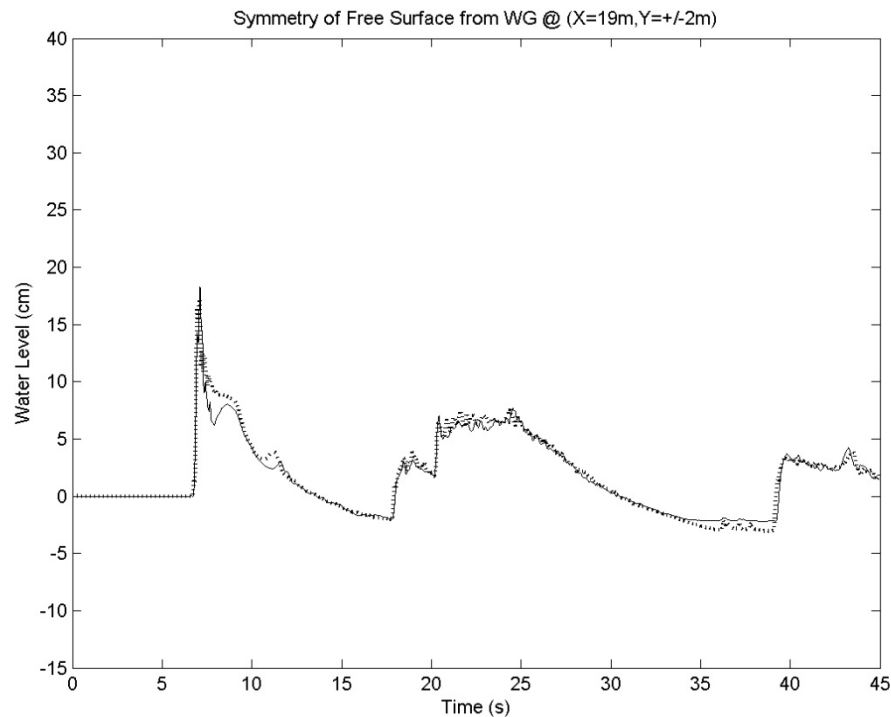
Figure 7: Symmetry of long WG (line) and medium WG (dots) located at X=19.0, Y=+/-2m.

The comparison of the free surface timeseries, obtained by the WGs on respective sides of the centerline and near the wavemaker, confirmed the symmetry and repeatability of the generated wave, respectively. The proven symmetry validates the argument that the instruments (WGs, usWGs, and ADVs) could be mirrored about the centerline of the basin in order to provide a more complete presentation of the free surface, turbulence, and kinematic properties that developed in the basin during the experiment. The proven repeatability validates that measurements taken during multiple trials and at different locations could be used together to provide a more complete portrayal of the dynamics observed. For the rest of the paper, the bottom half of the basin (Y≤0m) will be the focus of the presented material with the following: the long

WGs describing the free surface offshore of the shelf edge, the medium WGs describing the free surface onshore of the shelf edge but offshore of the SWS, the usWG describing the runup shoreward of the SWS, the bridge mounted ADVs describing the flow offshore of the shelf edge, and the bottom mounted ADVs describing the flow onshore of the shelf edge.

# 5.0 ADV MEASUREMENTS

## 5.1 Filtering

The ADVs used to record the fluid velocities generated in the basin during the experiment experience noise.  As a result, unreliable data which appeared as large erroneous spikes had to be eliminated using multiple filters.  The filters used included the signal-to-noise ratio (SNR) and the correlation (COR) timeseries provided by the ADVs during the experiment and a curvature technique established while analyzing the data after the laboratory experiment was completed.  The filters were applied to the timeseries obtained for all three components of velocity at each ADV location.

The first two filters which used the SNR and COR provided a means for eliminating data based on the quality of the signal received by the ADV during the actual measurements.  The SNR was a real-time measurement revealing the strength of the scattered acoustic signal received by the ADV (Cea, Puertas, & Pena 2007).  The filtering criteria used for the SNR required the signal to be greater than 10 decibels which was the minimum threshold suggested by the ADV manufacturer.  The COR was also a real-time measurement, but it accounted for the change in the instantaneous velocity relative to the sampling frequency (Cea, Puertas, & Pena 2007).  The sampling frequency of the ADVs during the experiment was 50 Hz and our filtering criteria required the COR to be greater than 70% as suggested by the manufacturer.

The third filter used a curvature technique ($\partial^2 U / \partial t^2$) to compare each data point ($U_t$) at a given time step with data point before ($U_{t-\Delta t}$) and after ($U_{t+\Delta t}$). The curvature was defined as the time rate of change of the acceleration of the fluid and was dependent on the sampling frequency ($\Delta t$). Center differencing was used to discretize and quantify the curvature at each time step in the timeseries as shown in Equation 1.

$$(1) \quad \frac{\partial^2 U}{\partial t^2} = \left| \frac{1}{\Delta t^2} (U_{t+\Delta t} - 2 * U_t + U_{t-\Delta t}) \right|$$

To filter the data without bias, multiple thresholds of the maximum curvature were analyzed in order to eliminate noise in the data without discarding quality data. The curvature was set to a maximum limit assuming that the time rate of change of the acceleration of the fluid physically possible was much lower to ensure that good quality data was not eliminated. With that assumption, the thresholds determined for the ADVs positioned offshore of the shelf edge were different from the ADVs positioned onshore of the shelf edge due to the larger fluid accelerations and the turbulence associated with hydrodynamics on the shelf. It was determined that a curvature <175 m/s$^3$ for the ADVs offshore of the shelf edge and <300 m/s$^3$ for the ADVs onshore of the shelf edge maximized the noise eliminated without discarding good quality data.

The final filter required that a minimum of 10 trials pass the previous filters at each time step in order to quantify turbulence with 20% accuracy. The method of determining the turbulence is described in the following section, while the statistical

approach used to determine the minimum number of trials required is discussed in more detail in Section 5.3.

## 5.2 Turbulence Calculations

After filtering the timeseries, we were able to begin calculating and quantifying specific turbulent characteristics of the flows measured by the ADVs. Turbulence is defined turbulence as the deviations of the instantaneous velocity from the mean flow (Tennekes & Lumley, 1972; Mathieu & Scott, 2000). Turbulence was determined by comparing an instantaneous velocity timeseries with an established mean flow timeseries for a given ADV location. By subtracting the instantaneous velocity from the mean flow, the instantaneous turbulent fluctuations were determined.

In order to obtain and quantify the turbulence associated with the breaking solitary wave, multiple trials had to be run for each ADV location recording the instantaneous velocity ($U$, $V$ and $W$) timeseries. After recording at least 20 trials and filtering them, the instantaneous velocity timeseries were ensemble averaged to establish the mean flow ($\overline{U}$, $\overline{V}$ and $\overline{W}$) at the instrument location as described by Equation (2) where $n$ was the number of trials performed. The following equations are expressed in terms of the U component, but are used to determine all three directional components.

$$(2) \quad \overline{U}(t) = \frac{\sum_{i=1}^{n} U(t)_i}{n} \quad [L/T]$$

Once the mean flow was determined, the instantaneous turbulent fluctuations

($u'$, $v'$ and $w'$) for each trial were calculated by subtracting the mean flow from the

instantaneous timeseries, Equation (3).

$$(3) \quad u'(t) = U(t) - \overline{U}(t) \quad [L/T]$$

At this point, the Reynolds stresses, which are the basic method for quantifying

turbulence, could be quantified using similar techniques as previously done by Ting

(2005). The average Reynolds stresses ($\overline{u'u'}$, $\overline{v'v'}$, $\overline{w'w'}$, $\overline{u'v'}$, $\overline{u'w'}$ and $\overline{v'w'}$) were

calculated by multiplying the various combinations of the instantaneous turbulent

fluctuation components together for each trail ($n$) and then ensemble averaged to obtain

a timeseries of the Reynolds stresses as described by Equation (4).

$$(4) \quad \overline{u'u'} = \frac{\sum_{i=1}^{n} u'(t)_i u'(t)_i}{n} \quad [L^2/T^2]$$

After calculating the Reynolds stresses, it was desired to express the turbulence

in the same units as the velocity and the RMS (root-mean-square) turbulence ($u'_{rms}$, $v'_{rms}$

and $w'_{rms}$) was determined with Equation (5).

$$(5) \quad u'_{rms} = \sqrt{\overline{u'u'}} \quad [L/T]$$

Using the Reynolds stresses obtained with Equation (4), the total turbulent

kinetic energy ( $K$ ) was quantified.  The total turbulent energy was of particular

importance because it provided a single timeseries which related all three components of

the turbulence.  The turbulent energy was calculated by adding the three Reynolds

stresses, $\overline{u'u'}, \overline{v'v'}$, and $\overline{w'w'}$, and dividing by 2 as described in Equation (6).

$$(6) \quad K(t) = \frac{\overline{u'u'} + \overline{v'v'} + \overline{w'w'}}{2} \quad [L^2/T^2]$$

## 5.3 Turbulence Error

The turbulent quantities determined above were statistically dependent on the

number of trials at each time step that passed the filters.  During the experiment, at least

20 trials were conducted at each ADV location, but due to filtering of the raw data, the

actual number of data points available to quantify turbulence was reduced.  The

reduction in the number of data points required that a minimum number of trials be

established to accurately quantifying turbulence.  By setting a minimum number of trials

required at each time step, a final filtering criterion was developed.

The turbulent quantities were determined by ensemble averaging the multiple

trials, so as the number of data points available at each time step was reduced, the

average inherently had greater variability.  The change in the ensemble averages caused

errors to be introduced into the quantified turbulence and revealed the need to determine

the accuracy associated with a set minimum number of data points. In order to quantify the error associated with the predicted turbulence quantities, a turbulence convergence approach was used. To do this, the U component of the RMS turbulence ($u'_{rms}$) was calculated using all available filtered data at a particular ADV location (X=17m, Y=0m) where 40 trials were performed and the amount of data eliminated by the other filters was relatively low. Because of the large statistical population, trials were randomly eliminated one at a time, a new RMS turbulence timeseries was calculated, and it was compared to the original RMS turbulence timeseries containing all the available trials. After a trial was eliminated, the original RMS timeseries was subtracted from the new RMS timeseries and then divided by the original RMS timeseries to determine the Error that was introduced at each time step as defined in Equation (7).

$$(7) \quad Error(t) = \frac{u'(t)_{rms(new)} - u'(t)_{rms(original)}}{u'(t)_{rms(original)}}$$

After each trial was eliminated, an AverageError for the timeseries was quantified by averaging the error at each time step ($n$) over the timeseries as shown in Equation (8).

$$(8) \quad AverageError = \frac{\sum_{i=1}^{n} Error(t_i)}{n}$$

This process was repeated until there was only one trial remaining and then average errors were plotted against the number of trials remaining. To confirm that the errors associated with progressively removing more trials converged, the process of randomly eliminating trials was performed a total of 4000 times and shown in Figure 8. From analyzing the figure, it was concluded that by requiring a minimum of 10 data points at each time step the turbulence was quantified with 20% accuracy. Based on this criterion, if an individual time step did not contain at least 10 data points after being filtered, all data points for this time step were eliminated so that no turbulence was quantified. By using the additional filtering criteria established by the turbulence convergence method, we can confidently suggest that our results present the measured turbulent quantities within 20% of the actual quantities.
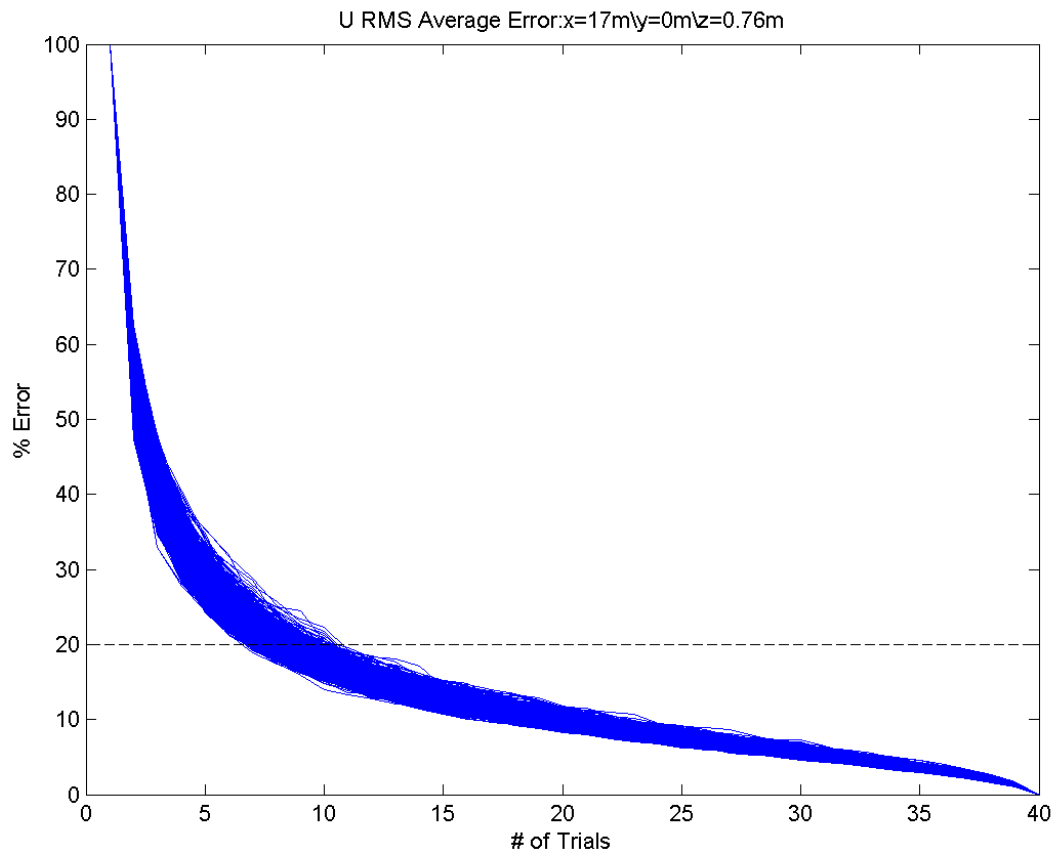
Figure 8: Turbulence convergence used to predict accuracy of turbulence quantified with ADV measurements.

# 6.0 OBSERVED WAVE EVOLUTION

To understand the three dimensionality of the free surface, fluid velocities, and turbulent energy of interest; a complete understanding of the hydrodynamics visually observed during the laboratory experiment was required. The single solitary wave generated for each trial of the experiment created very repeatable, but yet complex hydrodynamics throughout the basin. In particular, multiple borefronts and reflected waves developed on top of the shelf due to the flows' interaction with the bathymetry. The borefronts referenced resembled hydraulic jumps that extended across the shallow water shelf, but propagated and responded similar to waves as they interacted with the bottom.

## 6.1 Visually Observed Hydrodynamics

To depict the features that developed in the basin due to the generated wave, multiple planview images of half the basin (Y≤0m) at sequential times during the experiment are displayed in Figure 9. The images provide a detailed explanation of the basin which will be vital to understanding the data presented throughout the paper. The wave generated by the wavemaker propagated from left to right in the images in the cross-shore direction as it encountered the shelf, broke, and traveled up the planar beach. The centerline of the basin (Y=0m) was perpendicular to the black vertical lines, and it passed through the apex of the shelf near the top of the images. The side wall of the basin was along the bottom and the wavemaker was to the left of the images both just

outside the field-of-view.  The vertical black line on the left side of the images indicates

the end of the constant depth portion of the tank and the beginning of the shelf.  The

diagonal black line indicates the edge of the flat portion of the shallow water shelf.  The

vertical black line on the right side is shoreward of the SWS and indicates the planar

beach which extends beyond the field-of-view.  The green areas that can be seen near the

bottom of most of the images were from a dye study in which dye was released along the

edge of the shelf to reveal the advection and dispersion of the flow during the

experiment.

The images are organized in time with time starting at when the solitary wave

was generated by the wavemaker.  Figure 9a shows the generated wave arriving on the

shelf and beginning to break at 6.2 seconds.  Breaking began onshore of the shelf apex

along the centerline.  The initial impact of the jet with the water surface, characteristic of

a plunging breaker, can be seen as a dense localized white area.  This was the beginning

of the borefront associated with the generated wave and is labeled as borefront (1).  The

foggier area around the impacting jet is the beginning of the tube of air that became

trapped between the jet and vertical wave front.  The white arrows denote the onshore

flow associated with borefront (1) was onshore.

At 8.3 seconds, Figure 9b shows that the breaking of borefront (1) had extended

to the basin side wall as it traveled further onshore.  The flow behind borefront (1) was

onshore in the direction of wave propagation (white arrows); while on top of the shelf

near the apex, the flow was directed offshore (black arrows) due to the trough created

behind the solitary wave as pointed out in Section 4.1.  The flow just offshore of the

apex was directed onshore (white arrows) as a secondary wave, labeled as borefront (2), propagates onshore following the trough.  It was also interesting because at this time the apex of the shelf became dry for a short period preceding borefront (2) due to the trough.

7.8 seconds later at 16.1 seconds, Figure 9c shows the shoreward propagation of borefront (2), parabolic in shape due to refraction, over the shallow water shelf and resulting flow (white arrows).  Borefront (3), visible further onshore, was the reflected portion of borefront (1) off the top of the planar beach and it was observed to propagate toward the apex of the shelf creating an offshore flow (black arrows).  Borefront (3) was also parabolic in shape revealing the basic shape of borefront (1) as it reflected off the top of the planar beach.  By this point in time, the dye had been injected near the bottom of the image and advected shoreward due to the onshore flow following borefront (1).

Figure 9d shows the same two borefronts as Figure 9c, but 4 seconds later after they have passed through each other.  Borefront (2) was to the right in the image propagating onshore (white arrows) and borefront (3) was to the left propagating offshore (black arrows).  The green dye can be seen as it gathered along the shelf edge near the basin side wall due to the offshore flow resulting on the shelf following borefront (3).

At 26.4 seconds, Figure 9e shows that borefront (2) had traveled to the right beyond the field-of-view, while borefront (3) was converging at the apex of the shelf.  At this point, the flow on the shelf was still strongly direction offshore (black arrows) which was confirmed by the green dye being advected offshore of the shelf edge.  Near the apex, borefront (3) rapidly converged which caused a small wake to develop following

the intersection of the shelf edge and the borefront toward the centerline of the basin. At the apex, the wake collided with the similar wake from the other half of the basin in the area of the white oval. The wakes are of particular importance because they broke as they interacted with each other and could be identified as a large turbulent event in the data. Along the shelf edge where there was an abrupt change in the bathymetry coupled with the offshore flow, a shear layer began to develop which was revealed by the formation of a hydraulic bore. The shear layer will be discussed in more detail in Section 9.0.

Figure 9f shows that at 31.9 seconds no borefronts were visible on the shelf although the strong offshore flow (black arrows) following borefront (3) as it propagated offshore still persisted maintaining the hydraulic bore along the shelf edge. The instabilities in the shear layer eventually resulted in a counter clockwise rotating structure that developed offshore of the shelf edge. Its rotation could be seen by the concentration of green dye inside the white circle and will be discussed in further detail in Section 9.0. After colliding near the apex at some time between 26.4 seconds and 31.9 seconds, the wakes associated with borefront (3) could be seen traveling radially outward over the shelf.

The eddy (white circle) that was identified in the previous image was still visible 5 seconds later at 36.9 seconds in Figure 9g. By this time a return wave, labeled borefront (4), had arrived in the shelf traveling onshore. Borefront (4) was determined to be a combination of a trapped wave due to the very shallow water and a reflected wave from the wavemaker. The offshore flow still persisted on the shelf, but behind

borefront (4) the flow had turned onshore (white arrows).  Borefront (4) was parabolic in shape similar to borefront (2).

By 41.9 seconds borefront (4) had propagated further shoreward causing the flow over the shelf to be directed onshore (white arrows) as shown in Figure 9h.  Again, the eddy (white oval) could be seen by the gathering of dye even after the mean flow had changed in directions, but was less defined.  By understanding basic hydrodynamics that developed, data collected could be analyzed despite complexities due to spatial and time varying nature of flows.  With that said, the free surface measurements allowed the evolution of the solitary wave to be investigated, but the investigation of the fluid velocity was limited to after the generated wave past each individual instrument until 45 seconds.  These constraints were due to the high concentration of air that was entrained during breaking resulting in a lack of good quality data at these times and waves reflecting off the wavemaker and back wall of the basin.  Borefront (4) was partially due to a reflected wave off the wavemaker, but since it was also a result of a trapped wave on the shelf it was included in the analysis to completely investigate the hydrodynamics of the basin.  Fortunately the data after the solitary wave was complete and provided the information needed to analyze the dynamics of the flow.
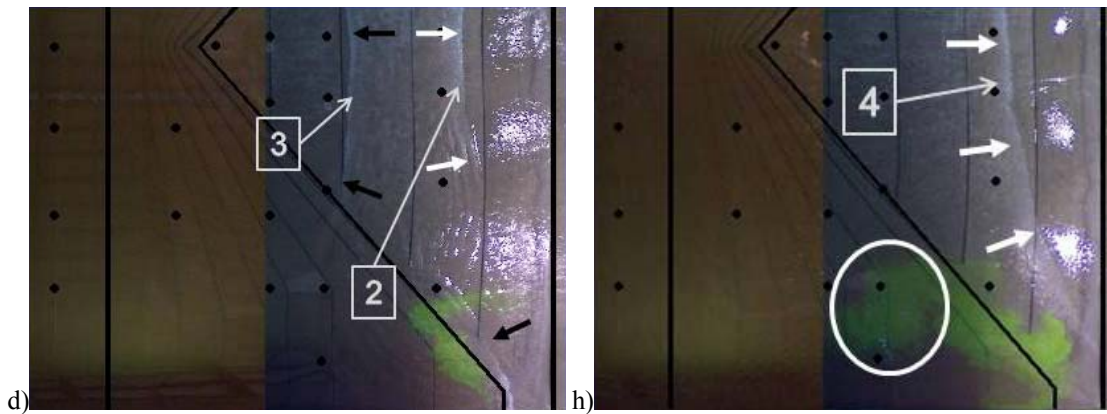
Figure 9: Images of the basin at a) 6.2s, b) 8.3s, c) 16.1s, d) 22.1s, e) 26.4s, f) 31.9s, g) 36.9s, and h) 41.9s after the solitary wave was generated. (●) ADV locations, (→) mean flow direction with, generally, white arrows indicating onshore flows and black arrows indicating offshore flows.

## 6.2 Free Surface Displacement

After studying the typical hydrodynamics during the experiment, the data collected by the WGs could be analyzed with a greater degree of confidence. First the maximum free surface elevations throughout the basin were compiled, and then specific WG locations were more closely analyzed to further grasp the hydrodynamics. As explained above, the medium WGs were used onshore of the shelf edge while the long WGs were used offshore of the shelf and mirrored when necessary to provide a complete picture of the free surface elevations.

The maximum free surface elevations obtained were associated with the solitary wave as it propagated through the basin and are shown in Figure 10. The straight black line near X=10.2m marks the end of the constant depth portion of the basin, while the diagonal, black line represents the edge of the triangular, shallow water shelf similar to Figure 9. The evolution of the wave portrayed by the data confirmed visual observations

that the wave height was very constant offshore of the shelf apex and, as portrayed in Figure 9, breaking began at the apex spreading laterally along the shelf edge to the basin side wall as the wave traveled onshore. The breaking was evident in Figure 10 by the rapid decay in wave height at the shelf edge.

A particular area of interest was the white region offshore of the shelf edge near the basin side wall. In this region, the wave increased significantly to its maximum height due to the combination of shoaling and the focusing of the wave energy at the side wall. In general, shoaling is referred to as the growth in wave height due to decreasing water depth over a sloping bathymetry. The focusing of wave energy was caused by the wall which reduced the dispersion of energy away from the centerline as the wave interacted with and broke on the shelf. Although there were some boundary effects at work, the location of maximum wave height agreed with conclusions made by Grilli et al. (1994) that shoaling is greater on milder slopes and less noticeable on steeper slopes. This also explained the lack of shoaling at the apex of the shelf were the slope is necessary for a strongly plunging breaker (Grilli et al., 1994).
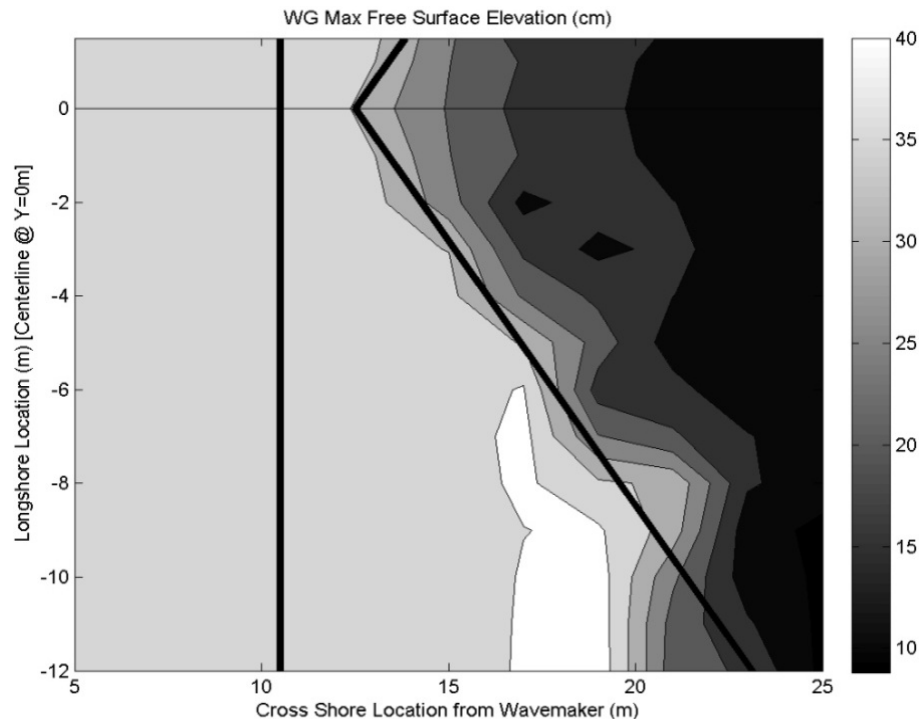
Figure 10: WG maximum free surface elevation (cm). Black lines, from left to right, denote the end of constant depth portion of the tank and the shelf edge.

By understanding the evolution of the generated solitary wave and its decay in wave height as it propagated over the shelf, the additional borefronts, as described in Figure 9, could be more readily analyzed. To do this, the free surface elevations recorded by multiple WGs along four cross-shore transects were provide in Figure 11- Figure 15. The locations of the transects (white lines) were positioned in the longshore direction at Y=0m, -1m, -2m, and -5m, shown in Figure 11, with each transect including WGs in at cross-shore locations including X=7.5m, 11.5m, 13.0m, 15.0m, 17.0m, and 21.0m. The multiple transects allowed the time and spatial lag of the individual borefronts in relation to the other WGs in a given transect to be revealed. The four borefronts that were identified in Figure 9 were labeled similarly and depicted in Figure

12-Figure 15 by four gray lines with (1) representing the generated solitary wave, (2) representing the secondary borefront, (3) representing the reflected borefront, and (4) representing the return wave borefront. The direction of propagation of the borefronts can easily be determined by looking at the slope of the gray lines; a negative slope denotes borefronts that were traveling onshore while a positive slope denotes the borefront that was traveling offshore.
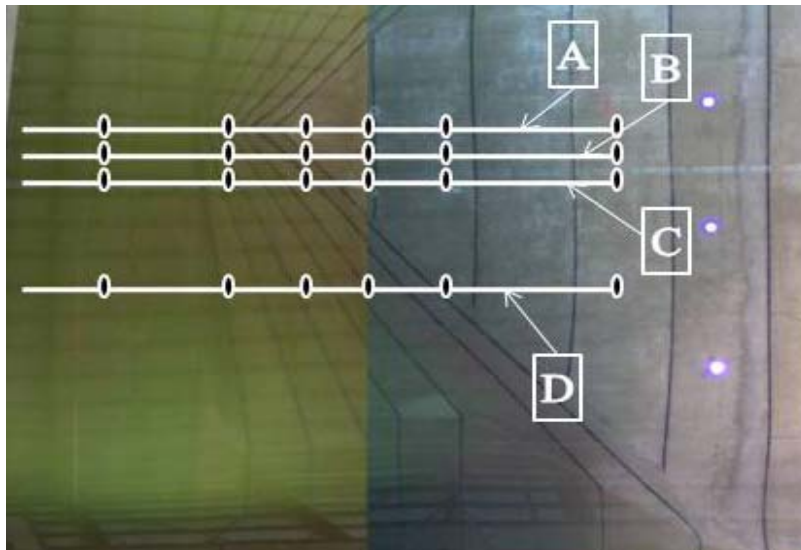


Figure 11: White lines denote cross shore transects located in the longshore direction at A) Y=0m, B) Y=-1m, C) Y=-2m, and D) Y=-5m.

Starting at the centerline of the basin, Transect A shown in Figure 12 contains two WGs located at X=7.5m and 11.5m offshore of the shelf edge. These two location confirm that the (1) experienced very little shoaling as it encountered the steep slope of the shelf agreeing with Grilli et al. (1994). Also at these offshore locations, the wave was symmetrical from front to back which is typical of a wave prior to breaking (Hsiao

et al. 2008).  Moving onshore, at 13.0m, the front face of (1) had started to became

vertical just prior to breaking which was forced by the abrupt slope at the apex and was

expected with the plunging breaker (Grilli et al., 1994).  By the time (1) reached

X=15.0m, breaking had begun as revealed by the decay in wave height although the jet,

associated with a plunging breaker, impacted the water slightly shoreward as shown in

Figure 9a. Shoreward at X=17.0m and 21.0m, the height of (1) had decreased

significantly as it traveled further onshore.  (2) followed after the trough created by (1)

and could be tracked in the data as it traveled onshore and passed through (3) at some

point between X=17.0m and X=21.0m as shown by the crossing of the gray lines.  The

height of (3) grew suddenly at X=13.0m as it traveled offshore and converged on the

apex of the shelf due to the trailing wakes colliding, which were described in relation to

Figure 9e.  The localized event ($\rightarrow$) at X=15.0m captured the wakes coming together and

breaking as (3) converged on the apex of the shelf.  The times of (3) at X=13.0m and the

wakes at X=15.0m were very well correlated in the timeseries with visual observations

during the experiment.  (4) was visually only seen on the shelf after the offshore flow

associated with (3) subsided, but, interestingly, its development offshore was detected at

X=7.5m and 11.5m.  Further offshore, (3) and (4) probably passed through each other

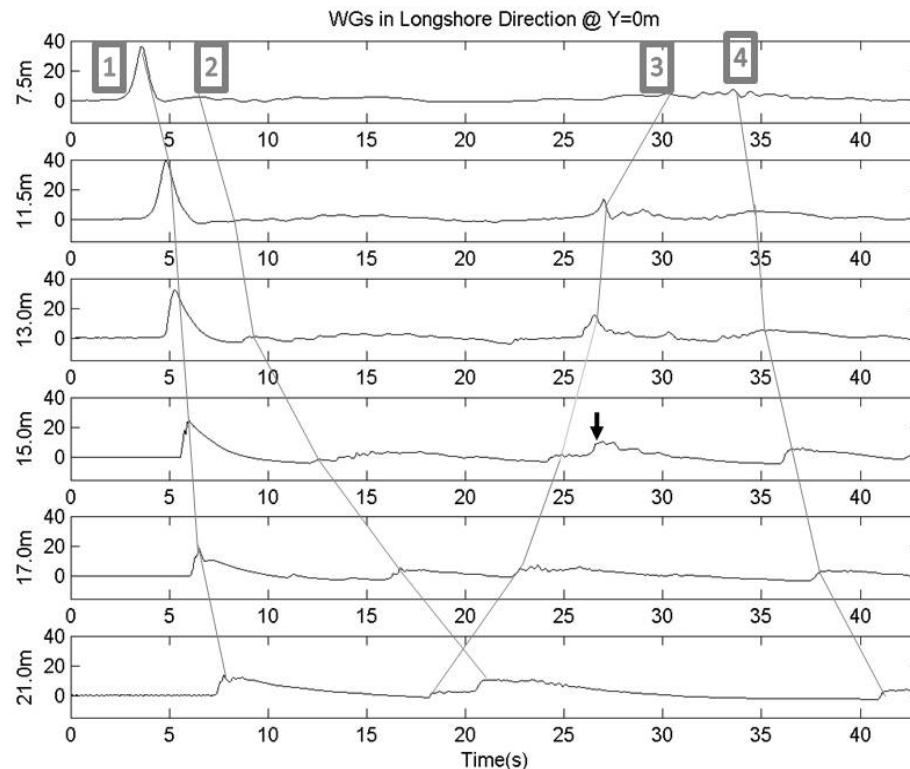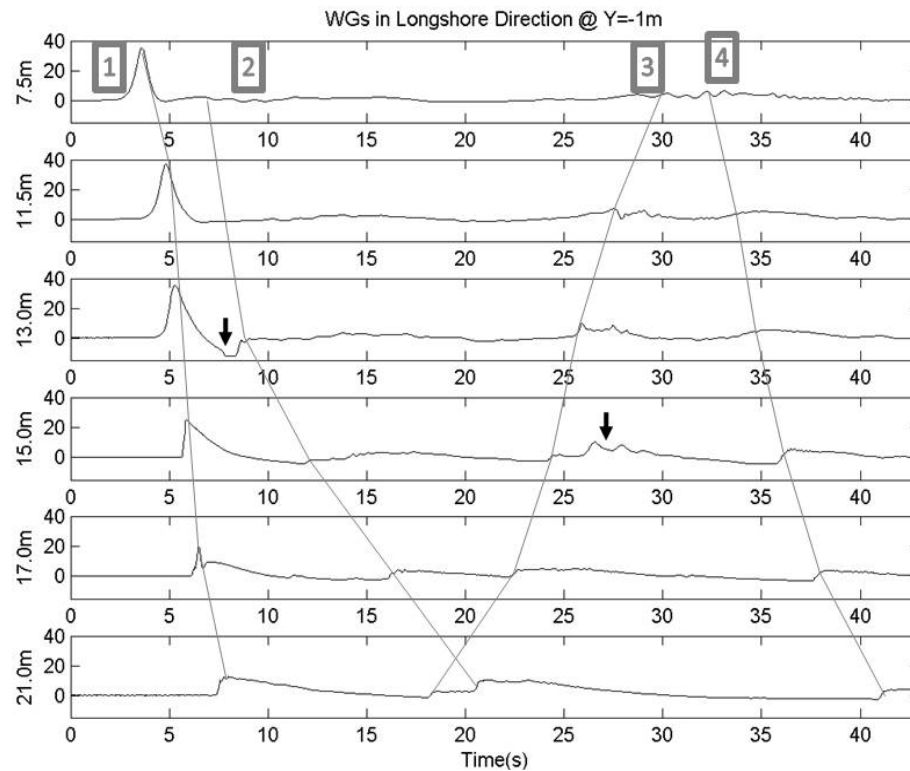similar to (2) and (3) as suggested by the slopes of the gray lines.

Figure 12:  WG free surface elevation (cm) timeseries of cross shore transect (X=7.5m, 11.5m, 13.0m, 15.0m, 17.0m, and 21.0m) at specified longshore location (Y=0m). Gray lines show identified borefronts, (1) generated wave, (2) secondary borefront, (3) reflected borefront, and (4) return wave/borefront, and times they pass each WG.  (→) Denotes localized event.

Moving away from the centerline to Transect B located at Y=-1m, Figure 13 shows very similar characteristics revealed by Transect A.  Again, the gray lines track the same respective borefronts/waves as defined in Figure 12.  In Transect B, X=7.5m, 11.5m, and 13.0m are located offshore of the shelf edge as revealed by the symmetry of (1) from front to back which is typical of waves prior to breaking (Hsiao et al. 2008). The front face of (1) had become vertical at X=15.0m as it traveled onto the shelf forcing it to break by the time it arrived at X=17.0m.  The splash up of the water surface due to the impacting jet, characteristic of a plunging breaker, could be seen from (1) at

X=17.0m around 7 seconds. The splash up was detected as spike in the water surface relative to the associated borefront. Another interesting featured revealed by Transect B at X=13m was the localized event (→) due to the large draw down of the free surface as the trough passed following (1), as observed in Figure 9b, could be seen at X=13.0m around 8 seconds. As discussed in Figure 12, (2) arrived on the shelf directly after the localized drawn down from the trough of (1). It quickly traveled onshore as shown by the decreased negative slope of the gray line between X=15m and X=21m in Figure 13. (3) was propagating offshore due to its origin and passed through (2) at some point between X=17m and X=21m as shown by the crossing of the gray lines. At X=15m, a second localized event (→) captured by the WG data was the colliding wakes trailing (3) as it converged on the apex of the shelf. This event was the same localized event discussed in Figure 12 except the two wakes could be seen after they passed through each other since the point of their intersection was along the centerline. (4) was detected by the WGs after (3) had propagated offshore of the shelf as confirmed by the timeseries at X=7.5m. Further offshore, (3) and (4) probably passed through each other and caused the gray lines to cross similar to (2) and (3).
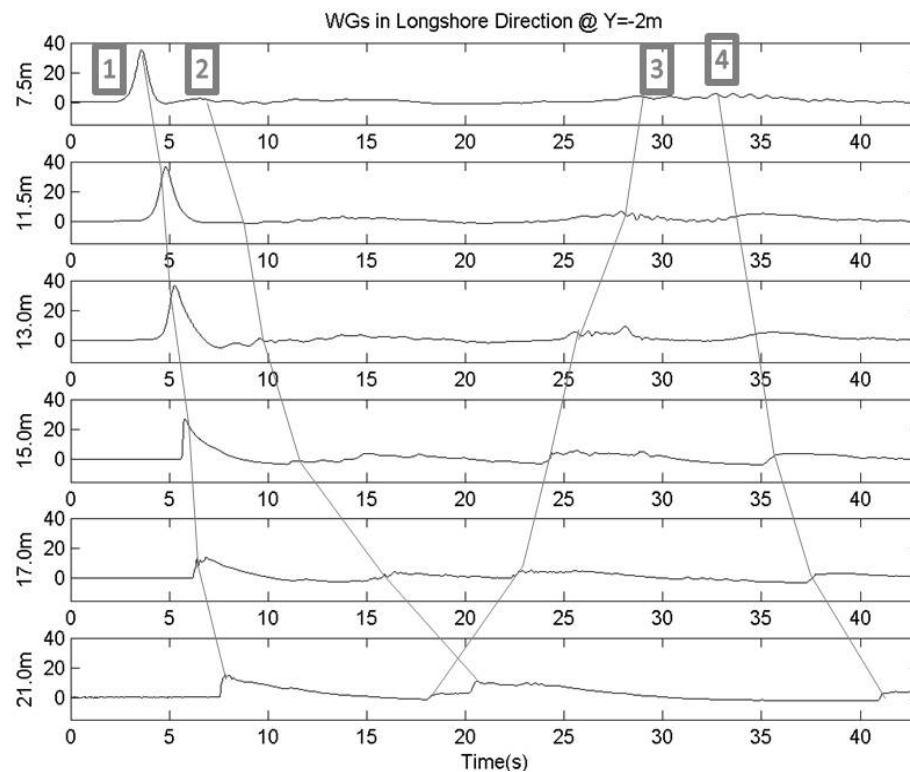
Figure 13: WG free surface elevation (cm) timeseries of cross shore transect (X=7.5m, 11.5m, 13.0m, 15.0m, 17.0m, and 21.0m) at specified longshore location (Y=-1m). Gray lines show identified borefronts, (1) generated wave, (2) secondary borefront, (3) reflected borefront, and (4) return wave/borefront, and times they pass each WG. (→) Denotes localized events.

Continuing to move away from the centerline, Figure 14 shows Transect C located in the longshore direction at Y=-2m. Again, the gray lines track the same respective borefronts/waves as Figure 12 and Figure 13. At Transect C, the shape of (1) was nearly symmetrical from front to back at X=7.5m, 11.5m, and 13.0m which is typical of waves before they begin to break (Hsiao et al. 2008) agreeing with the fact that they were located offshore of the shelf edge. The front face of the generated wave became vertical at X=15m as (1) traveled onto the shelf which forced breaking by the time it arrived at X=17m. (2) was the second borefront that became noticeable on the

shelf after (1) passed.  The localized event observed in Transect B was not observed in

transect C, but once (2) arrived on the shelf it quickly traveled onshore as shown by the

decreased negative slope of the gray line between X=15m and X=21m in Figure 14.

Again, (3) was propagating offshore due to its origin and passed through (2) at some

point between X=17m and X=21m as shown by the crossing of the gray lines.  (4) was

detected  by the WGs after (3) had propagated offshore of the shelf as confirmed by the

timeseries at X=7.5m. Further offshore, (3) and (4) probably passed through each other
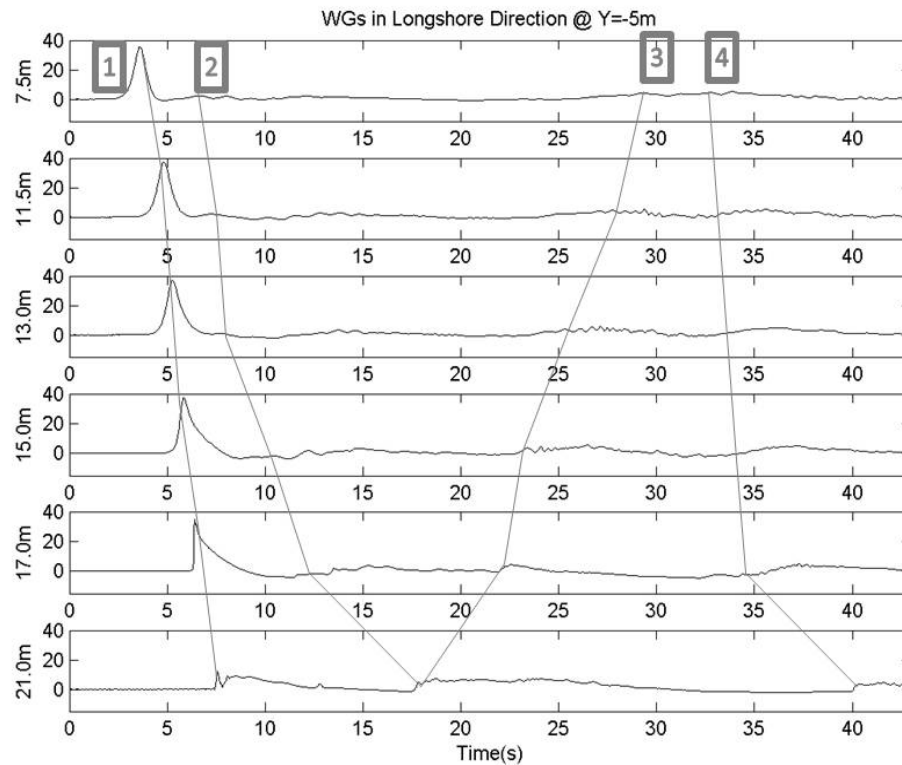
and caused the gray lines to cross similar to (2) and (3).



Figure 14:  WG free surface elevation (cm) timeseries of cross shore transect (X=7.5m, 11.5m, 13.0m, 15.0m, 17.0m, and 21.0m) at specified longshore location (Y=-2m). Gray lines show identified borefronts, (1) generated wave, (2) secondary borefront, (3) reflected borefront, and (4) return wave/borefront, and times they pass each WG.

Furthest from the centerline, Figure 15 shows Transect D located in the longshore direction at Y=-5m. The gray lines track the same respective borefronts/waves as Figure 12, Figure 13, and Figure 14. At Transect D, the shape of (1) was nearly symmetrical from front to back at X=7.5m, 11.5m, 13.m, and 15.0m confirming that these locations were located offshore of the shelf edge. The front face of (1) became vertical at X=17.0m and breaking had begun as the wave traveled over the shelf and arrived at X=21.0m.

Again, once (2) arrived on the shelf it quickly traveled onshore as shown by the decreased negative slope of the gray line between X=17m and X=21m in Figure 15. In Transect D, (3) was propagating offshore due to its origin and passed through (2) at X=21m as shown by the intersection of the gray lines. (4) was detected by the WGs after (3) had propagated offshore of the shelf as confirmed by the timeseries at X=7.5m. Further offshore, (3) and (4) probably passed through each other and caused the gray lines to cross similar to (2) and (3) in Transects A, B, and C.

A complete set of the free surface elevations recorded by the WG is presented in Appendix I.

Figure 15:  WG free surface elevation (cm) timeseries of cross shore transect (X=7.5m, 11.5m, 13.0m, 15.0m, 17.0m, and 21.0m) at specified longshore location (Y=-5m). Gray lines show identified borefronts, (1) generated wave, (2) secondary borefront, (3) reflected borefront, and (4) return wave/borefront, and times they pass each WG.

## 6.3 Turbulence Characteristics on Shelf

The visually observed hydrodynamic and free surface displacements provide an understanding of the features that develop during the experiment with respect to the free surface, but in order to understand the dynamics below the water surface, the fluid velocity was investigated.  To do this, all three components of the mean fluid velocity measured by the ADVs throughout the basin were used to extract and quantify turbulence which is believed to be the major mechanism that causes sediment to become and remain suspended within the water column.  Once suspended, the mean flow is

responsible for advecting (transporting) sediment (Ting & Kirby, 1994) and ultimately governing coastal morphology.

In particular, the turbulence can be quantified relative to each component of velocity by the RMS turbulence ($u'_{rms}$, $v'_{rms}$ and $w'_{rms}$) and it can be expressed as the square root of the total turbulent kinetic energy ($\sqrt{K}$). The following figures are shown to reveal the complete flow and turbulent characteristics, in cm/s, that developed on the shallow water shelf during the experiment due to the generated solitary wave and resulting hydrodynamics. The turbulence from each ADV locations shown coincide with a WG measurement location contained in the cross-shore transects discussed above in Figure 11 through Figure 15, but due to the limited ADV locations not all WG locations were co-located with ADVs. The ADV locations displayed were organized in relation to each Transects A, C, and D starting at the centerline moving toward the basin side wall and over the shallow water shelf from the most offshore location to the most shoreward location. Nine of the ADV locations that were positioned on top of the shelf and co-located with WGs can be seen in Figure 2 between X=13m and X=21m and between Y=0m and Y=-5m. In the figures, the turbulence data was not obtained at intermittent times due to a large quantity of the data having been eliminated based on the filtering criteria described in Sections 5.1 and 5.3.

At each location, the passing of the four borefronts defined in the Section 6.1 were identified as turbulent events revealed in the $\sqrt{K}$ timeseries. Starting closest to the centerline along Transect A at the most offshore ADV location, X=13m, Y=0m, Figure 16 shows the turbulent events associated with the passing borefronts in the $\sqrt{K}$

timeseries.  By looking at the respective WG timeseries, the passing of borefronts (1)

through (4) occurred at times around 5, 9, 26, and 35 seconds, respectively, and were

well correlated to events (spikes) in the $\sqrt{K}$ timeseries.

Two other turbulent events, at about 22.5 and 30 seconds, were revealed by total

turbulent energy due to the complex flows that converged at the apex of the shelf.  At

22.5 seconds, just before borefront (3) arrived there was another small borefront that

developed, which eventually contributed to the localized wakes that collided near

X=15m, Y=0m as observed in Figure 9e and discussed in Figure 12.  At 30 seconds,

during the offshore flow following borefront (3), another small borefront developed

similar to a trapped wave for about 2 seconds before being diminished by the strong

flow.  Looking at the total turbulent kinetic energy timeseries, in general the turbulent

events were very well correlated with accelerations in the fluid (changes in the fluid

velocity with time).  Even if specific hydrodynamic features were not noticeable specific

turbulent events, the fluid velocity was observed to increase or decrease and/or change

directions with time creating vertical shear.
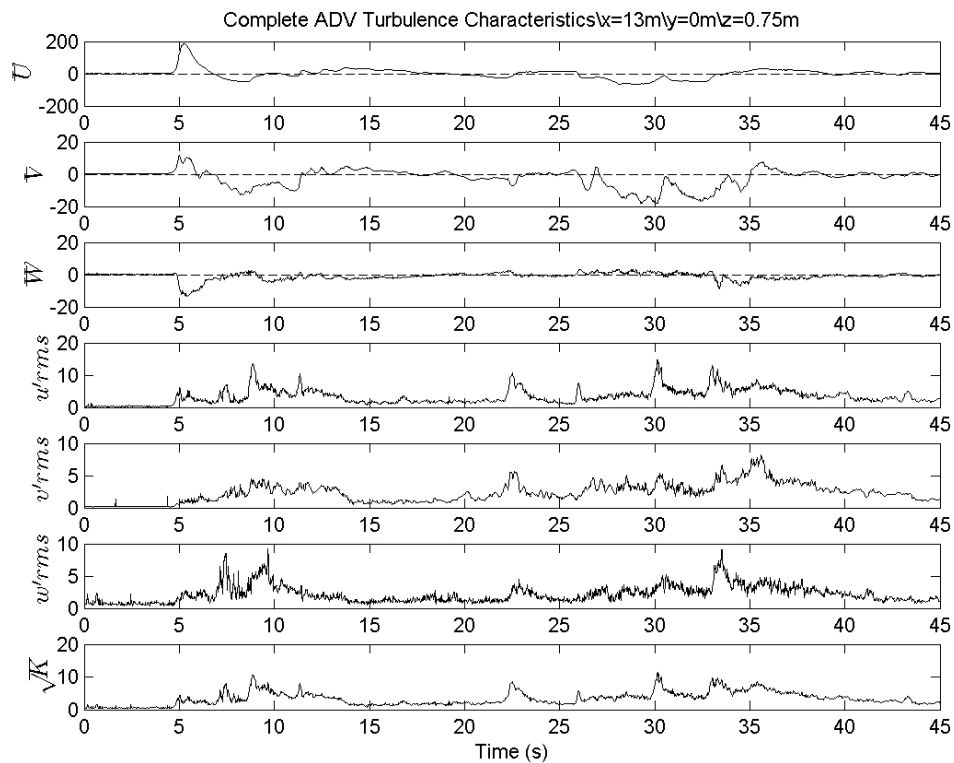
Figure 16: Mean velocity (cm/s), RMS turbulence (cm/s), and $\sqrt{K}$ (cm/s) of ADV co-located with WG at X=13.0m, Y=0m, Z=0.75m.

Along Transect A, but further onshore at X=15m, Y=0m, Figure 17 shows that the turbulent events in the $\sqrt{K}$ timeseries associated with borefronts (1) through (4) were correlated at times around 6, 13, 24.5, and 36 seconds, respectively. The large turbulent event at 27.5 seconds was attributed to the colliding and breaking of the wakes that followed borefront (3) along the shelf edge as discussed in Figure 9e and Figure 12. Again, turbulent events that were revealed and were not correlated with specific hydrodynamic features were likely a result of the accelerations of the flow in at least one component of velocity causing some shear.
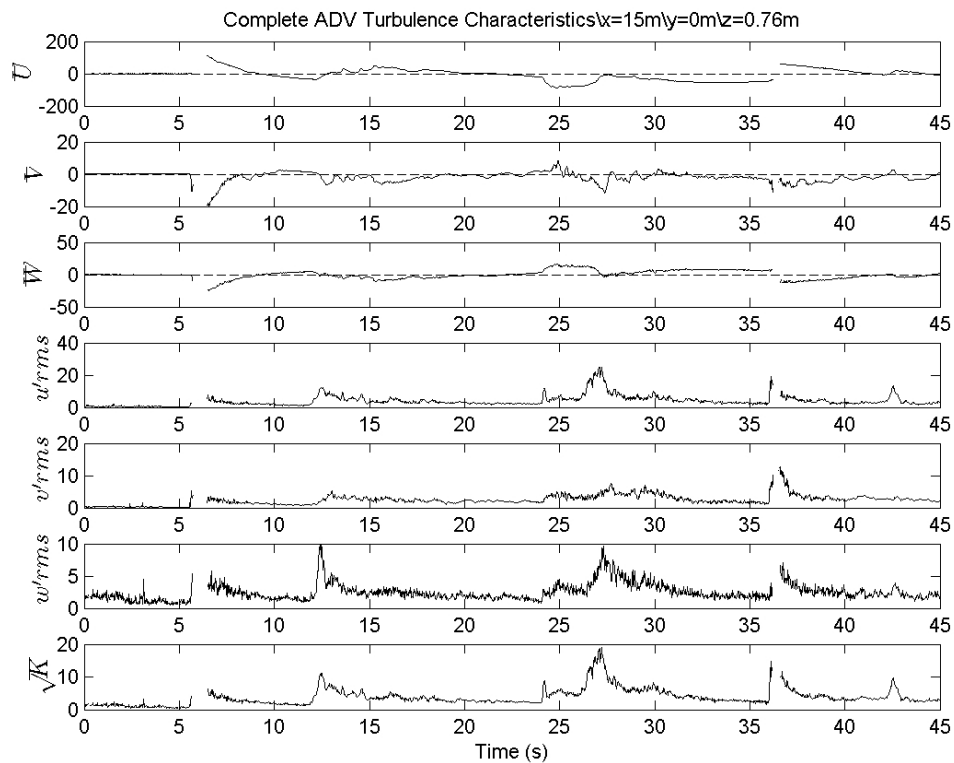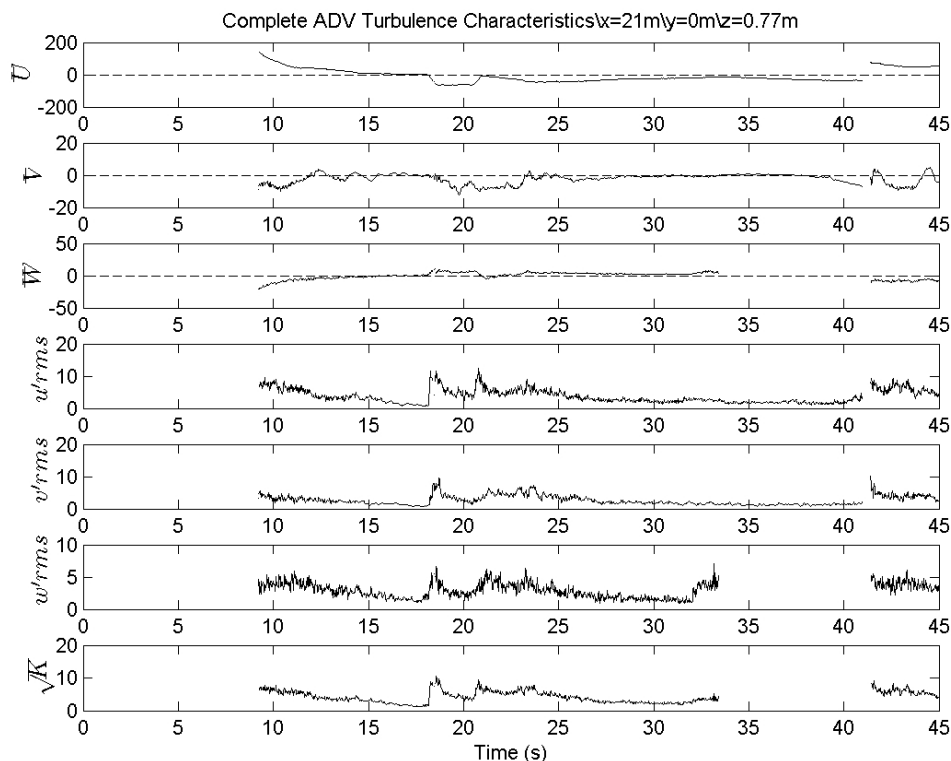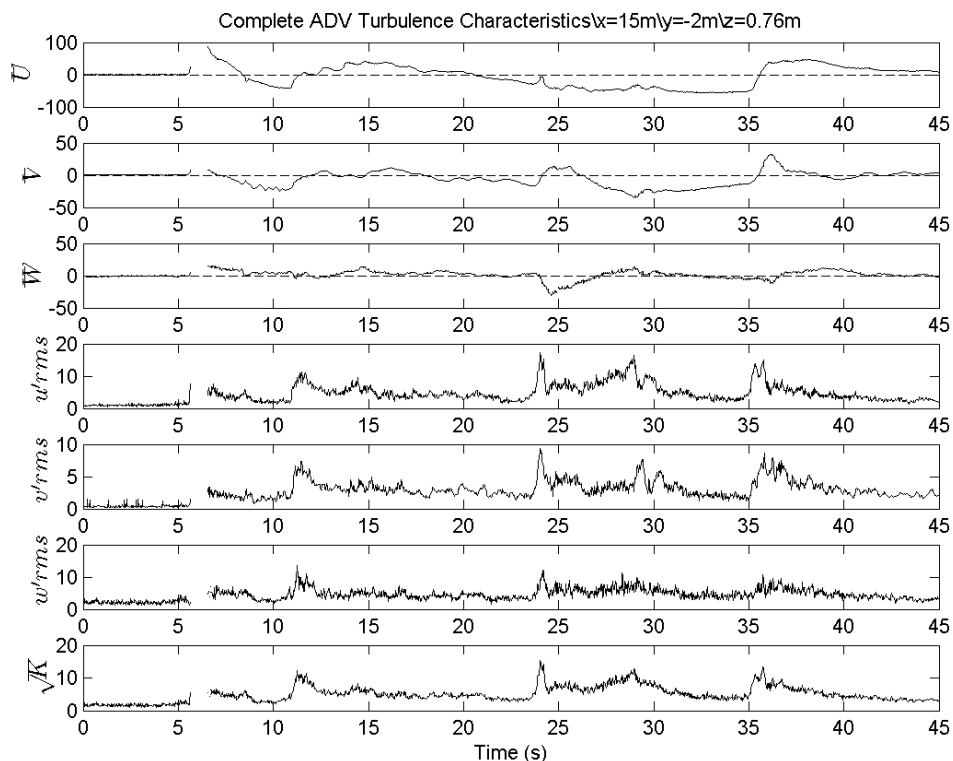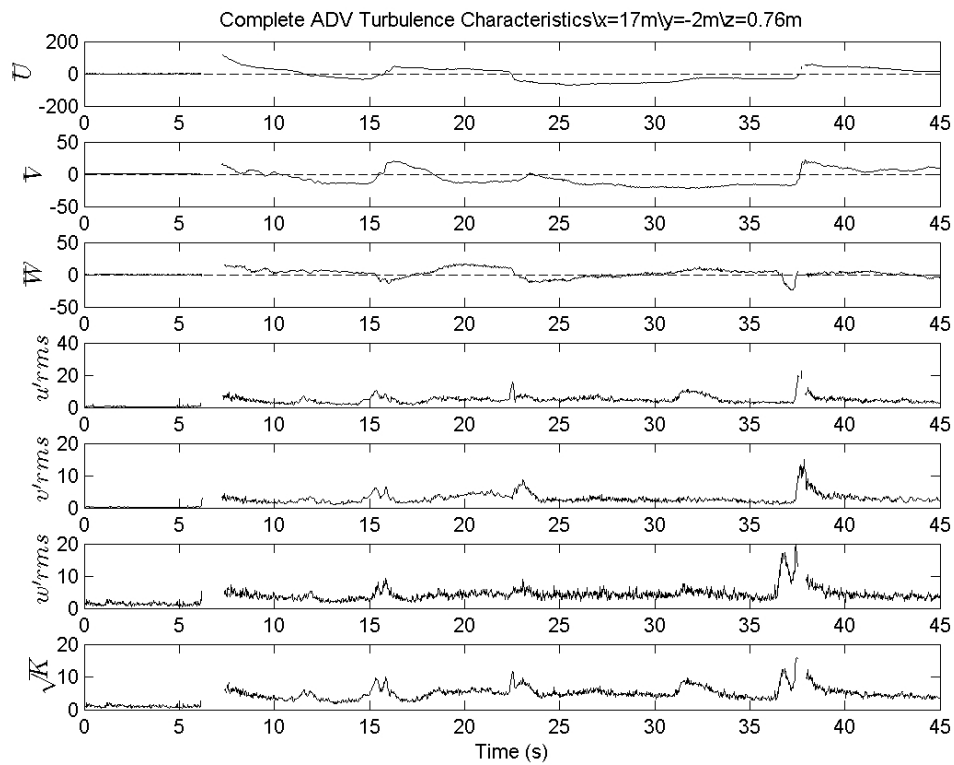
Figure 17:  Mean velocity (cm/s), RMS turbulence (cm/s), and $\sqrt{K}$  (cm/s) of ADV co-located with WG at X=15.0m, Y=0m, Z=0.76m.

Along Transect A, but further onshore at X=17m, Y=0m, Figure 18 shows that the turbulent events in the $\sqrt{K}$ timeseries associated with borefronts (1) through (4) were correlated at times around 7, 16.5, 23, and 38 seconds, respectively.  Three other turbulent event at 11, 14, and 31 seconds were attributed to conditions that were specific to the ADVs location.  At 11 and 14 seconds, after borefront (1) passed two small wakes developed traveling offshore due to the spanwise tube of air that was trapped ejected jet of water and the wave front being pushed out the back of the wave.  The two wakes were directed offshore with the offshore flow associated the drawn down of the water preceding borefront (2).  The offshore directed flow can be seen specifically in Figure 9b

although the wakes are not present at the time displayed by the image. The turbulent

event at 31 seconds is a direct result of the borefront created by the converging wakes

traveling onshore which were detected at X=15m, Y=0m after borefront (3) had

propagated offshore.
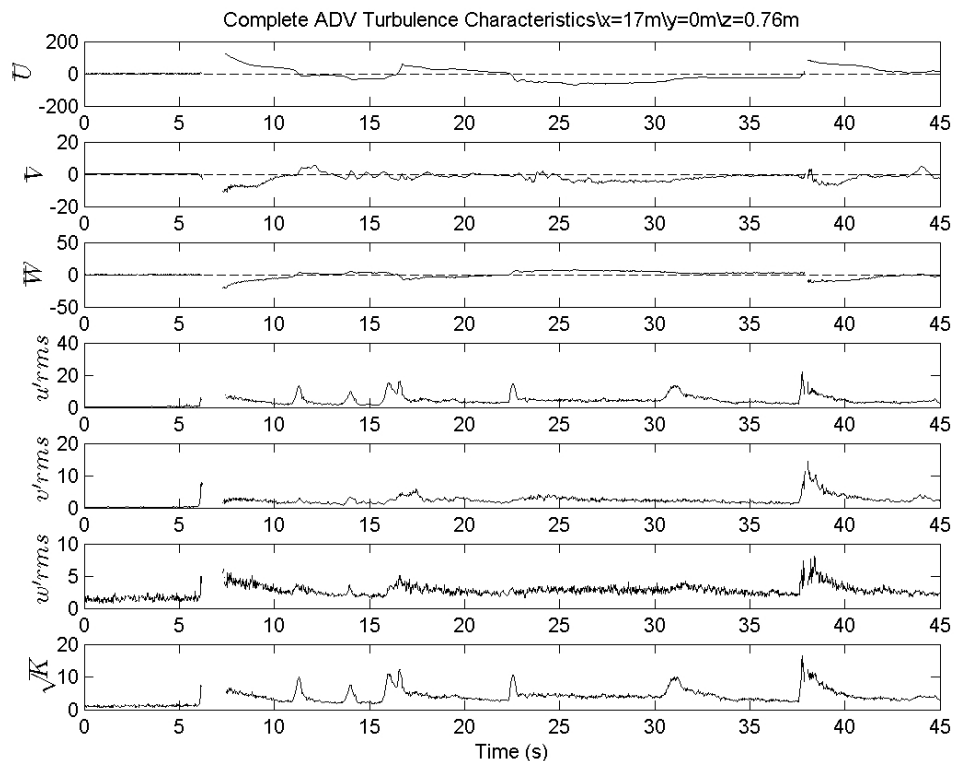


Figure 18:  Mean velocity (cm/s), RMS turbulence (cm/s), and $\sqrt{K}$  (cm/s) of ADV co-located with WG
at X=17.0m, Y=0m, Z=0.76m.

At the furthest onshore location along Transect A, the ADV at X=21m, Y=0m is

shown Figure 19 revealing that turbulent events were well correlated with borefronts (1)

through (4) in the $\sqrt{K}$ timeseries at times around 8, 21, 18, and 41 seconds, respectively.

Again, turbulent events that were revealed and that could not be correlated with specific

hydrodynamic features were likely the result of the accelerations of the flow in at least one component of velocity.



Figure 19: Mean velocity (cm/s), RMS turbulence (cm/s), and $\sqrt{K}$ (cm/s) of ADV co-located with WG at X=21.0m, Y=0m, Z=0.77m.

Moving away from the centerline to Transect C, the most offshore ADV location on the shelf was at X=15m, Y=-2m. Figure 20 shows the turbulent events in the $\sqrt{K}$ timeseries were well correlated with borefronts (1) through (4) at times around 6, 12, 24, and 36 seconds, respectively. The turbulent event that occurs at 29 seconds was due to the wakes that followed borefront (3) along the shelf edge and converged as

describe in Figure 9e and Figure 12. After the wakes collided creating a small borefront, they dispersed outward over the shelf.



Figure 20: Mean velocity (cm/s), RMS turbulence (cm/s), and $\sqrt{K}$ (cm/s) of ADV co-located with WG at X=15.0m, Y=-2m, Z=0.76m.

Further onshore along Transect C, at X=17m, Y=-2m the turbulent events associated with borefronts (1) through (4) can be seen in the $\sqrt{K}$ timeseries in Figure 21 at times around 6.5, 16, 22.5, and 37 seconds, respectively. Again, the turbulent event at 32 seconds was due to the wakes, generated along the shelf edge as borefront (3) converged on the apex, spreading outward over the shelf.

Figure 21: Mean velocity (cm/s), RMS turbulence (cm/s), and $\sqrt{K}$ (cm/s) of ADV co-located with WG at X=17.0m, Y=-2m, Z=0.76m.

The furthest onshore ADV location in Transect C was at X=21m, Y=-2m. Figure 22 shows the turbulent events in the $\sqrt{K}$ timeseries associated with borefronts (1) through (4) correlated at times around 8, 21, 18, and 41 seconds, respectively.
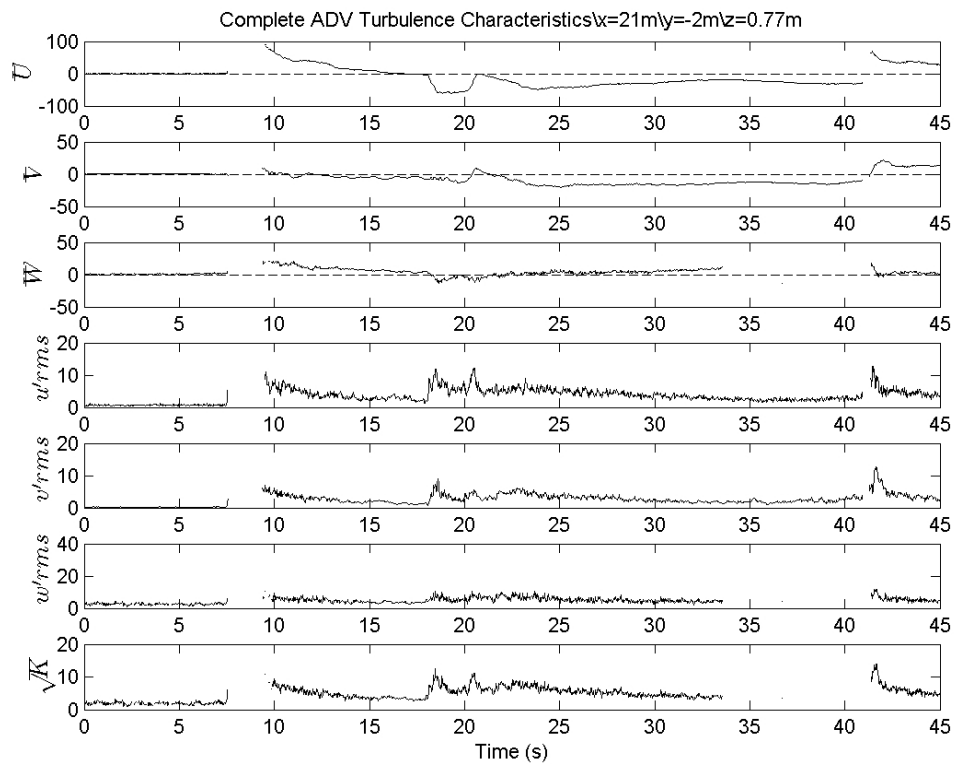
Figure 22: Mean velocity (cm/s), RMS turbulence (cm/s), and $\sqrt{K}$ (cm/s) of ADV co-located with WG at X=21.0m, Y=-2m, Z=0.77m.

Moving to Transect D, located the furthest from the centerline, the most offshore location of an ADV located on the shelf was at X=17m, Y=-5m. The turbulent events in the $\sqrt{K}$ timeseries associated with borefronts (1) through (4) were shown to be well correlated in Figure 23 at times around 7, 12, 22.5, and 35 seconds, respectively.
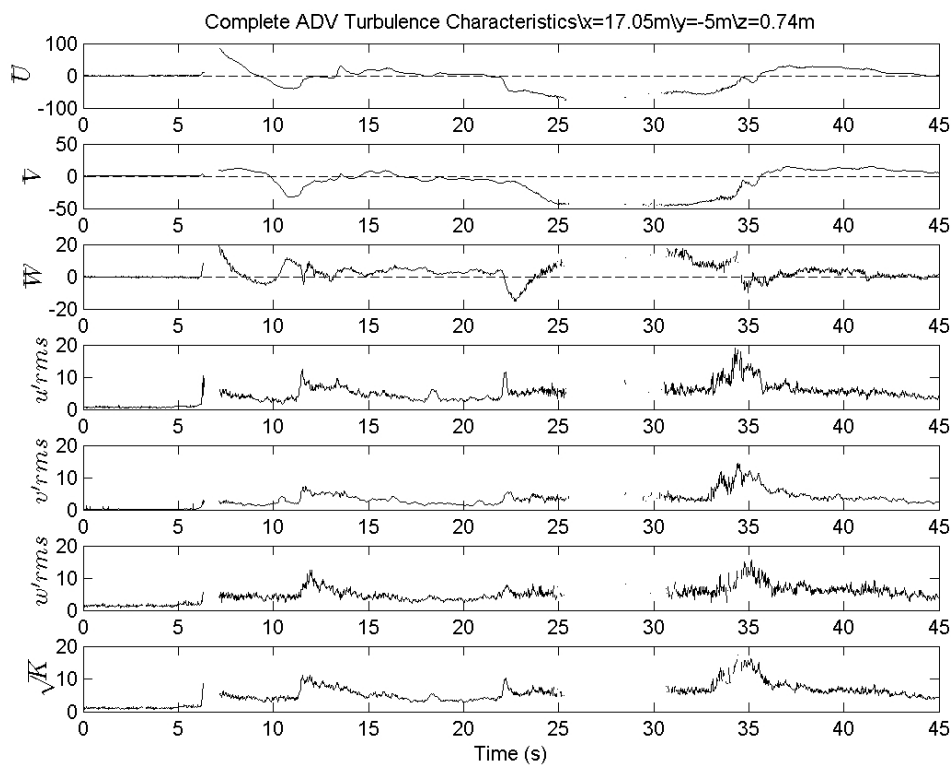
Figure 23: Mean velocity (cm/s), RMS turbulence (cm/s), and $\sqrt{K}$ (cm/s) of ADV co-located with WG at X=17.0m, Y=-5m, Z=0.74m.

The furthest onshore ADV location along Transect D was located at X=21m, Y=-5m. The turbulent events in the $\sqrt{K}$ timeseries associated with borefronts (1) through (4) were shown to be well correlated in Figure 24 at times around 7.5, 18, 18, and 40 seconds, respectively. Borefronts (2) and (3) were portrayed as the same turbulent event because the passed through each other at this ADV location.
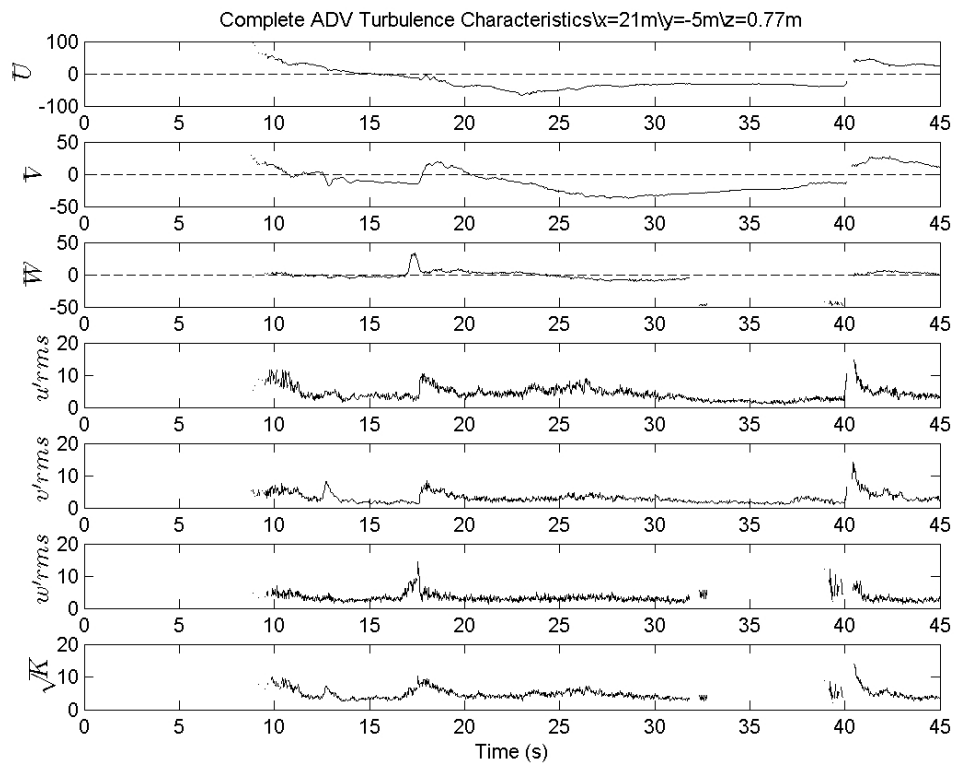
Figure 24:  Mean velocity (cm/s), RMS turbulence (cm/s), and $\sqrt{K}$ (cm/s) of ADV co-located with WG at X=17.0m, Y=-5m, Z=0.77m.

From analyzing Figure 15 through Figure 24, it was concluded that the large turbulent events recorded by the ADVs located on top of the shallow water shelf were a direct result of passing borefronts.  The borefronts that were identified both visually and through the WG data could be well correlated with total turbulent kinetic energy obtained from the ADV velocity measurements.  The major borefronts, (1) through (4), could be identified at every ADV location along with the other minor wakes and borefronts that were observed as they propagated over the shelf.  As expected the complex, shallow water bathymetry had a major influence on the turbulence that developed since it had a major impact on the hydrodynamics throughout the basin after

the initial solitary wave was generated.  The strong flow driven by both gravity and propagating borefronts forced had a great influence on the turbulence that development in both time and space.  A complete set of the mean flows and turbulence characteristics recorded by all the ADVs both onshore and offshore of the shelf edge are presented in Appendix II.

# 7.0 REFRACTION OF GENERATED SOLITARY WAVE

From the images displayed in Figure 9, the effects of the shallow water shelf on the borefronts were revealed.  In particular, the refraction and bending of borefronts (1), (2), and (4) was shown by the parabolic shapes as they propagated onshore.  Refraction refers to the bending of the wave front due to interactions with the bathymetry as it propagates into shallow water and begins to orient itself parallel to the depth contours (Dean & Dalrymple, 1991).  Due to the speed with which borefront (1) was traveling, the bending of the borefront in the longshore direction was not as pronounced.  To reveal the refraction of the solitary wave over the shelf, red and green dye was injected into the water at five points along the shelf edge while the wave passed from the bottom to the top of the images shown in Figure 25.

The images A-E show the injection points starting at the apex and moving along the shelf edge away from the centerline, respectively, and the resulting streamlines outlining direction of the flow following the solitary wave. The streamline in image A is straight since there was no refraction at the apex due to the symmetry of the bathymetry. In images B and C, the streamline near the shelf edge bent toward the centerline before beginning to straighten out further onshore.  The streamlines in images D and E confirmed that the effects of refraction extended the width of the basin to the side wall. The streamlines closer to the basin side wall were directed more toward the centerline as compared to images B and C  indicating that the amount of refraction increased

proportional to the distance from the centerline.  The increased refraction with distance from the centerline was also proportional to the acceleration the wave front experienced which greatly influenced its parabolic shape.  Also, the streamlines directed toward the centerline indicated that there was a convergence of water mass near the centerline as the borefront traveled over the shelf.  These forces that the wave experienced traveling over the shelf greatly affected the runup on the planar beach shoreward of the SWS and will be discussed in Sections 8.2 and 8.3.
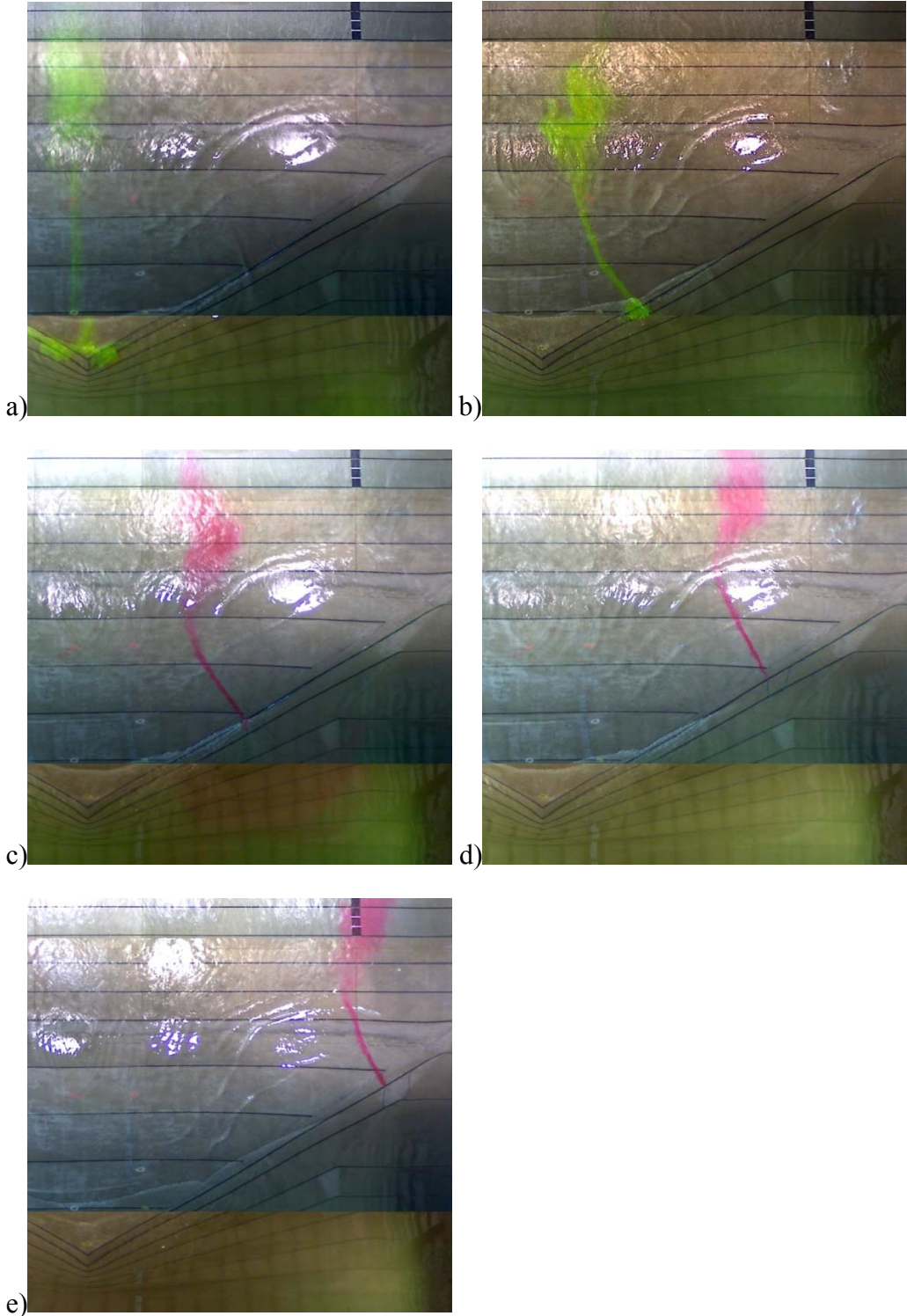
Figure 25:  Streamlines after the solitary wave, borefront (1).

# 8.0 RUNUP OF THE GENERATED SOLITARY WAVE ON THE

# PLANAR BEACH

With the hydrodynamics of the basin and the evolution of the generated solitary wave over the shallow water shelf understood, the next area of interest is shoreward of the SWS. Specifically, the area included the planar beach extending beyond the SWS at X=25.75m where the usWG were used to track the wave's runup due to the very shallow depth of the flow. By tracking the runup, the velocity in the cross-shore direction (U component) was then determined.

## 8.1 usWG Validation

Before the usWG data was accepted, they were validated against medium WGs at co-located locations offshore of the SWS. As explained in Section 2.2.1, the medium WGs were positioned at the cross-shore location X=25m and in the longshore locations including Y=0, -2, -5, -7, and -10m, while the usWG were located at X=25m at longshore locations including Y=0, 2, 5, 7, and 10m. Due the symmetry of the basin that was established in Section 4.2, the usWG were mirrored about the centerline co-locating the medium WGs and the usWGs. After comparing the timeseries, it was determined that the data collected by the usWG was in good agreement with the WG timeseries. For example, the nearly identical timeseries obtained at X=25m, Y=0m with the WG (lines) and the usWG (dots) are shown in Figure 26. Looking at the maximum and minimums revealed by the timeseries, there are some discrepancies, but this was expected due to the

fact that measurement techniques were different and there was air entrained in the water as the borefront (1) passed the instruments. Despite this, the general timeseries confirmed and validated the use of the usWG shoreward of the SWS.

A complete set of the runup timeseries recorded by the usWG is presented in Appendix III.
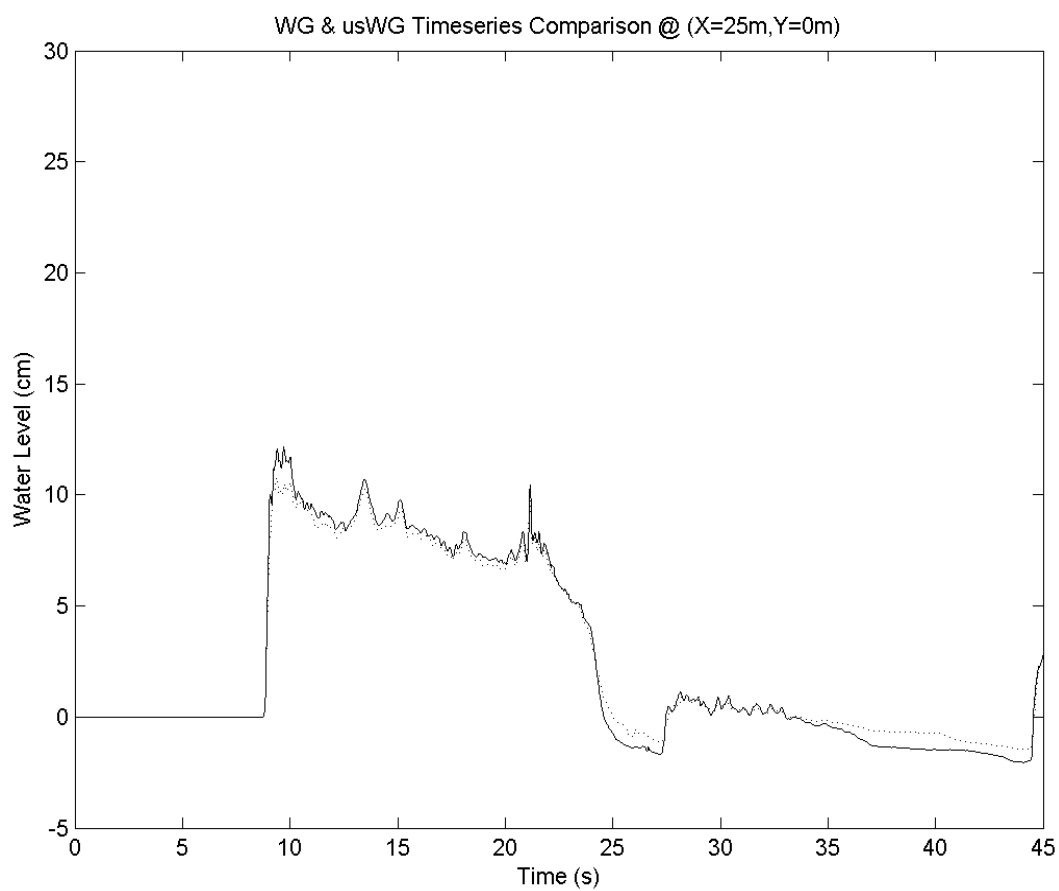


Figure 26: Comparison of WG (line) and usWG (dots) timeseries at X=25m, Y=0m.

## 8.2 Longshore Variation

After the mirroring usWG locations, the area shoreward of the SWS where usWG data was collected is outlined by the black box in the image displayed in Figure 27. From the usWG timeseries, the runup of the generated solitary wave was analyzed as it traveled up the planar beach in the cross-shore direction.

The runup of the solitary wave was tracked shoreward of the SWS by determining the time it arrived at each usWG. By extracting the runup's arrival time, its longshore variation (shape) as it traveled up the beach in the cross-shore direction was revealed as shown in Figure 28. The figure displays the arrival time of borefront (1) as it entered the area of the black box from left to right as shown in Figure 27. Naturally, the earliest arrival times occurred near X=27m after about 9 seconds, while the latest arrival times occurred at X=39m after about 16 seconds. The contour lines of constant time revealed that the runup's shape was not uniform as it traveled up the beach. For example, at X=29m the borefront arrived first near the basin side wall as compared to the centerline. We believe that the later arrival time near the centerline of the basin at X=29m was due to the effects of refraction as borefront (1) propagated over the shallow water shelf. Once the runup had reached X=39m, the borefront was still not uniform and had an earlier arrival time along the centerline as compared to near the wall. The change in the orientation of the runup revealed that there was a change in its cross-shore velocity as it traveled up the beach.
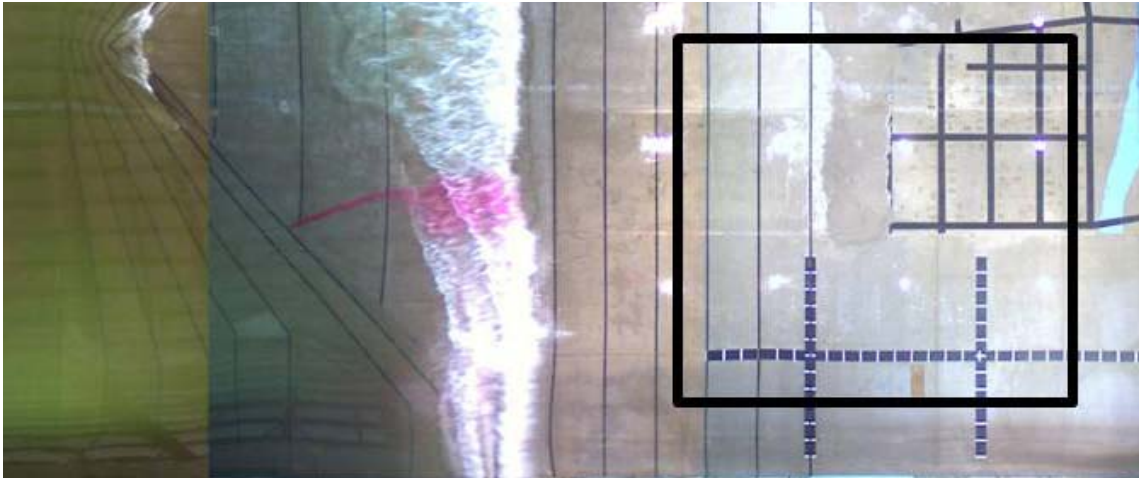
Figure 27: Black box denotes area of usWGs, which were used to track the generated solitary wave borefront runup.
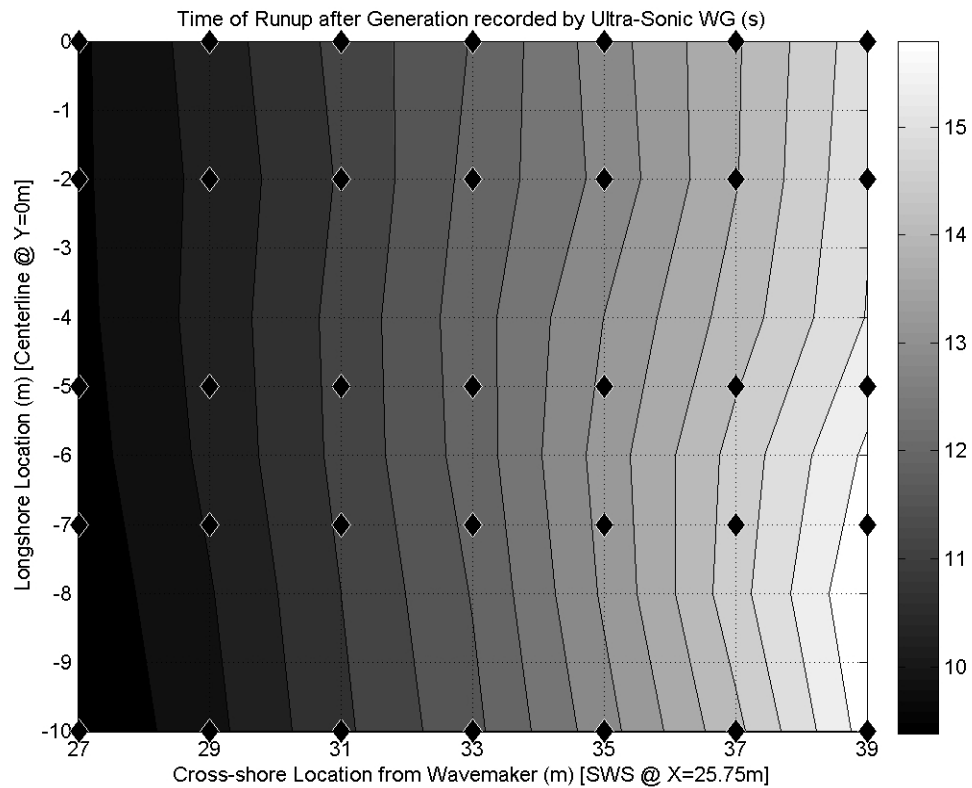


Figure 28: The arrival time, in seconds as recorded by the usWG, of the solitary wave borefront on the planar beach shoreward of the SWS. (◆) represent usWG locations.

**8.3 Cross-shore Velocity**

Realizing that cross-shore velocity of the runup was not constant, finite differencing used to calculate it based on the arrival times of the runup with respect to the known locations of the usWG. Figure 29 revealed that the greatest velocity occurred at X=27m near the centerline of the basin, while the lowest velocity occurred at X=39m near the basin side wall. We believe that the greater velocity along the centerline was due to a jetting mechanism created after the wave refracted and became parabolic in shape over the shelf. After reaching the planar beach, the forces causing the convergence of water along the centerline were relaxed and the stabilizing effects of gravity forced water in the direction of propagation and laterally along the borefront. The jetting caused the greatest velocity to initially be concentrated near the centerline and spread laterally over time at each sequential cross-shore location as shown in Figure 29 at X=33m by the increasingly parabolic velocity contour lines near the basin side wall. It is believed that the initial shape, cross-shore velocity of the runup, and its variation as it traveled up the beach were greatly influenced by the bathymetry offshore of the SWS.
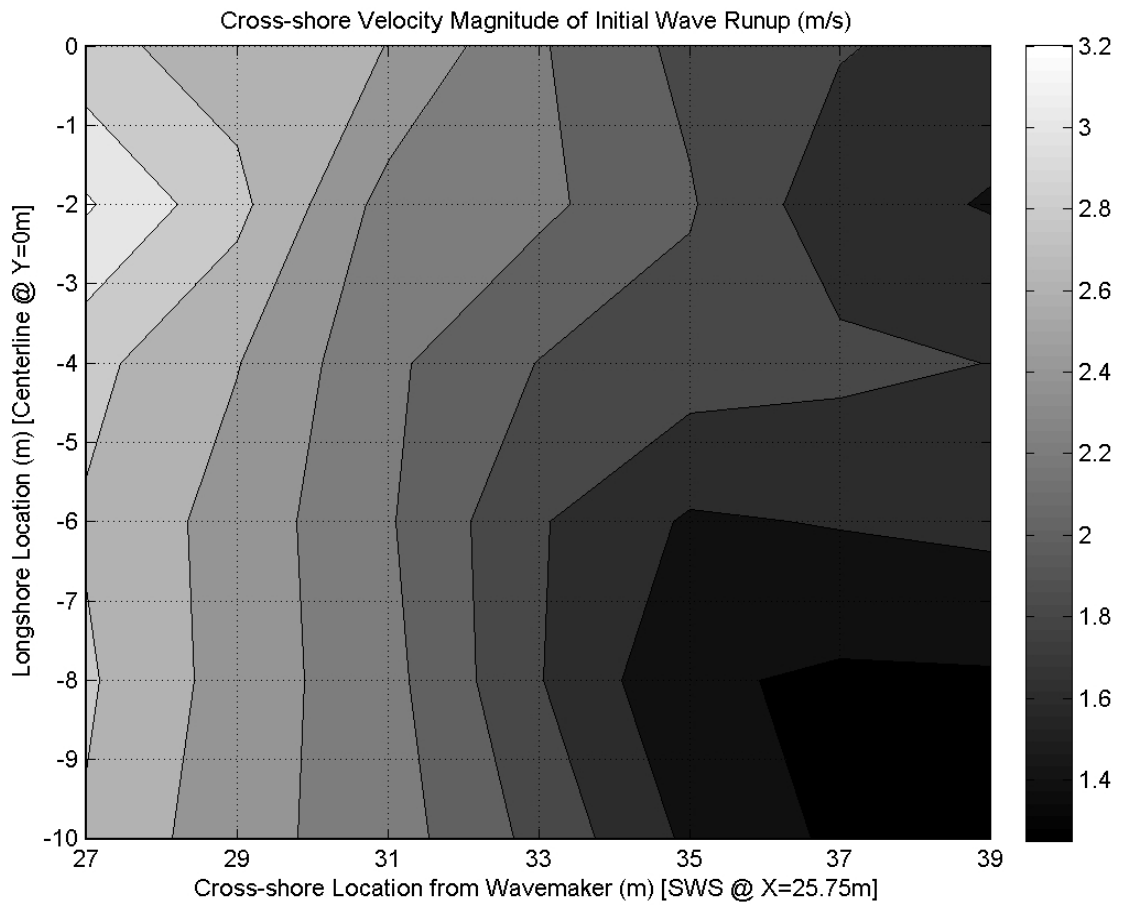
Figure 29: U component of the borefront velocity above the SWS on the planar beach as recorded by the usWG.

# 9.0 MEASUREMENTS AND OBSERVATIONS OF LARGE-SCALE STRUCTURES DURING RUNDOWN

Now that the complete hydrodynamics of the basin has been described, the other particular area of interest was the formation of a turbulent structure (eddy) that formed offshore of the shelf edge near the basin side wall as shown within the white circles in Figure 9f through Figure 9h.  It formed after borefront (3) had propagated offshore of the shelf's apex and persisted as borefront (4) arrived and traveled onshore over the shallow water shelf.  The eddy was considered a three dimensional coherent structure because it persisted over a considerable period of time and its horizontal area was large as compared to the water depth.  In the past, the eddy that formed would have been classified as a two-dimensional coherent structure, but our experiment revealed that the flows associated with the eddy actually varied strongly with depth adding a third dimension to its structure.  In this section, the formation of the eddy will be discussed and its three-dimensionality will be confirmed.  To do this, the eddy will be shown at multiple time steps over a 2.10 second period between the images shown in Figure 9f through Figure 9g.

## 9.1 Eddy in Planview

The coherent turbulent structure that developed was due to the combination of the strong offshore flow on top of the shallow water shelf following borefront (3) and the abrupt change in the bathymetry at the shelf edge which is the strongest mechanism for

generating two-dimensional coherent structures (Socolofsky & Jirka, 2004). The strong offshore flow along with the change in bottom slope caused a shear layer to develop along the shelf edge which was revealed by the hydraulic bore as seen in Figure 9f. The instability of the shear layer in turn produced the eddy which detached and shed off into deeper water with the mean offshore flow. The eddy was able to persist over time even with the change in mean flow following borefront (4) because it was generated by unsteady offshore flow which increased its rotation (Signell & Geyer, 1991).

To understand the eddy, the mean horizontal velocity and turbulent data obtained with the ADVs were displayed in three horizontal planes spaced vertically throughout the water column. The horizontal planes starting near the water surface were positioned at $Z=0.74m$, $0.63m$ and $0.52m$ and included both bottom mounted and bridge mounted ADVs. The deeper water depths ($Z=0.63m$ and $0.52m$) were obtained by using the vertical stacks of ADVs mounted to the bridge and position offshore of the shelf edge as shown in Figure 2. Due to the bathymetry and the filtering of the data, each horizontal plane did not contain every ADV location. For example, at the lower elevations ($Z=0.63m$ and $0.52m$), the horizontal planes did not include ADVs positioned on the shelf due to the shallow water depth. Also, other ADV locations did not randomly appear in the horizontal planes due to the filtering of the raw data which eliminated unreliable data similar to the timeseries shown in Section 6.3.

The time period chosen to describe the eddy began at 33.8 seconds and continued until 35.9 because it showed the eddy's development during the offshore flow following borefront (3) and it persistence after the onshore flow following borefront (4) had begun.

At 33.8 seconds, borefront (3) had propagated offshore of the apex of the shelf and the strong offshore flow that followed was present generating the shear layer which was revealed by the hydraulic bore along the shelf edge as shown in Figure 30. The eddy rotating counter clockwise can be seen by the green dye that extended offshore of the edge and had become concentrated near the ADVs located at furthest onshore and toward the centerline within the white circle.
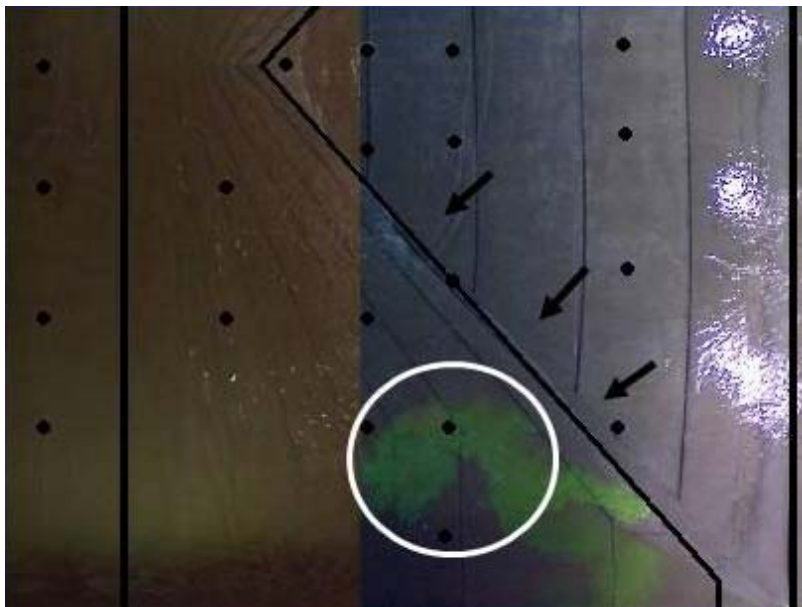


Figure 30: Picture of the basin from above 33.8s after the solitary wave was generated. (●) indicate the location of ADVs.

Figure 30 provides a visualization of the basin hydrodynamics at 33.8 seconds, but to understand the fluid flow the horizontal velocity and total turbulent kinetic energy at all three elevations were required. At an elevation Z=0.74m, the horizontal plane closest to the water surface, the left plot in Figure 31 shows the horizontal velocity at

each ADV which are denoted by the arrows, while the right plot shows the turbulent energy magnitudes. The horizontal velocities on the shelf are strongly directed offshore perpendicular to the shelf edge. The greatest magnitudes of about 0.5 m/s occur along the edge and were drastically reduced offshore of the edge. The advection of the dye due to the presence of the eddy as shown in Figure 30 was confirmed by the greatest horizontal velocity offshore of the shelf edge occurring at near the ADV located at X=17m, Y=-9m. Similarly, the greatest turbulent energy, characteristic of coherent structures, was contained at the same location further validating the eddy that was revealed by the dye.

Moving deeper in the water column to Z=0.63m, Figure 32 continues to reveal the eddy near the ADV at X=17m, Y=-9m. At this water depth, the only data available was from the ADVs located offshore of the shelf edge due to the bathymetry. The magnitudes of most the ADVs horizontal velocities were small and directed onshore indicating the arrival of borefront (4). Again, at X=17m, Y=-9m, the velocity was directed offshore with the greatest magnitude of 0.25 m/s due to the eddy. Further offshore, the ADV at X=15m and Y=-9m recorded a minimal velocity also directed offshore and away from the centerline due to the eddy traveling to it most offshore point before the flow changed directions due to borefront (4). Looking at the turbulent energy, again, the only recorded energy occurred at these ADVs confirming that the eddy's center of rotation was between the two ADVs and slightly toward to the basin side wall.

The third horizontal plane of instruments was located at Z=0.52m and shown in Figure 33. Again, the ADV located at X=17m, Y=-9m recorded fluid velocity directed

offshore which was opposite of the other ADV locations and experienced the only

turbulent energy at this elevation. The reduced magnitude of the velocity near the

bottom at the ADV of interest may have been a result of the bathymetry's bottom

frictional effects since the bottom was located at Z=0.49m. Because the eddy was

detected throughout the complete depth of the water column, its classification as a two-

dimensional coherent structure is validated.
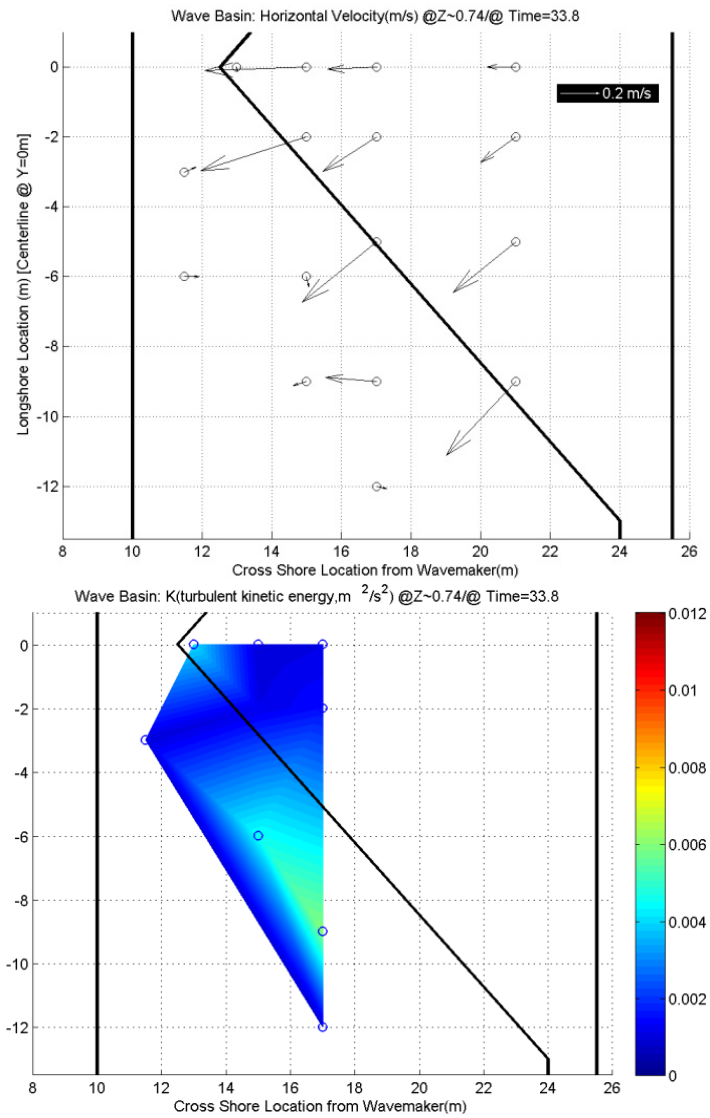
Figure 31: Horizontal velocity magnitude/direction (m/s) with K ($m^2/s^2$) at 33.8s and Z=0.74m.
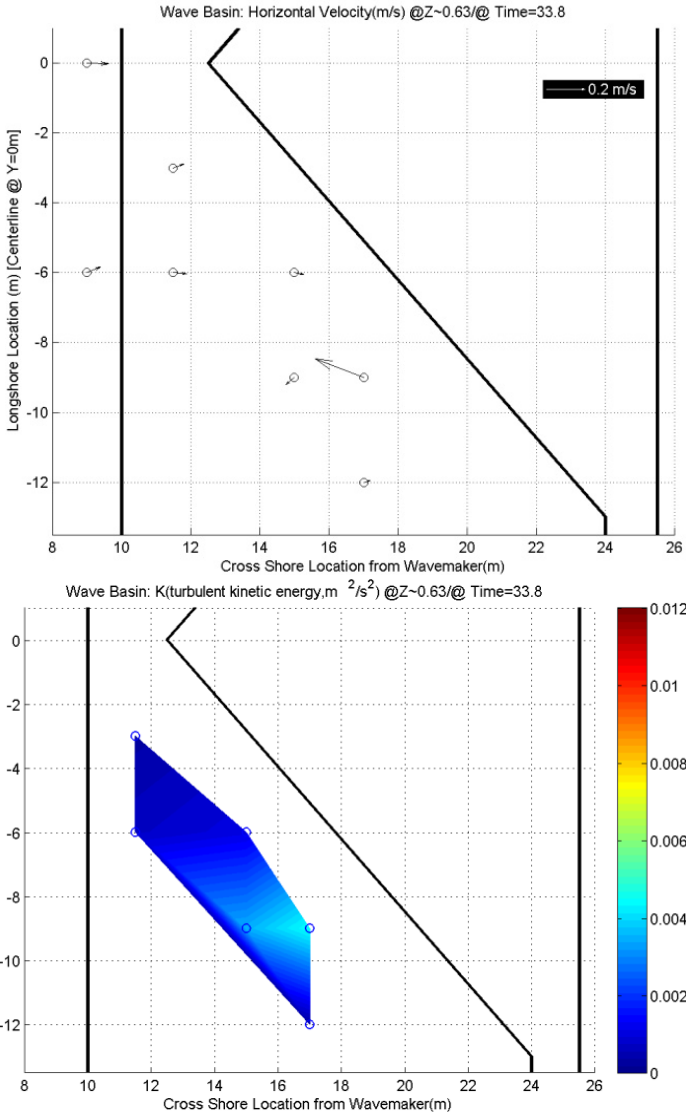
Figure 32: Horizontal velocity magnitude/direction (m/s) with K (m$^2$/s$^2$) at 33.8s and Z=0.63m.
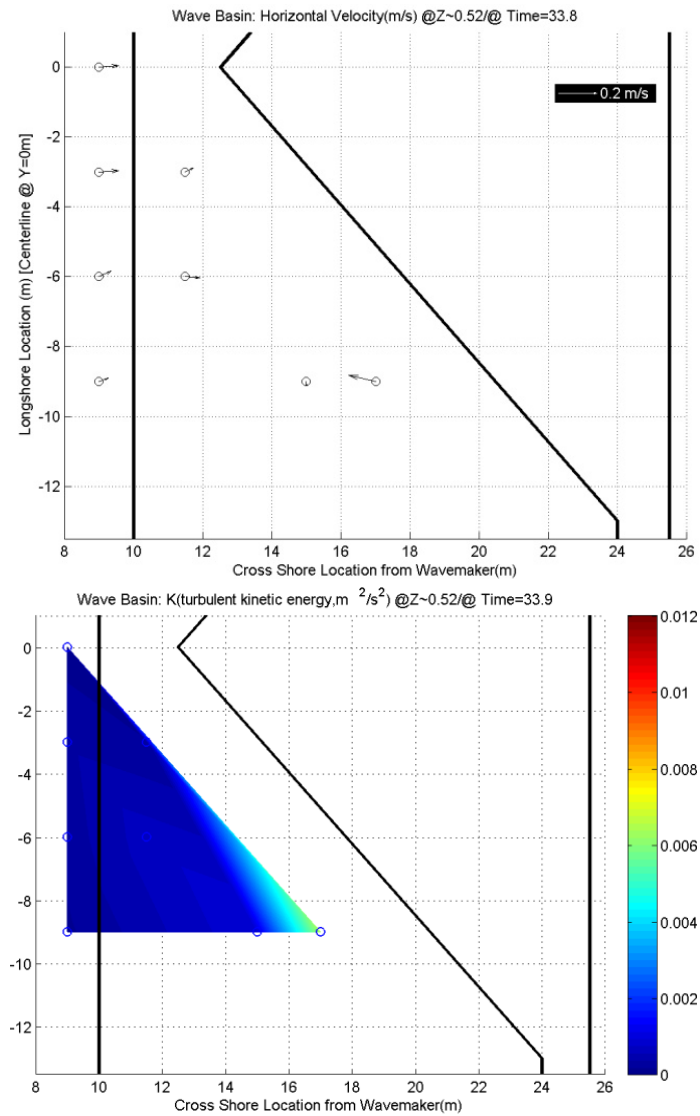
Figure 33:  Horizontal velocity magnitude/direction (m/s) with K ($m^2/s^2$) at 33.8s and Z=0.52m.

Stepping forward in time to 35.9 seconds; borefront (4) traveling onshore began to appear on the shelf as shown in Figure 34.  Borefront (4) was parabolic shaped borefront with its vertex onshore of the shelf apex.  The ADVs located at X=17m, Y=-9m, denoted by the black dot most shoreward and toward the centerline within the white circle, continued to experience the eddy's effects at it remained in the area.  The green

dye seen in the same area as at 33.8 seconds showed that the eddy's center of rotation

was still located slightly offshore and toward the basin side wall with respect to the

ADVs of interest even with the onshore flow following borefront (4).
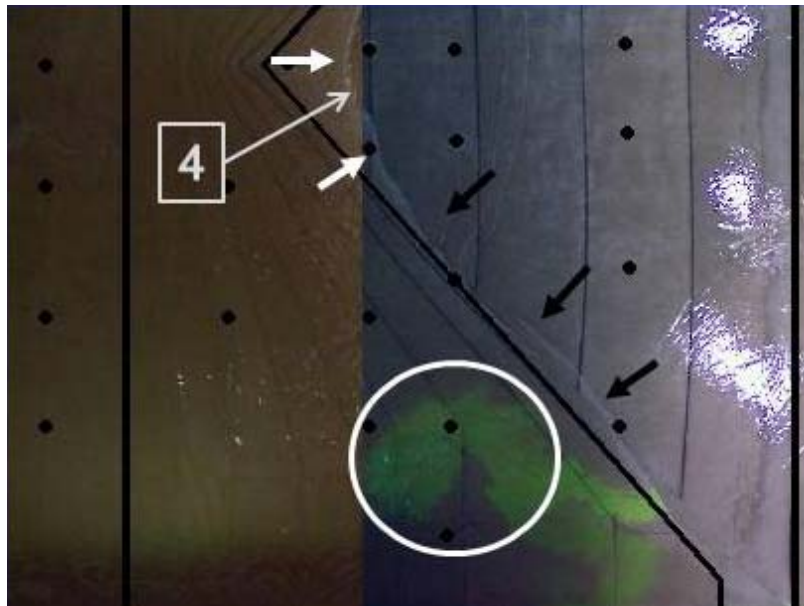


Figure 34:  Picture of the basin from above 35.9 s after the solitary wave was generated.  (●) indicate the location of ADVs.

At this point in time, the strong offshore flow continued over much of the shelf,

but at the edge it had ceased due to the arrival of borefront (4).  This is confirmed by the

strong change horizontal velocities near the shelf edge from offshore to onshore as

shown in Figure 35 at $Z=0.74m$.  Onshore of the borefront the velocities are directed

offshore, while offshore of the borefront the velocities are directed onshore.

Interestingly in the area of the eddy, the ADV at $X=17.0m$, $Y=-9m$ was the only location

offshore of the borefront that was not directed onshore.  The magnitude of the velocity at

this location was reduced due to the fact that the cross-shore component directed offshore was resisting the mean onshore flow following borefront (4). Looking at the turbulent energy, Figure 35 agrees with conclusions made in Section 6.3 that significant turbulence occurred under the borefronts and in areas of converging flows. The turbulence was greatest under the borefront near the shelf edge at X=15m, Y=-2m and at X=17m, Y=-5m, while the only other location of significant turbulence was at X=17m, Y=-9m. At this offshore point, the onshore flow following borefront (4) was converging with the offshore flow caused by the rotating eddy.

At a lower elevation, Z=0.63m, the horizontal velocity and turbulent energy in Figure 36 again confirmed the eddy's close proximity to the ADV at X=17m, y=-9m. In general, the velocity in the basin was directed in the onshore direction while at the ADV of interest the velocity was directed offshore and toward the centerline of the basin. As seen in Figure 35, the offshore component of the eddy's flow resisted the onshore flow and created an area of convergence which was revealed by the area of increased in turbulent kinetic energy.

Moving to the horizontal plane closest to the bottom at Z=0.52m, Figure 37 shows the onshore flow due to borefront (4) was still noticeable and caused the offshore flow expected from the eddy's rotation at X=17m and Y=-9m to be minimal. At this location the bathymetry was located at Z=0.49m which makes the explanation of the reduce velocity difficult. It is believed that the reduced velocity was due to a combination of the eddy's flow strongly resisting the onshore flow resulting in only a small net component of the velocity to be directed toward the centerline and frictional

effects due to the bottom. Again, the turbulence was greatest at this location due to the convergence of the flows near the eddy. The three horizontal planes confirm that the eddy extended from the water surface to the underlying bathymetry over an extended period of time even after the mean flow changed directions and validated its classification as a traditional two-dimensional coherent structure.
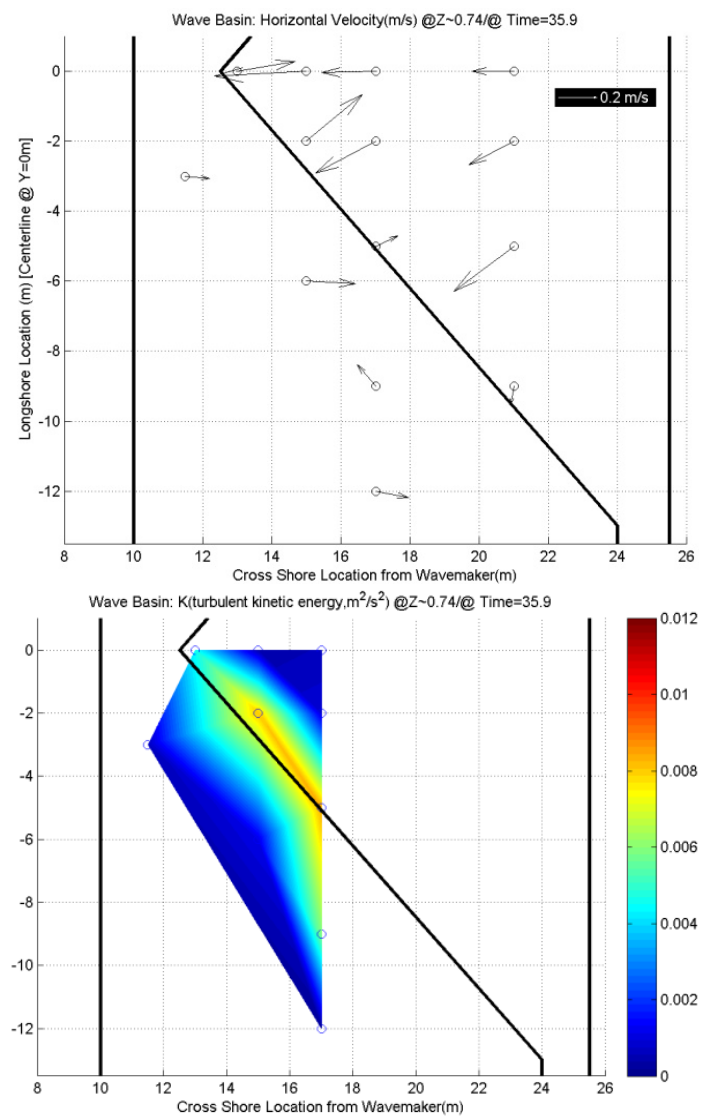
Figure 35: Horizontal velocity magnitude/direction (m/s) with K ($m^2/s^2$) at 35.9s and Z=0.74m.
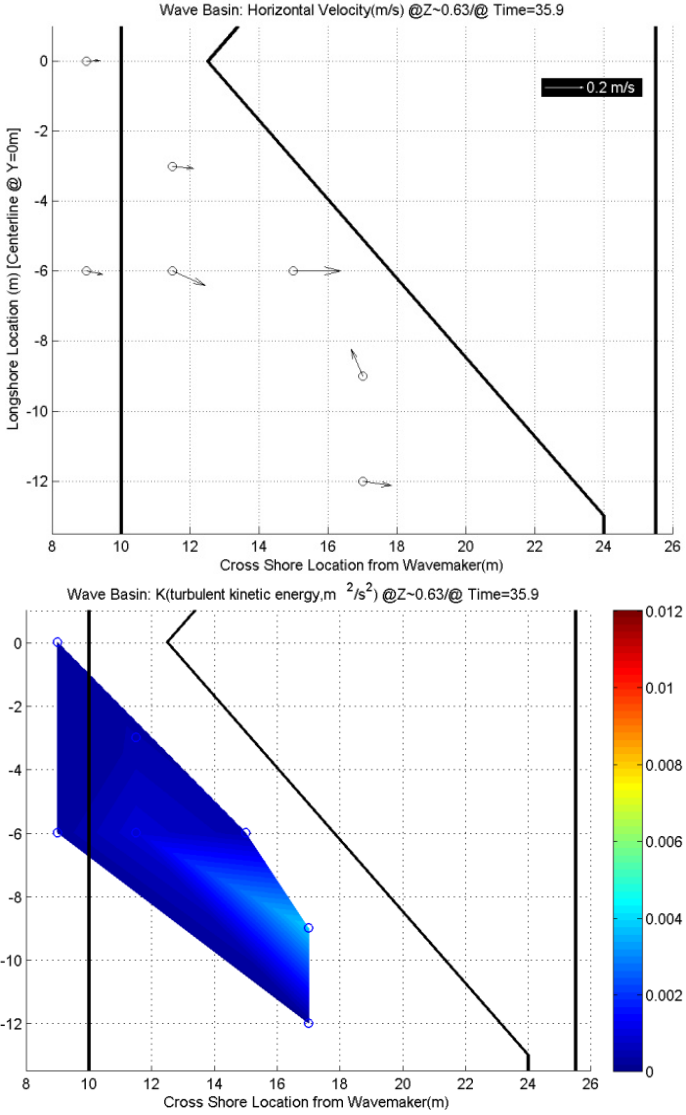
Figure 36: Horizontal velocity magnitude/direction (m/s) with K ($m^2/s^2$) at 35.9s and Z=0.63m.
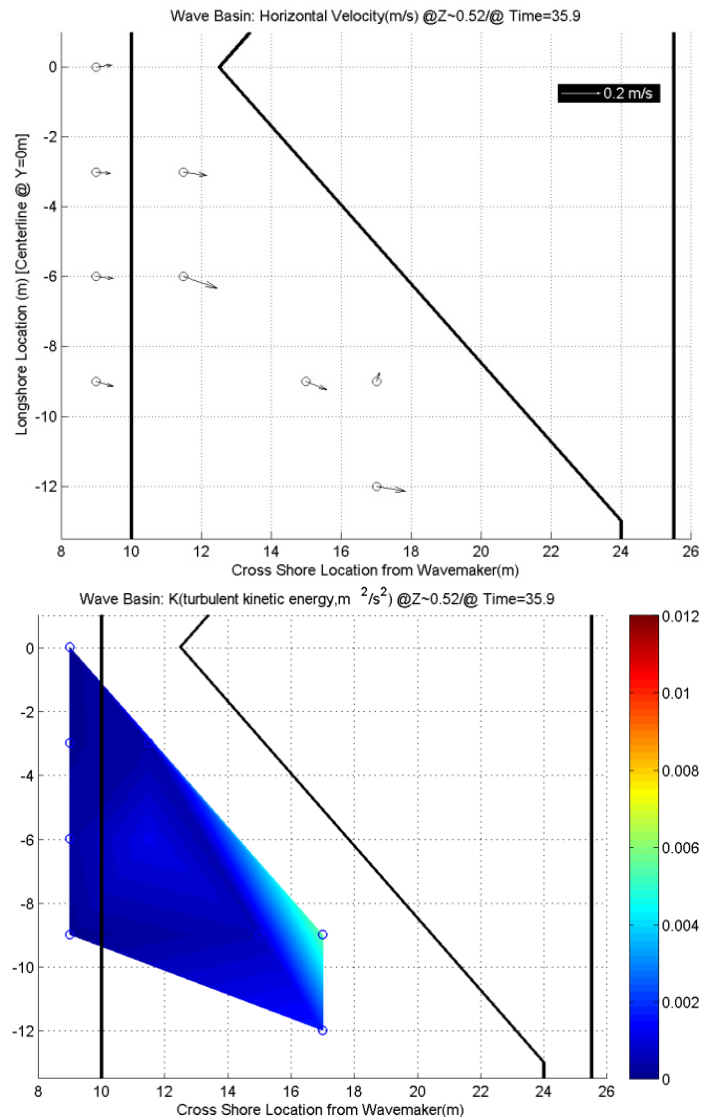
Figure 37: Horizontal velocity magnitude/direction (m/s) with K ($m^2/s^2$) at 35.9s and Z=0.52m.

## 9.2 Vertical Structure of Eddy with Depth

Section 9.1 investigated the coherent structure in multiple horizontal planes, but to understand the three-dimensional flows within the structure, the vertical profiles were analyzed. To completely describe the eddy that had been identified both visually with the dye and with the ADVs in the horizontal planes, the vertical profiles at X=17m, Y=-

9m were created at four selected time steps between 33.8 seconds and 35.9 seconds and presented below. The vertical profiles provided a means to relate the variations in velocity and turbulence for all three components with depth and time. Each vertical profile contains a mean velocity component ($\overline{U}$, $\overline{V}$ and $\overline{W}$), RMS turbulence component ($u'_{rms}$, $v'_{rms}$ and $w'_{rms}$), and the total turbulent kinetic energy ($\sqrt{K}$). Furthermore, the vertical profiles for all three components were created at time steps including 34.16, 34.70, 35.00, and 35.44 seconds. It should be noted that the total turbulent kinetic energy calculated was the same for all components at a given time and was presented in each profile for comparison purposes.

The vertical profiles are plotted with the vertical axis representing elevation (m) and the horizontal axis representing the magnitude of the various quantities (cm/s). Within each profile, the grey area shows the elevation of the underlying bathymetry (Z=0.49m) at X=17m, Y=-9m, the vertical dotted line represents the zero line to denoting directionality of the flow velocity, and the horizontal dotted line with the black triangle represents the water surface. Also, (✳) denotes mean velocity and (□) denotes RMS turbulence with respect to the directional component specified, while (Δ) denotes the square root of the total turbulent kinetic energy from all three components.

The vertical profiles that revealed the complex variations of the eddy's flow with depth are shown in Figure 38. In general, the profiles with respect each component exhibit similar depth varying profiles at each time step confirming the stability and consistency of the flows within the structure. Naturally, the turbulent kinetic energy was the same moving horizontally across the figure, but varied moving down the figure with

time.  Overall, the turbulent energy associated with the eddy remained constant with time, but the slight variations may have been due to the magnitude of the vertical shear of the velocity within the eddy coupled with the general movement of the eddy with respect the ADVs.  This made it very difficult to distinguish between reductions in the velocity and turbulence due to eddy's flow structure or orientation, but despite the complexity, some general features could be identified.

The magnitude of the U component of velocity, left column of Figure 38, decreased over time, but was strongly negative (directed offshore) due to the position of the eddy's center with respect to the ADVs at each time step revealing a logarithmic type profile.  The ADVs were positioned near the edge of the eddy's flow field causing most of its rotational velocity to be directed offshore as recorded.  The decay in the velocity magnitude with depth was due to the boundary frictional effects which cause velocities to approach zero near the bottom.  The RMS turbulence of the U component was fairly constant with time except in the last two time steps where it increased with depth due the shear.  We believe that the shear increased due to the bottom boundary layer that developed over the sloping bottom.  This may have been due to the magnitude of the velocities within the eddy coupled with the bathymetry and/or the eddy's orientation with respect to the ADVs.

The V component of velocity, middle column of Figure 38, was positive (directed toward the centerline of the basin) at each time step.  The vertical profiles were not constant with respect to time or depth revealing the complexity of the three-dimensional flows within the eddy.  The spike in the velocity at mid-depth, Z=0.63m, at

each time step showed that there were regions of smaller flow structures contained within the eddy. The smaller structures (vortex structures) were believed to likely resembled rotating tubes that form rings around the eddy's center when viewed from above and were positioned throughout the water depth (Lin, Ozgoren, & Rockwell, 2003). A vortex structure could be thought of as an individual, straight tube spinning with an axis of rotation along its length. Then the tube was bent connecting the ends of the rotating tube to create a ring around in a plane perpendicular to the eddy's axis of rotation. Lin et al. (2003) showed that the rings had various rotational directions and magnitudes which greatly affected the flows direction and magnitude within the eddy. Just as the vortex rings affected the velocity, the RMS turbulence profiles revealed variations in magnitude with depth and time. The diameter, positioning, and rotation of the multiple rings within the water column greatly affected the V component of the vertical profiles. The positioning of the ADVs with respect to the eddy and its rings revealed that there was generally an outward flow away from the eddy's center with a maximum near mid-depth.

Just as the vortex rings affected the velocity, the RMS turbulence profiles revealed great variation in magnitude with depth and over time. The diameter, positioning, and rotation of the multiple rings within the water column greatly affected the V vertical profiles with depth and over time. The positioning of the ADVs with respect to the eddy and its rings revealed that there was generally an outward flow away from the eddy's center with maximum near mid-depth.

Due to similar effects, the W component of velocity, right column of Figure 38, was negative (directed downward toward the bottom) at each time step. Again, the vortex rings greatly affected the vertical flow field within the eddy (Lin, Ozgoren, & Rockwell, 2003) due to their positioning and varying rotations. Like the V component, there was a spike at mid-depth revealing the stronger downward flow as compared to the rest of the water column confirming the three-dimensional dynamics within the eddy. Unlike the V component of the RMS turbulence, the W component was much more constant with depth and over time possibly due to the smaller velocity magnitudes and horizontal shear within the eddy. In general though, the magnitudes of the RMS turbulent fluctuations were on the same order of magnitude as the mean velocities at each time step, especially in the V and W components, confirming the large amount of turbulence characteristic of turbulent coherent structures.

Because of the single location of the vertically stacked ADVs that captured the eddy's flow field, it was very difficult to confidently describe orientation of the vortex rings and eddy with respect to the ADVs. One possible explanation of the eddy's internal flow field is presented in Figure 39. It was determined that the ADVs were located shoreward and toward the centerline from the eddy's center of rotation which as shown by the planview in Figure 39a. The filled dot represents the ADV stack while the larger circle represents the general location of the eddy. From the dye study, it was determined that the eddy's center was not stationary and wavered in the area of the ADV stack due to the change in flow direction. The crosses represent the general path of the eddy's center shoreward and toward the centerline following borefront (4). The

highlighted cross represents the starting location of the eddy's center at 34.16 seconds. The dashed line is the position of the vertical cross section displayed in the elevation view shown in Figure 39b, when viewed in the onshore direction.

The elevation view portrays the possible positioning of the vortex rings along with their rotations so that the flow field agreed with the vertical velocity profiles. The black arrow at the top of Figure 39b represents the center of the eddy and the highlighted vertical line represents the ADV stack. The flow field on each side of the eddy's center is shown given that the opposite side would contain complementing vortex structures (Lin, Ozgoren, & Rockwell, 2003). Given the vertically varying flows, the assumption of upward flow near the center, as shown, could be plausible (Geyer, 1993) agreeing with the three-dimensional structures (Lin, Ozgoren, & Rockwell, 2003). The strong downward outflow at mid-depth could be achieved by the close proximity of counter rotating vortex rings. The convergence and acceleration of the flow between the rings over the complete water depth would also explain the turbulence that was measured. The vortex rings' positions and flow fields presented are general and only provide a possible explanation of the inner dynamics of the eddy and a more detailed study either numerically or experimentally of the flow field would be required to more accurately depict the three-dimensional flow field.
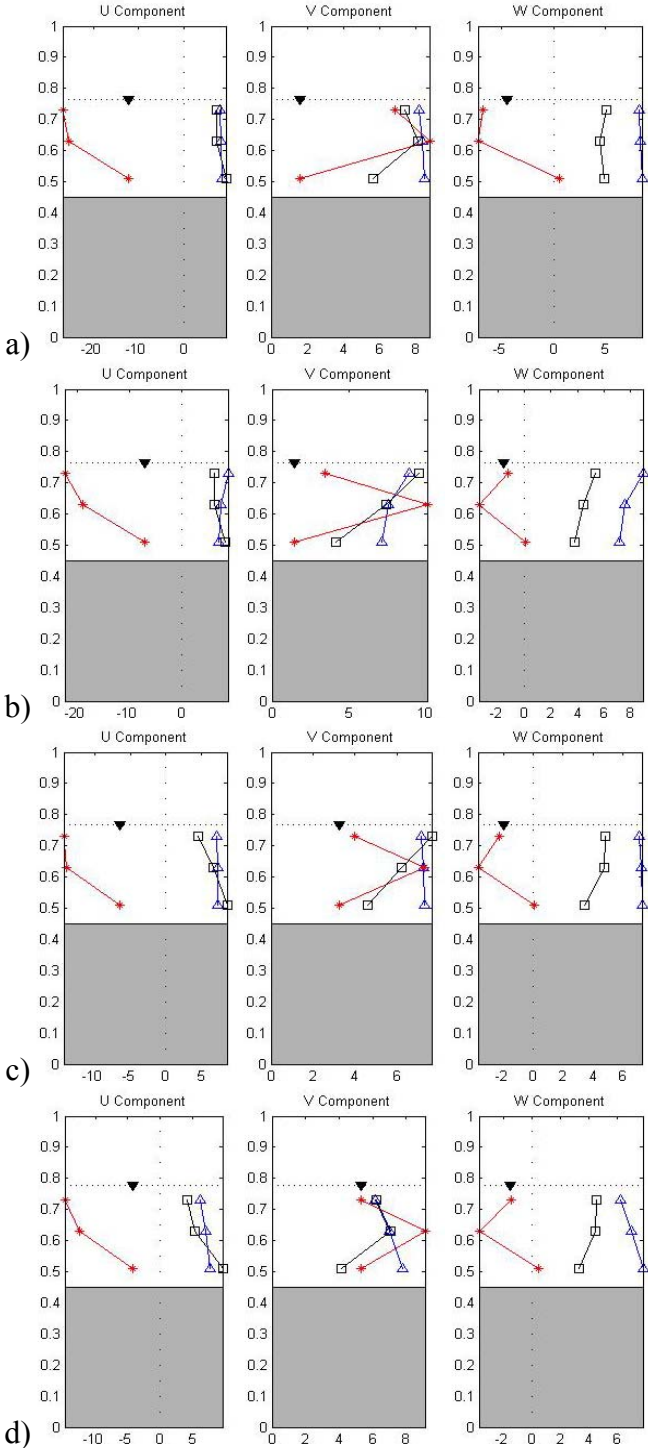
Figure 38:  Vertical Profiles at X=17m and Y=-9m over time at a)34.16s, b)34.70s, c)35.00s, and d)35.44s with the vertical axis being elevation (m) and horizontal axis being magnitude (cm/s): $(\ast)\overline{U}$ , $(\square)u'_{rms}$ , and $(\Delta)\sqrt{K}$ .
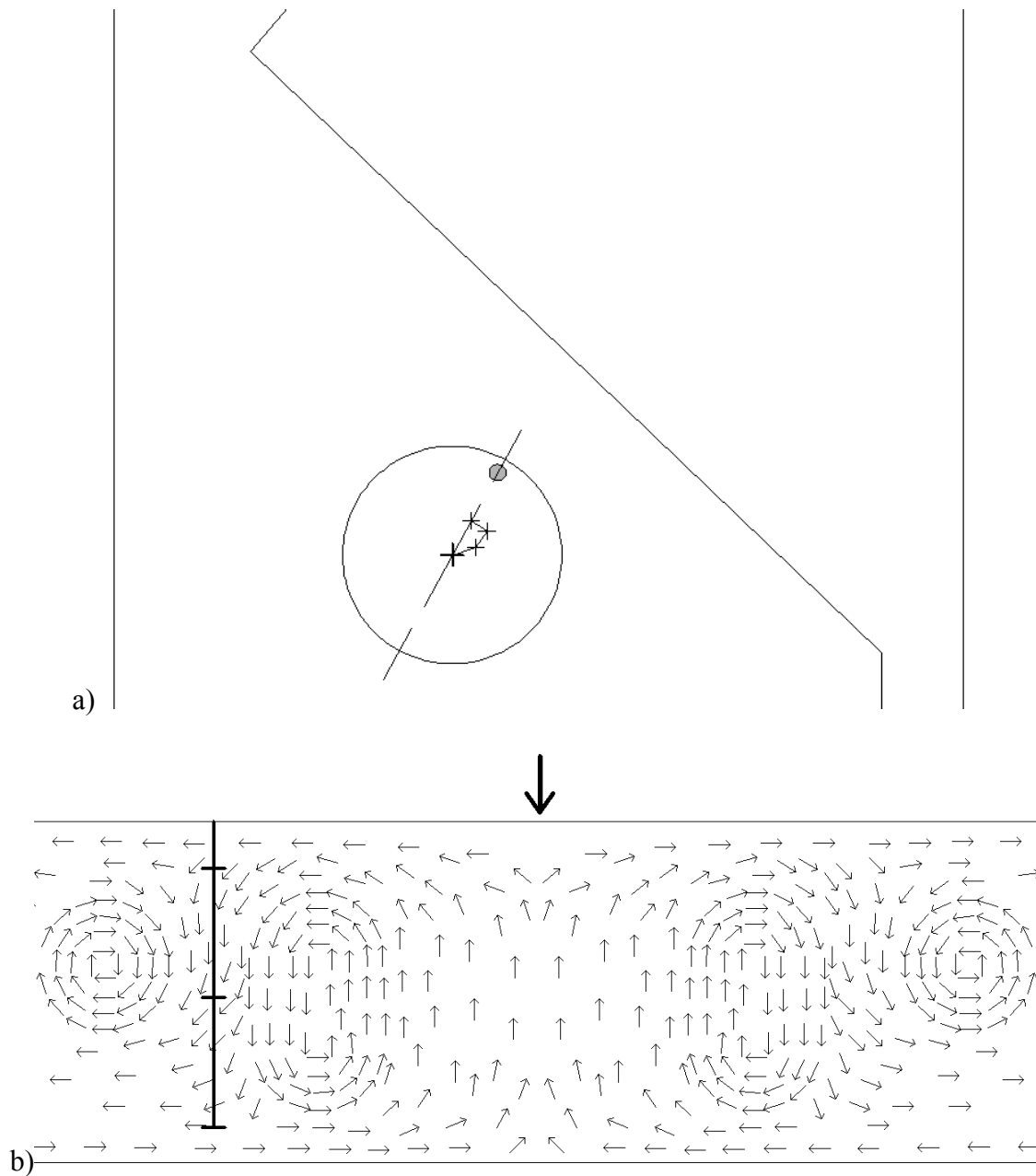
Figure 39: Eddy orientation near ADV stack at X=17 and Y=-9m from a) plan view and b) elevation view. Dashed line in planview represents vertical plane shown elevation view.

The data confirmed the formation of a three-dimensional coherent structure

(eddy) rotating counter clockwise near the ADVs located at X=17m, Y=-9m after

borefront (3) had propagated offshore.  The eddy was generated by the instability of the strong shear layer that developed along the shelf edge following borefront (3).  The offshore flow coupled with the abrupt change in the bathymetry created strong transverse shear which is the most significant generators of coherent turbulent structures (Socolofsky 2004).

The eddy identified in the experiment has characteristics that are common to three-dimensional coherent turbulent structures; the vertical flow is directed upward at the eddy's center and downward near the edges.  Also, there is an increase in turbulent kinetic energy associated with the eddy which was confirmed by the horizontal planes shown in Figure 30 through Figure 37 and vertical profiles in Figure 38.  The increased turbulent energy due to the eddy was further validate by the very low amount of turbulent energy detected elsewhere offshore of the shelf edge.  The data confirmed that the eddy extended from the water surface to the underlying bathymetry (at about $Z=0.49m$) agreeing with previous studies (Lin & Hwung 1992; Ting 2008).  Although the density/spacing of the instruments limited the complete documentation of the eddy, in general, the U velocity component was offshore, the V velocity component was toward the centerline of the basin, and the W velocity component was downward at $X=17m$, $Y=-9m$.  From this, we conclude that the ADVs were located shoreward and toward the centerline of the basin from the eddy's center of rotation.

# 10.0 MAXIMUM TURBULENT KINETIC ENERGY

To relate the structures and events that were observed offshore of the SWS, the

maximum turbulent kinetic energy was investigated.  Because the turbulent energy

within the water column is an extremely important mechanism for sediment transport, by

understanding it quantitatively, the importance of the structures and events became

clearer.  To do this, the maximum turbulent kinetic energy ( $K$ ) recorded by the ADVs

was extracted.  The maximum in the timeseries from each instrument was limited to the

point after the solitary wave, borefront (1), had passed causing the cross-shore

component of the mean velocity ( $\overline{U}$ ) to switch directions until 45 seconds after it was

generated.  The timeseries was limited to after borefront (1) had passed because of the

large amount of unreliable data that was eliminated during this time period in most of the

timeseries.  Similar to the method used to identify the eddy in Section 9.1, the same three

horizontal planes were used to display the maximum turbulent energy at each depth in

the water column.  To help convey the symmetry of the basin, the maximum turbulent

energy obtain with each ADV was mirrored about the centerline of the basin providing a

complete picture for the width of the basin.

Starting at the horizontal plane with the lowest elevation, Z=0.52m, Figure 40a

shows a large concentration of turbulent energy at the most onshore ADV locations.

These locations were at X=17m, Y=±9m and X=17m, Y=±12m which were near the

eddy.  At X=15m, Y=±9m some turbulent energy was measured when the eddy wavered

to it most offshore location.  As explained above, the ADVs at this elevation and Z=0.63m were limited to those offshore of the shelf edge due to the shallow water bathymetry.

Moving the horizontal plane up in elevation to Z=0.63m, Figure 40b shows that all of the turbulent energy was concentrated around X=17m, Y=±9m due to the eddy, while the other surrounding ADV locations did not experience much turbulence.  The magnitude of the maximum turbulent energy measured at this elevation was very well correlated to the maximum shown in Figure 40a at Z=0.52.

The next elevation, Z=0.74m, was closest to the water surface and included the ADVs located on top of the shallow water bathymetry.  Figure 40c revealed a much broader area of turbulence as compared to the two previous elevations.  The maximum turbulent energy onshore of the shelf edge was due to borefront (4) that propagated onshore over the shallow water shelf against the offshore flow following borefront (3) causing a rapid change in the mean velocity in a short period of time as discussed in Section 6.3.  The only exception to this was at X=15.0m, Y=0m where the wakes following borefront (3) collided and broke.  Looking at the ADVs located offshore of the shelf edge, the maximum turbulent energy was again found at X=17m, Y=±9m as expected due the presence of the eddy.  Comparing the offshore turbulence found in all three horizontal planes, the magnitudes were very consistent in the region where the eddy developed.  The maximum turbulent kinetic energy in all three horizontal planes confirmed that large scale coherent structures and borefronts contained the greatest turbulent energy.

Wave Basin: Max K(turbulent kinetic energy,m²/s²) @Z~0.52/during rundown

a)

b)

c)
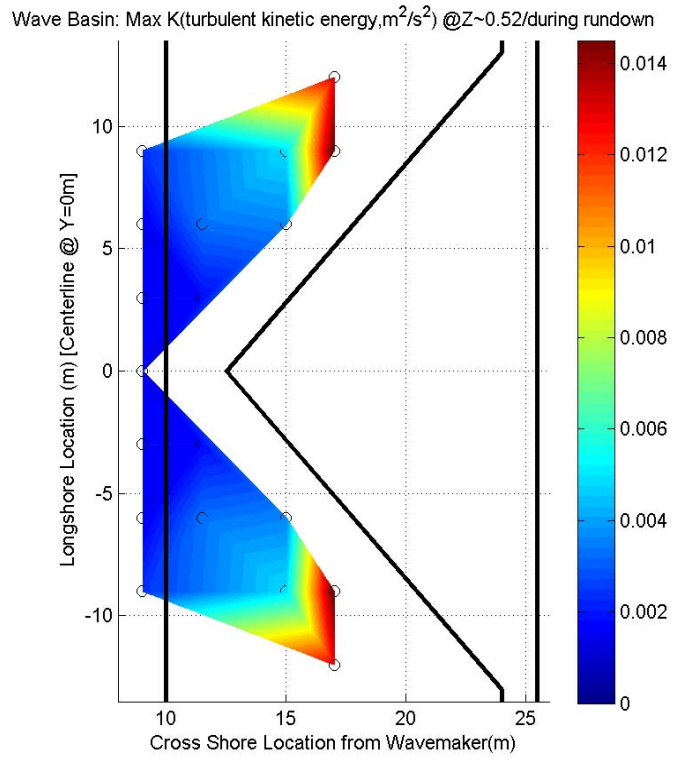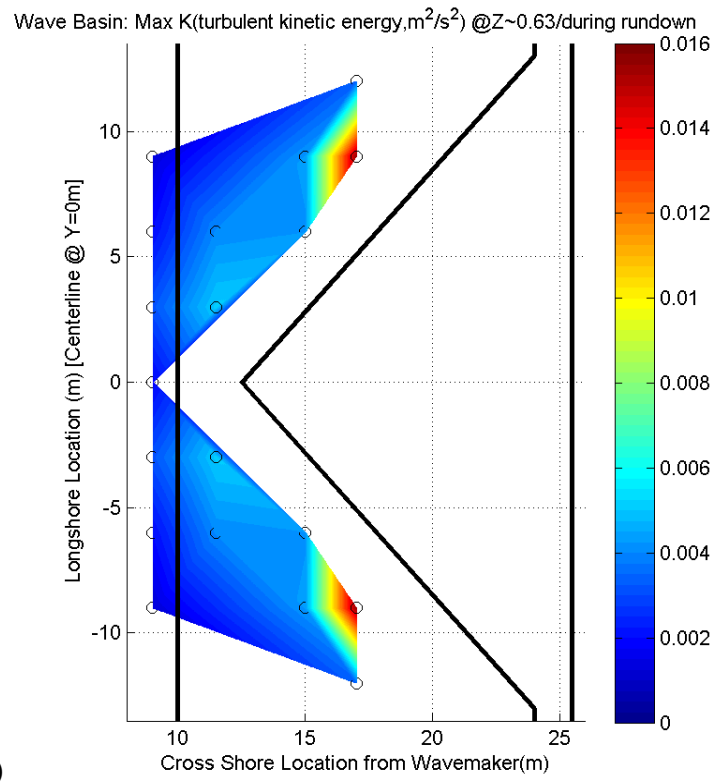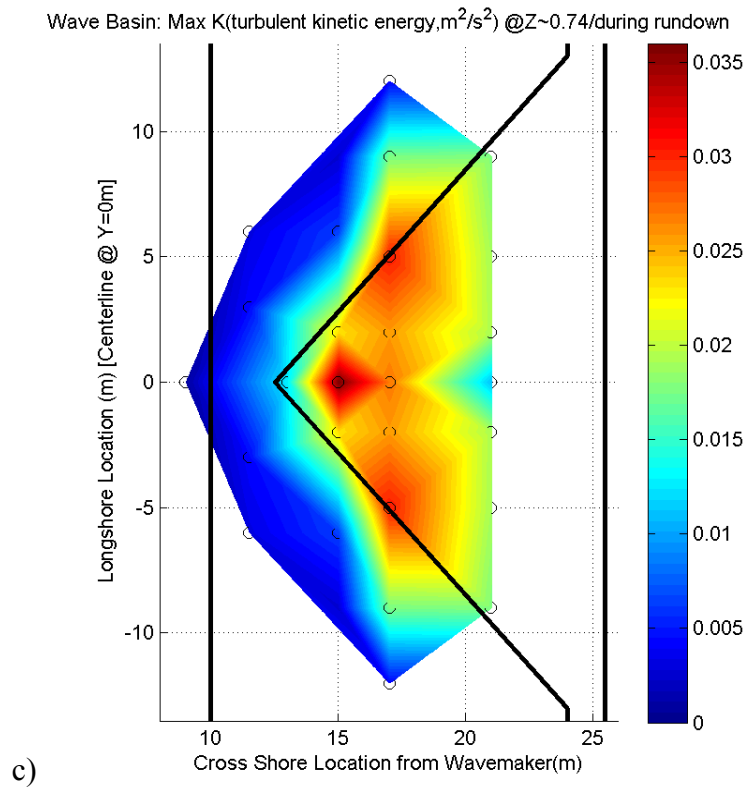
Figure 40:  Maximum turbulent energy ( $K$ ) recorded a) at Z=0.52m, b) at Z=0.63m, and c) at Z=0.74m.

# 11.0 CONCULSIONS

The laboratory study, presented above, investigated the highly complex interactions between a breaking solitary wave and a shallow water shelf. The generated wave provided the initial energy and the shelf, coupled with the resulting mean flows, produced the various phenomena that were observed. Due to the shallow shelf, the solitary wave broke as a strongly plunging breaker resulting in multiple other borefronts. They included a secondary borefront following the generated borefront, a reflected borefront from the top of the planar beach, and a return wave after the reflected borefront traveled offshore.

The free surface measurements allowed the evolution of the solitary wave to be revealed both offshore and onshore of the SWS. Specifically, the wave shape and height was very constant within the constant depth portion of the basin and remained symmetric about the centerline as it propagated over the bathymetry. As it encountered the shelf, almost no shoaling was observed at the apex due the very steep slopes while noticeable shoaling was revealed near the basin side walls. The shoaling was greatest in these regions due to the confinement and focusing of the wave's energy by the wall coupled with the milder sloping bathymetry. Once the wave traveled over the shelf edge, the wave height rapidly decayed due to breaking.

Another known phenomenon that was observed in the experiment was refraction. Refraction was caused by two-dimensional bathymetry and manifested itself by forcing

the wave crest to bend in a manner to become oriented parallel to the depth contours. Due to the speed the generated wave impacted the shelf and the short distance between the constant depth portion of the basin and the shelf edge, the wave experienced only a mild amount of refraction that was revealed in the runup beyond the SWS. The borefronts that followed were more parabolic in shape as they experienced a greater amount of refraction due to their slower propagation speeds. The small amount of refraction that the solitary wave experienced was captured by the dye streamlines which revealed the direction of the flow following the wave. The streamlines showed the longshore component of the flow by bending in toward the centerline of the basin.

Once the solitary wave reached the SWS, the runup up on the planar beach was not uniform in the longshore direction as expected due to the bathymetry offshore. Closest to the SWS, the runup arrived first near the basin side wall, but as it traveled further up the beach, the runup arrived first near the centerline. The change in the shape revealed that the cross-shore velocity was not constant and the greatest velocity magnitude occurred near the centerline due to the focusing of water as the wave front refracted over the shelf. After the initial focusing was relaxed, a jetting mechanism was observed as the converged mass of water spread both laterally and in the direction of propagation due to gravity.

Along with the borefront from the solitary wave, a total of three others were tracked both through the free surface data and the fluid velocity data. The change in water surface was correlated to specific turbulent events extracted from the velocity timeseries. The large turbulent events that were experienced were directly linked to the

passing borefronts. Interestingly, other instances where there was a change in the fluid velocity with time (acceleration) a measureable turbulent event accompanied. This showed that the shear within the water column was a major factor in causing turbulence even if the water depth was very shallow. In general, on top of the shelf, the greatest turbulent kinetic energy experienced was associated with borefront (4) because of the rapid change in existing flow that was present following borefront (3). The change in velocity with time coupled with the change in direction caused the turbulence to be relatively large.

Moving offshore of the shelf edge, a three dimensional coherent structures was found to develop after the borefront (3) propagated offshore. The eddy resulted from the instability in the shear layer that was revealed by a hydraulic bore along the shelf edge where there was an abrupt change in the bathymetry. The eddy was identified both visually by the local concentration of dye and quantitatively by the vertical stack of ADVs near its center of rotation. The ADV stack allowed the three-dimensional flow field to be recorded and gave insight to the eddy's vertical flow field and turbulent energy with depth. Despite the visual observations and the velocity data, the flow field could not be completely documented due to the movement and orientation of the eddy with respect to the single location where vertical profiles were obtained. Although it was difficult to say for certain, we believe that the multiple vortex rings that were identified by Lin et al. (2003) were also present in the eddy. A hypothetical scenario of the organization of the vortex rings was provided, but there was not enough data to provide a clear, accurate flow field within the eddy. We propose that the rings had

different diameters and angular rotations which contributed the inner flows and helped drive an upward flow at the eddy's center.  The turbulent energy associated with these large structures was also confirmed by the data with most of the turbulent energy recorded offshore of the shelf being within the eddy.  Both the vertical profiles over time and the horizontal planes of turbulent energy were constant with depth revealing the stability of the structure.

The conclusions from the experiment, along with the presented data, provide a great starting point to validate and calibrate numerical models that are being used to predict nearshore circulations.  Given that turbulence is the dominant mechanism responsible for sediment transport, the experiment gives reliable turbulent quantities with respect to borefronts in shallow water and large scale structures as they move into deeper water.  We hope that in the future the information presented will be useful in advancing the prediction and quantification of sediment transport and ultimately predicting coastal morphology.

# 12.0 REFERENCES

Cea, L., Puertas, J., and Pena, L., 2007. Velocity measurements on highly turbulent free surface flow using ADV. Experiments in Fluids 42, 333-348.

Dalrymple, R.A., 1992. Prediction of storm/normal beach profiles. Journal of Waterway, Port, Coastal, and Ocean Engineering 118, 193-200.

Dean, R.G., and Dalrymple, R.A., 1991. Water wave mechanics for engineers and scientists. World Scientific Publishing Co., 353 pp.

Deigaard, R., Fredsoe, J., and Hedegaard, I.B., 1986. Suspended sediment in the surf zone. Journal of Waterway, Port, Coastal, and Ocean Engineering 112, 115-129.

Geyer, W.R., 1993. Three-dimensional tidal flow around headlands. Journal of Geophysical Research 98, 955-966.

Grilli, S.T., Subramanya, R., Svendsen, I.A., and Veeramony, J., 1994. Shoaling of solitary waves on plane beaches. Journal of Waterway, Port, Coastal, and Ocean Engineering 120, 609-628.

Hibberd, S. and Peregrine, D.H., 1979.  Surf and runup on a beach: a uniform bore.  Journal of Fluid Mechanics 95, 323-345.

Hsiao, S.C., Hsu, T.W., Lin, T.C., and Chang, Y.H., 2008.  On the evolution and run-up of breaking solitary waves on a mild sloping beach.  Coastal Engineering 55, 975-988.

Johns, B. and Jefferson, R.J., 1980.  The numerical modeling of surface wave propagation in the surf zone.  Journal of Physical Oceanography 10, 1061-1069.

Johns, B., 1978.  The modeling of tidal flow in a channel using a turbulence energy closure scheme.  Journal of Physical Oceanography 8, 1042-1049.

Lin, C. and Hwung, H.H., 1992.  External and internal flow fields of plunging breakers.  Experiments in Fluids 12, 229-237.

Lin, J.C., Ozgoren, M., and Rockwell, D., 2003.  Space-time development of the onset of a shallow-water vortex.  Journal of Fluid Mechanics 485, 33-66.

Lin, P. and Liu, P.L.F., 1998.  A numerical study of breaking waves in the surf zone.  Journal of Fluid Mechanics 359, 239-264.

Lubin, P., Vincent, S., Abadie, S., and Caltagirone, J.P., 2006.  Three-dimensional large eddy simulation of air entrainment under plunging breaking waves.  Coastal Engineering 53, 631-655.

Nadoaka, K., Hino, M., Koyano, Y., 1989.  Structure of turbulent flow field under breaking waves in the surf zone.  Journal of Fluid Mechanics 204, 359-387.

Negretti, M.E. and Socolofsky, S.A., 2005.  Stabilization of cylinder wakes in shallow water flows by means of roughness elements: an experimental study.  Experiments in Fluids 38, 403-414.

Mathieu, J., and Scott, J., 2000.  An Introduction to Turbulent Flow.  Cambridge University Press, 374 pp.

Tennekes, H. and Lumley, J.L., 1972.  A First Course in Turbulence. MIT Press, 300 pp.

Ting, F.C.K. and Kirby, J.T., 1994.  Observation of undertow and turbulence in a laboratory surf zone.  Coastal Engineering 24, 51-80.

Ting, F.C.K. and Kirby, J.T., 1995.  Dynamics of surf-zone turbulence in a strong plunging breaker.  Coastal Engineering 24, 177-204.

Ting, F.C.K., 2006.  Large-scale turbulence under a solitary wave.  Coastal Engineering 53, 441-462.

Ting, F.C.K., 2008.  Large-scale turbulence under a solitary wave: Part 2 forms and evolution of coherent structures.  Coastal Engineering 55, 522-536.

Titov, V.V. and Synolakis, C.E., 1995.  Modeling of breaking and nonbreaking long-wave evolution and runup using VTCS-2.  Journal of Waterway, Port, Coastal, and Ocean Engineering 121, 308-316.

Schaffer, H.A., Madsen, P.A., and Deigaard, R., 1993.  A Boussinesq model for waves breaking in shallow water.  Coastal Engineering 20, 185-202.

Signell, R.P. and Geyer, W.R., 1991.  Transient eddy formation around headlands. Journal of Geophysical Research 96, 2561-2575.

Socolofsky, S.A. and Jirka, G.H., 2004.  Large-scale flow structures and stability in shallow flows.  Journal of Environmental Engineering Science 3,451-462.

Stoker, J.J., 1957.  Water waves.  Interscience Publisher, New York, New York.

Zhao, Q., Armfield, S., and Tanimoto, K., 2004.  Numerical simulation of breaking

waves by multi-scale turbulence model.  Coastal Engineering 51, 53-80.

# APPENDIX I:  COMPLETE WG PRESENTATION

The WG timeseries presented below are organized moving in the positive longshore direction and in the positive cross-shore direction starting at X=5m, Y=-12m and ending at X=25m, Y=12m.
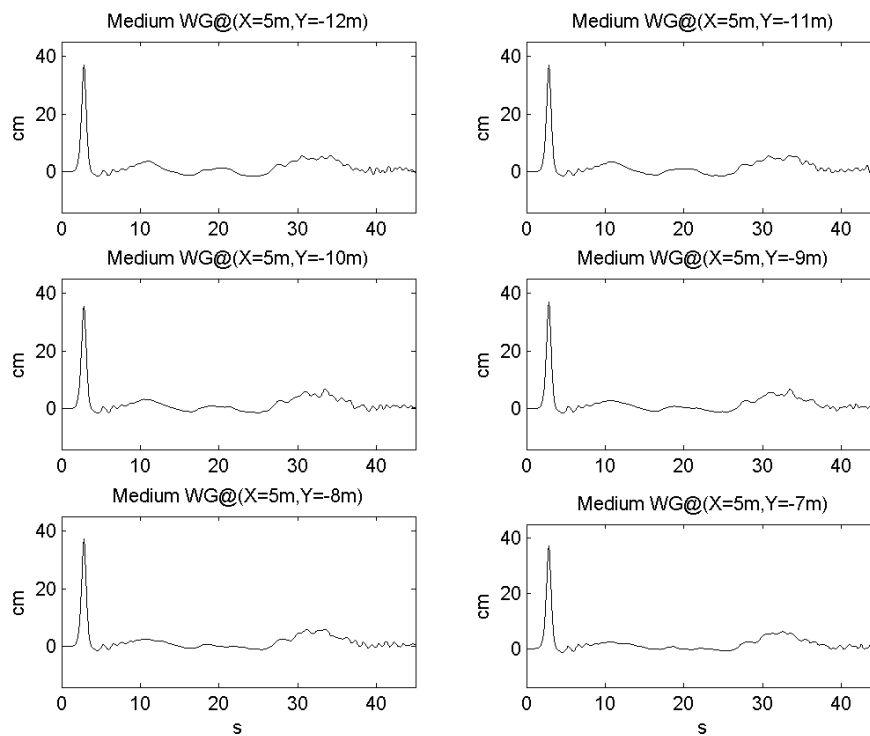


Figure 41: WG timeseries including X=5m, Y=12m to X=5m, Y=-7m.
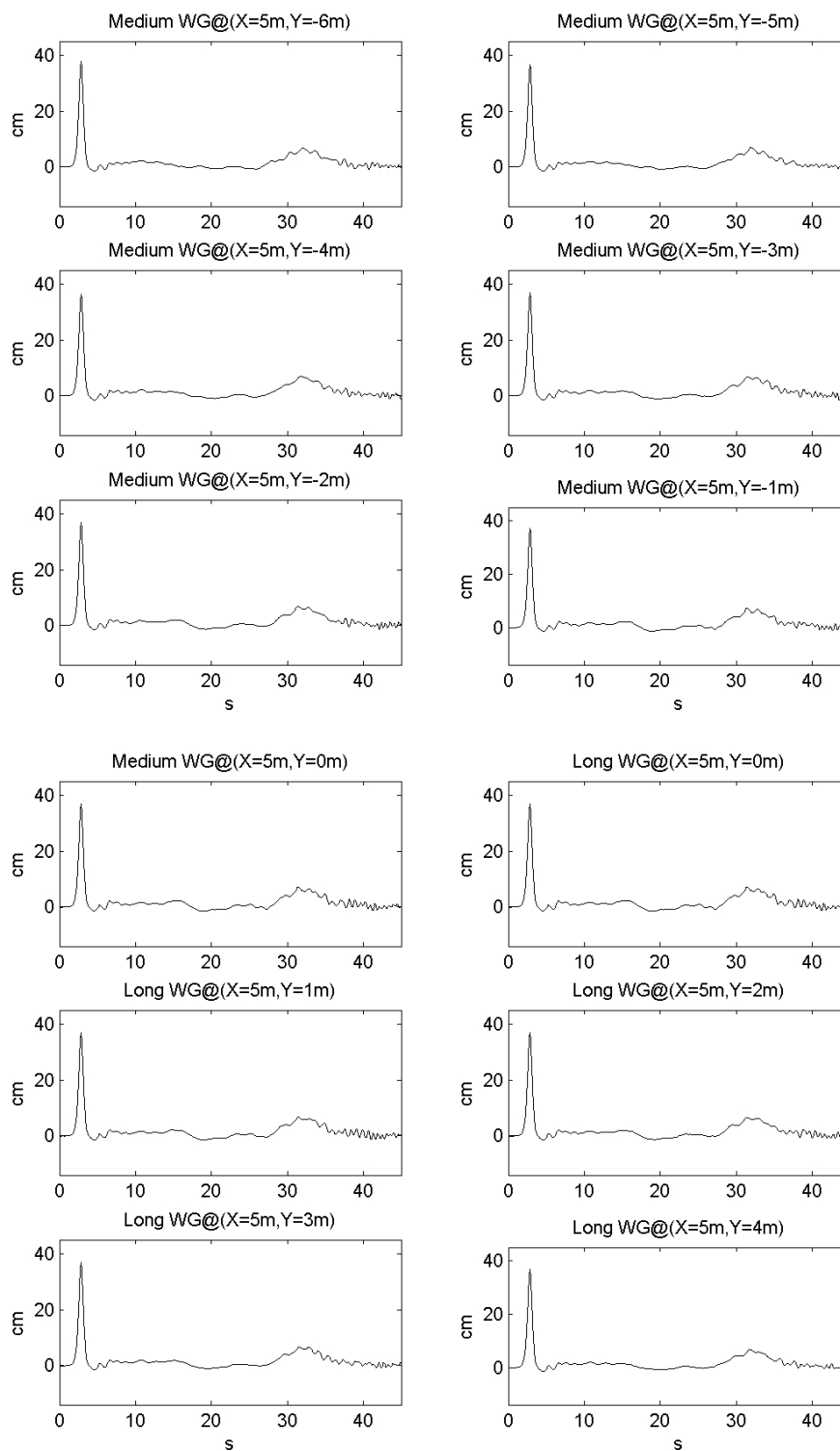
Figure 42: WG timeseries including X=5m, Y=-6m to X=5m, Y=4m.
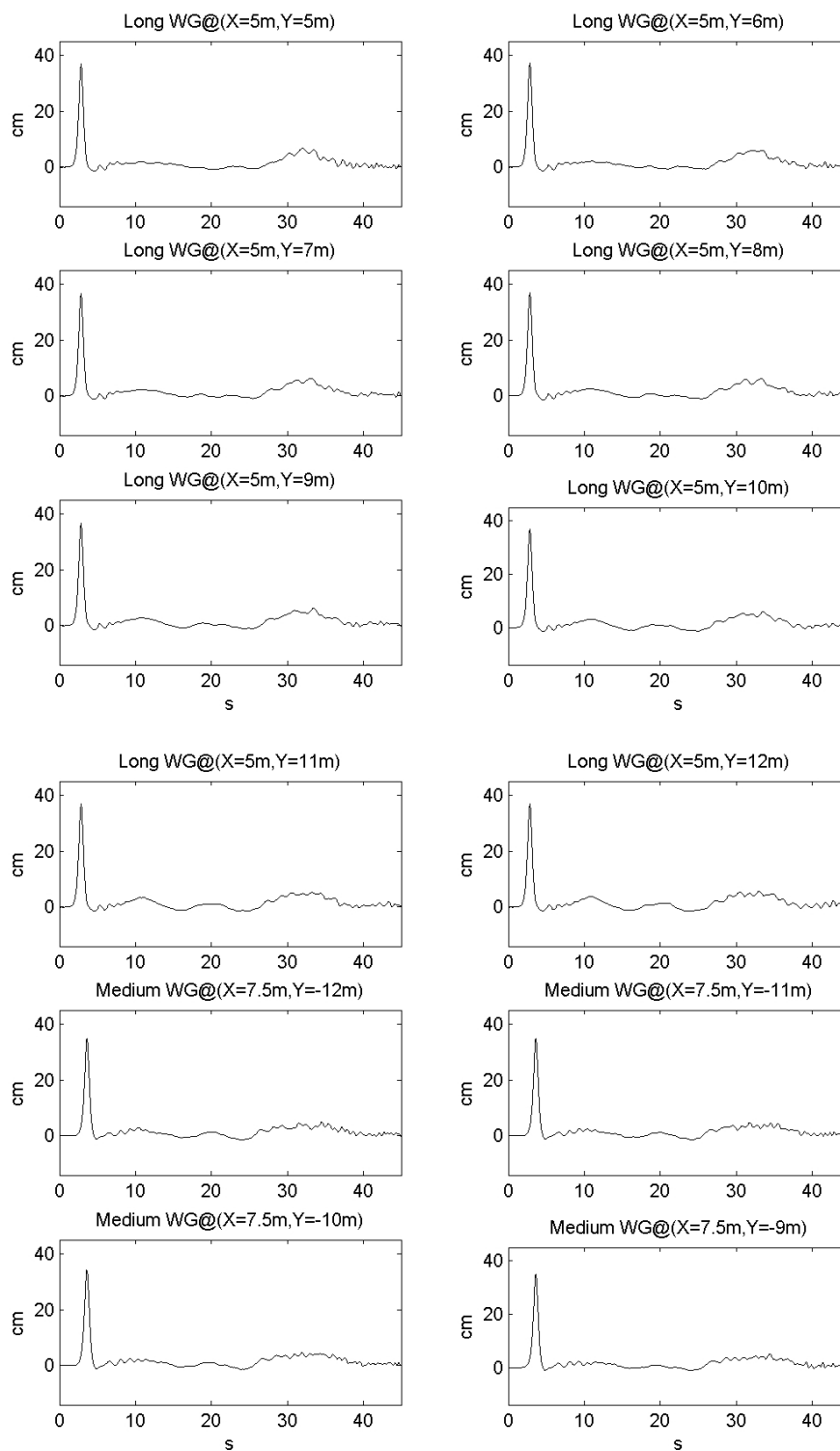
Figure 43: WG timeseries including X=5m, Y=5m to X=7.5m, Y=-9m.
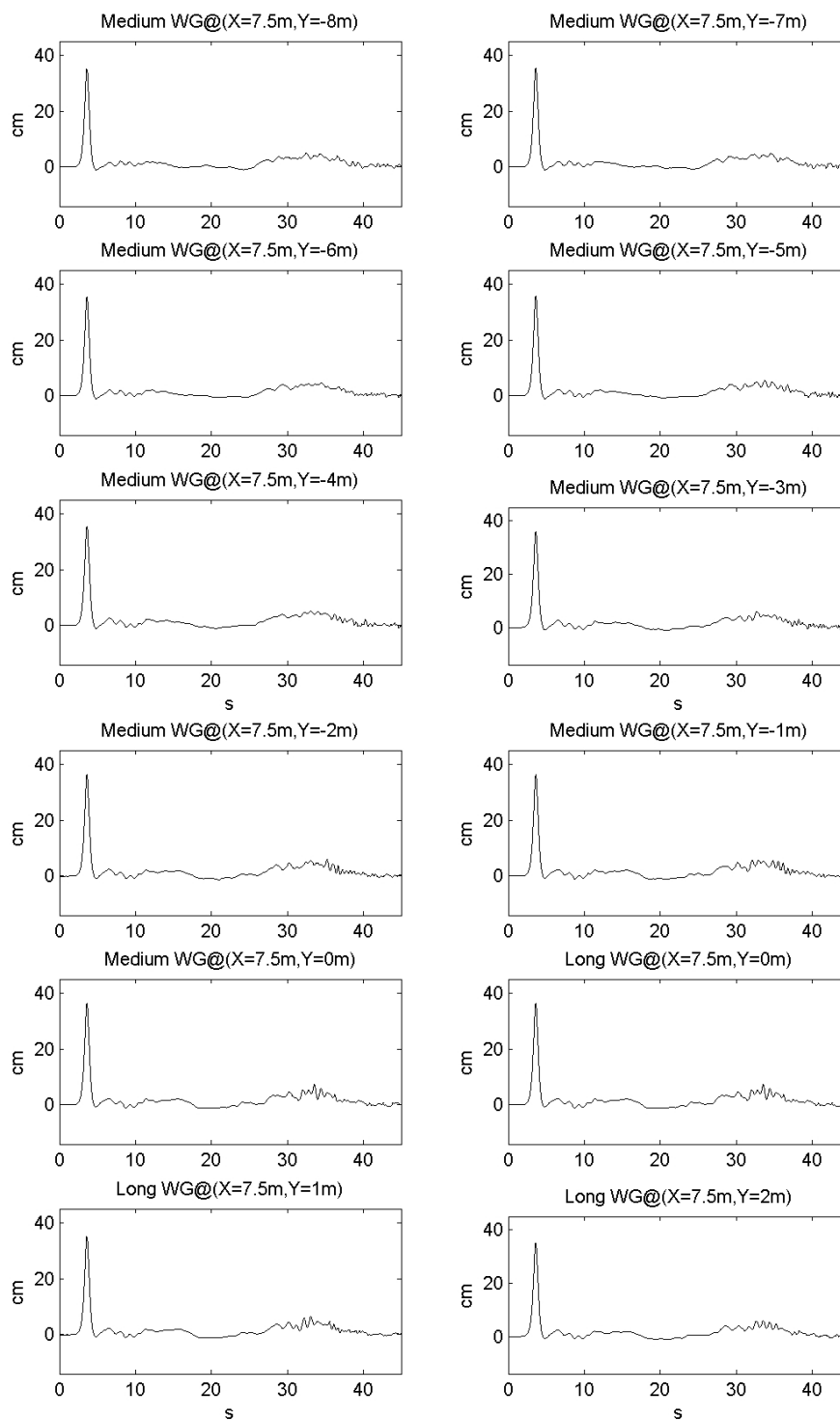
Figure 44: WG timeseries including X=7.5m, Y=-8m to X=7.5m, Y=2m.
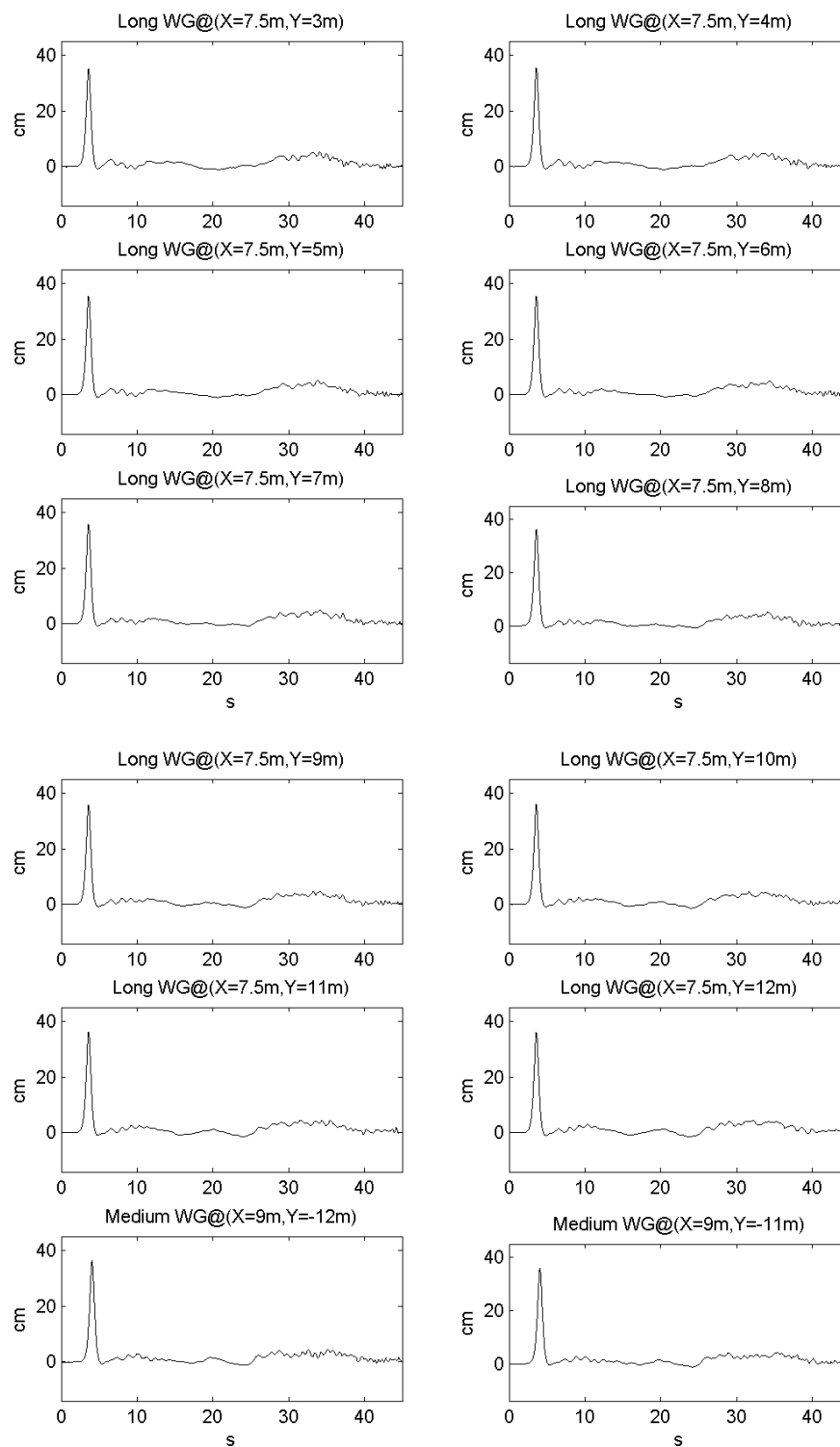
Figure 45: WG timeseries including X=7.5m, Y=3m to X=9m, Y=-11m.
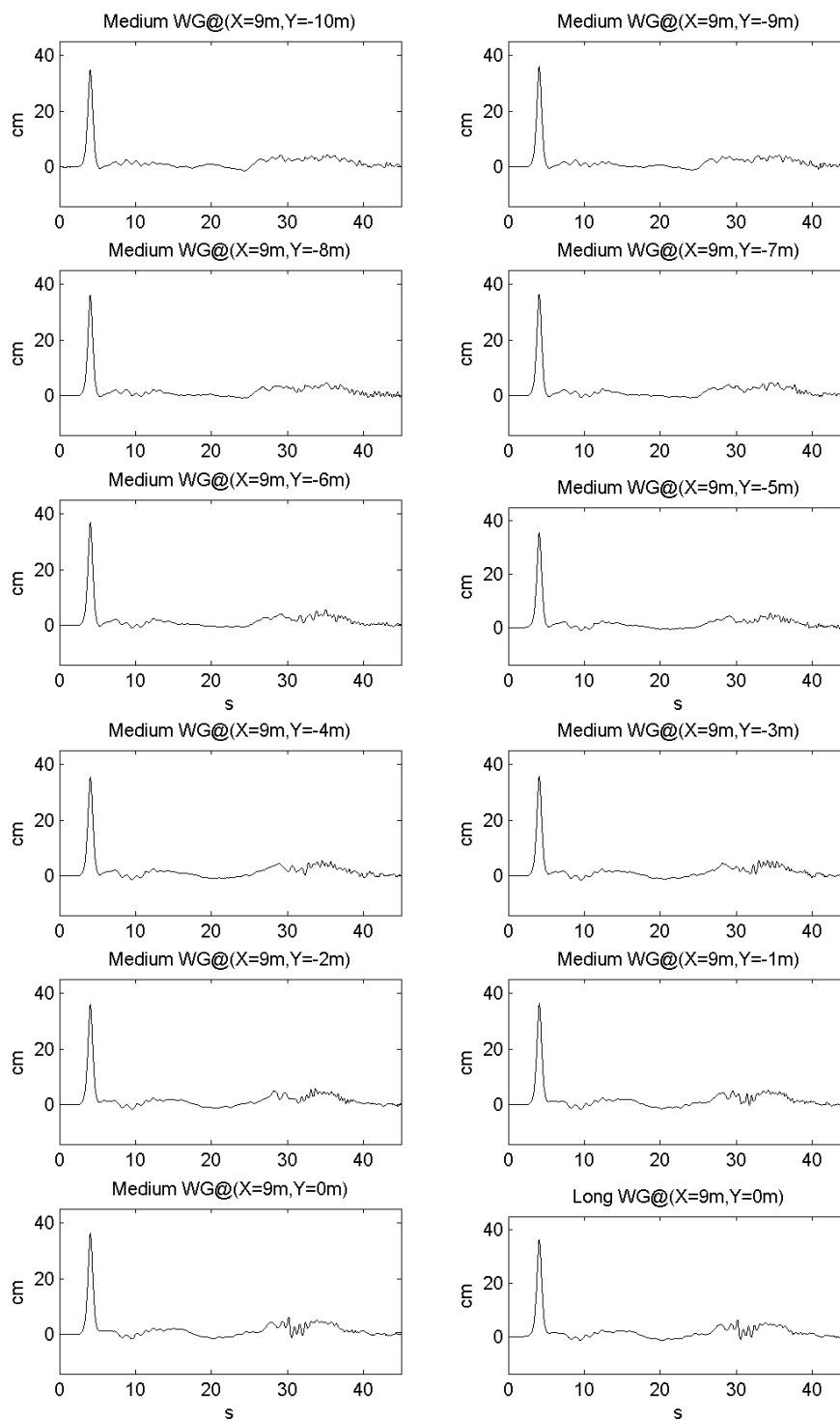
Figure 46: WG timeseries including X=9m, Y=-10m to X=9m, Y=0m.
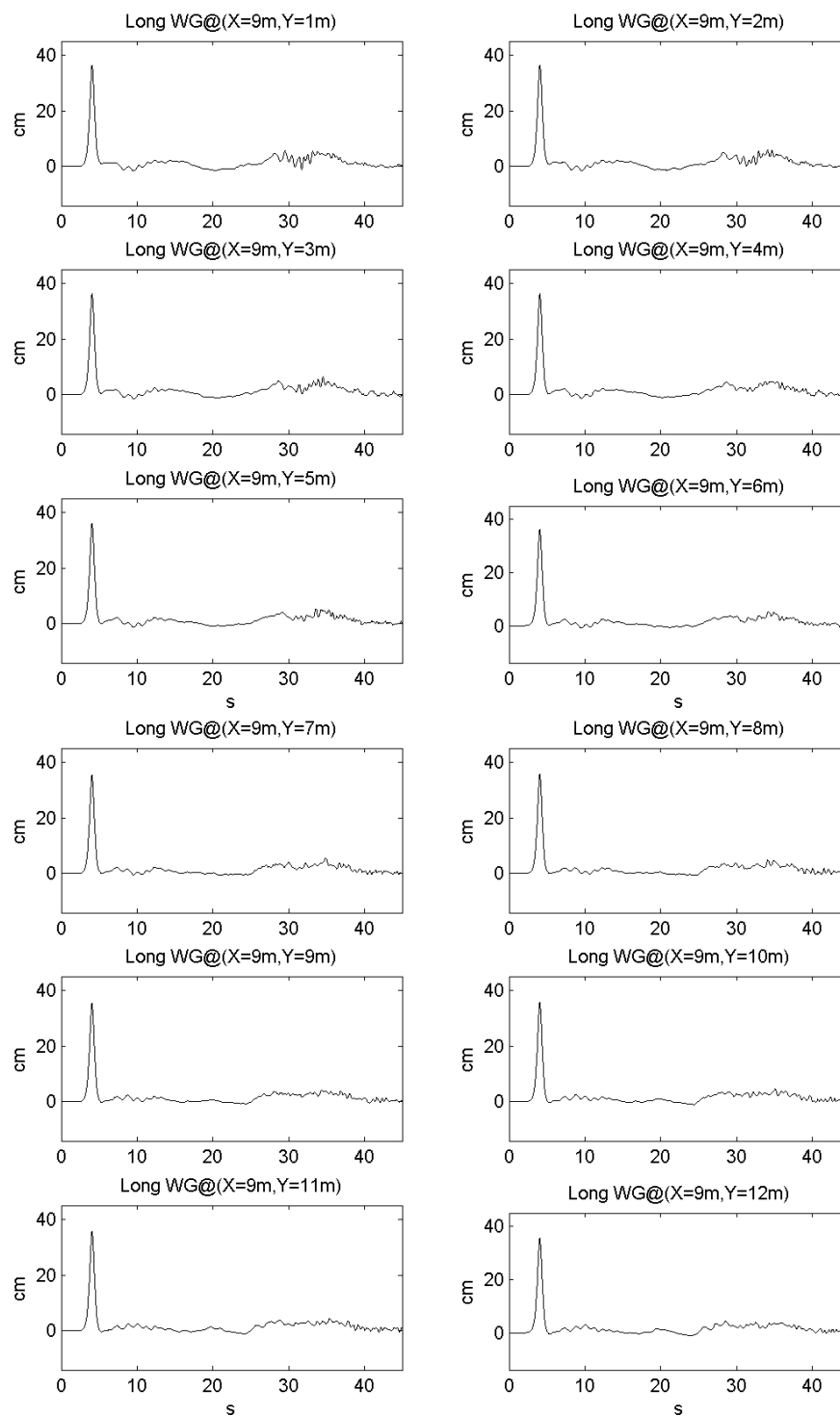
Figure 47: WG timeseries including X=9m, Y=1m to X=9m, Y=12m.
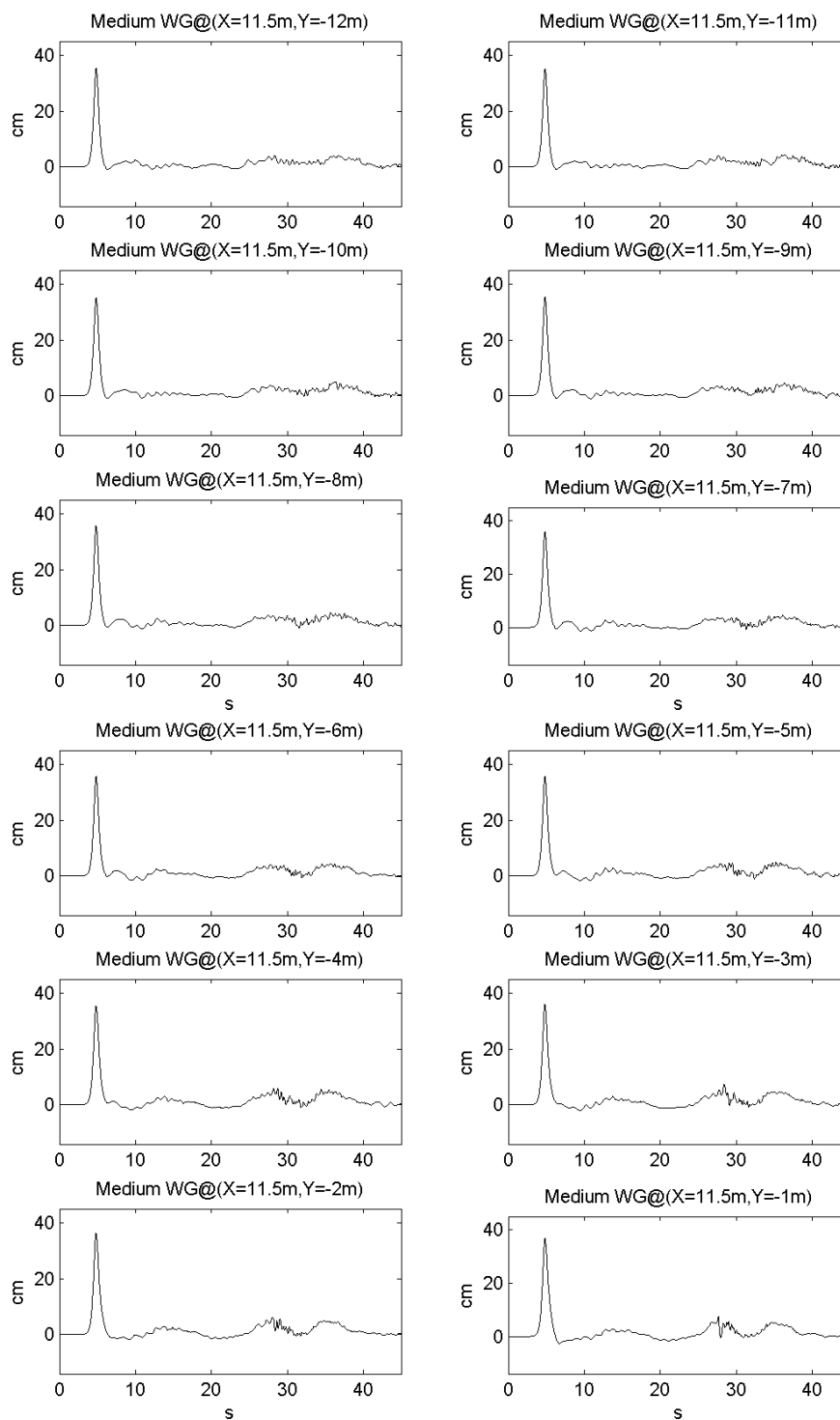
Figure 48: WG timeseries including X=11.5m, Y=-12m to X=11.5m, Y=-1m.
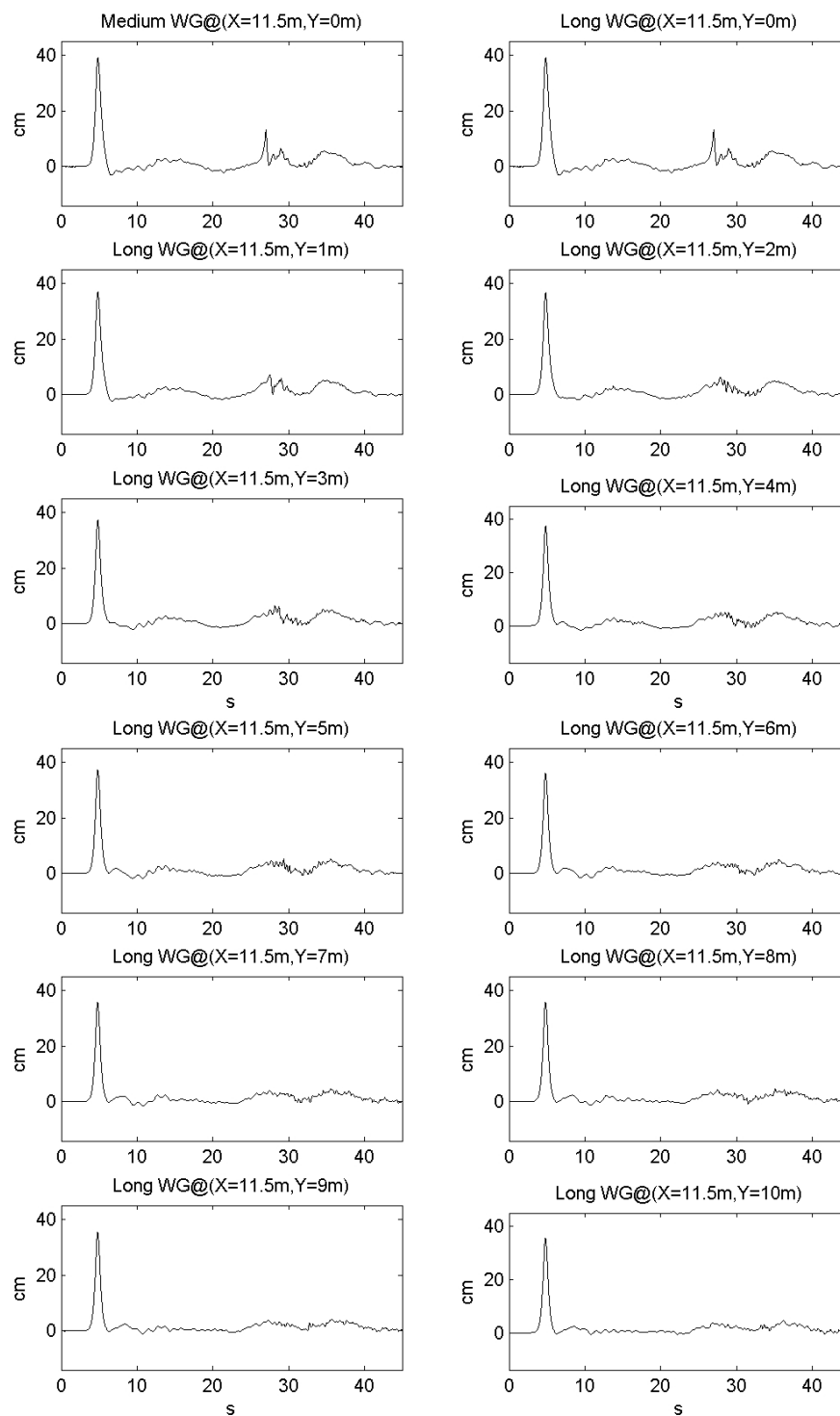
Figure 49: WG timeseries including X=11.5m, Y=0m to X=11.5m, Y=10m.
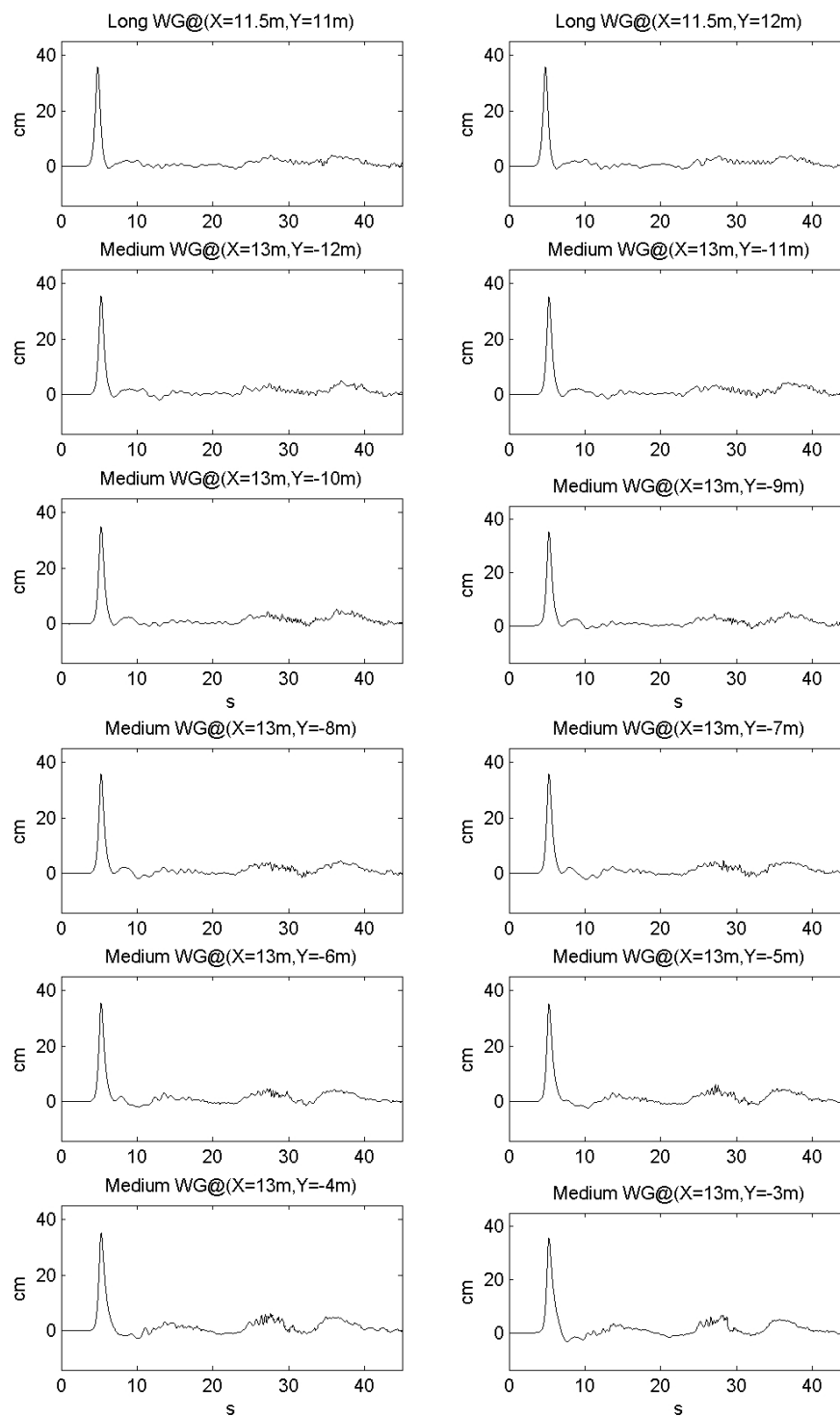
Figure 50: WG timeseries including X=11.5m, Y=11m to X=13m, Y=-3m.
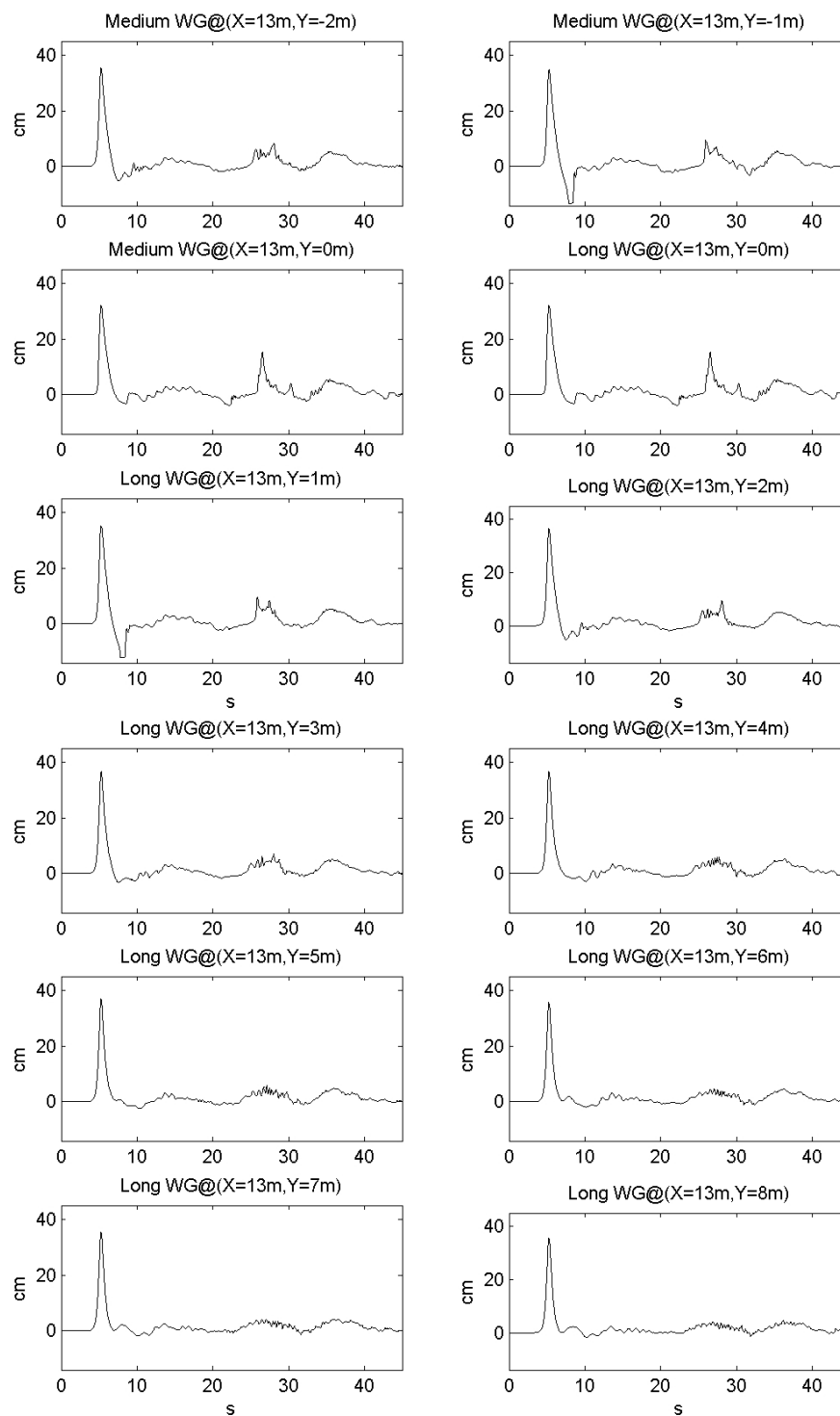
Figure 51: WG timeseries including X=13m, Y=-2m to X=13m, Y=8m.
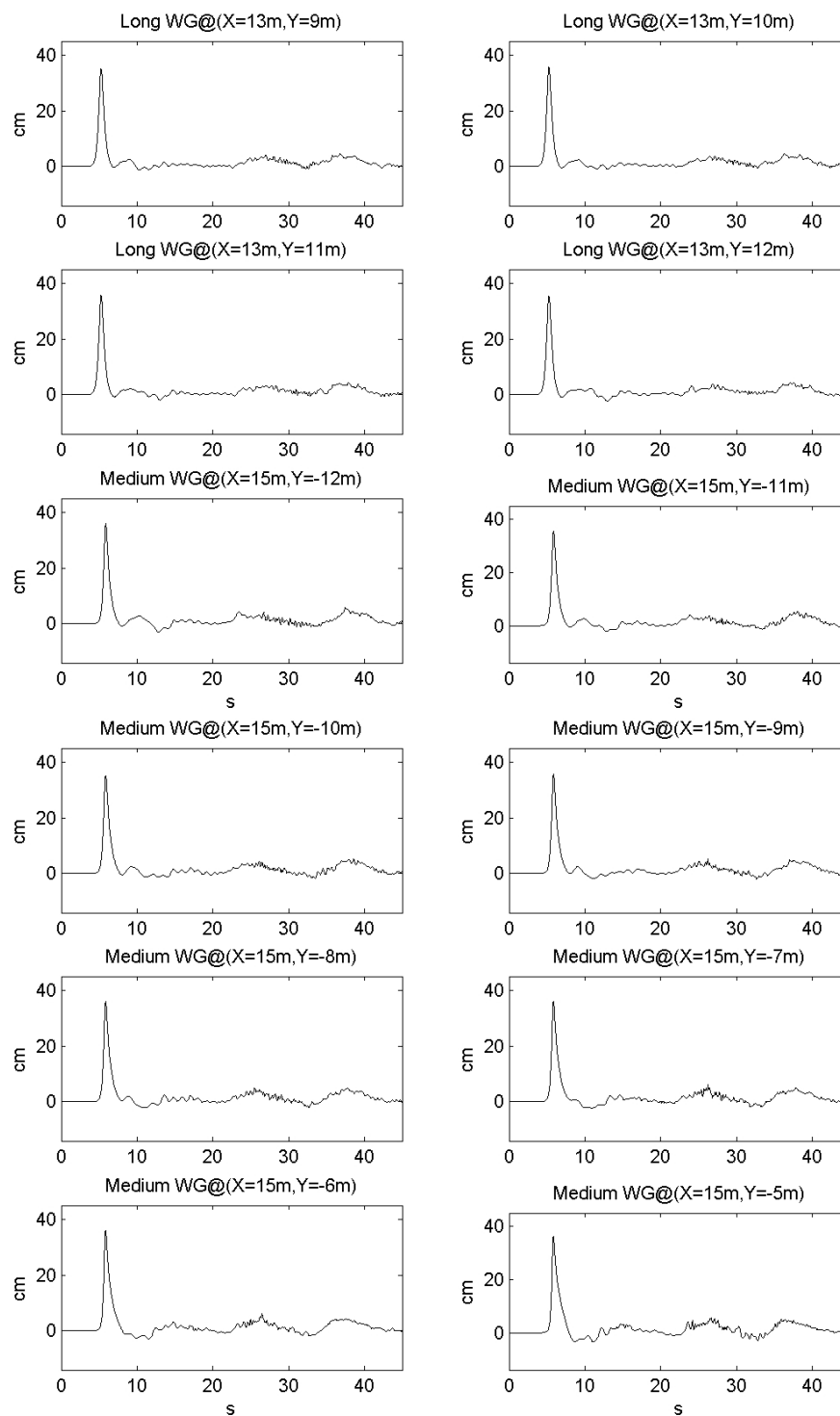
Figure 52: WG timeseries including X=13m, Y=9m to X=15m, Y=-5m.
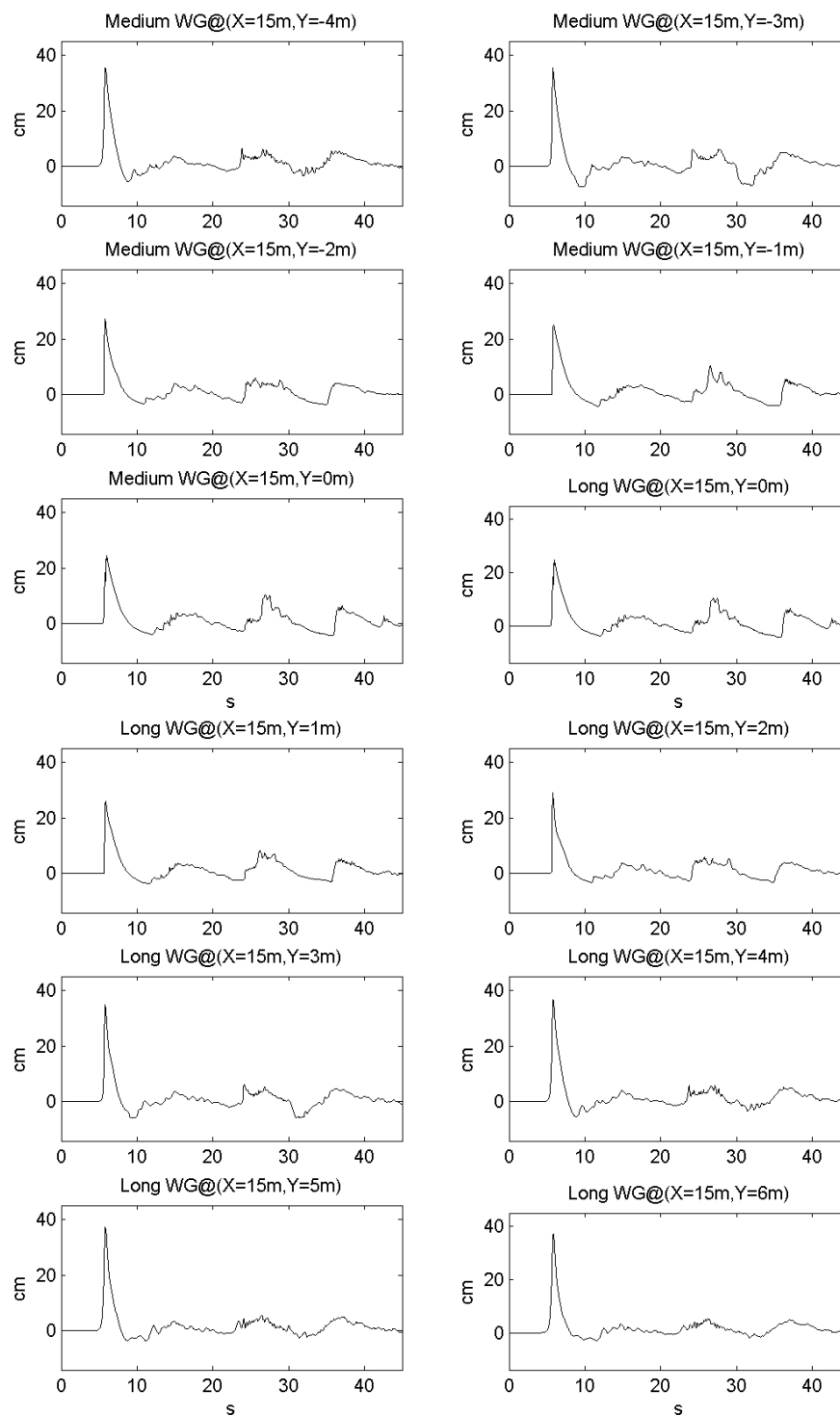
Figure 53: WG timeseries including X=15m, Y=-4m to X=15m, Y=6m.
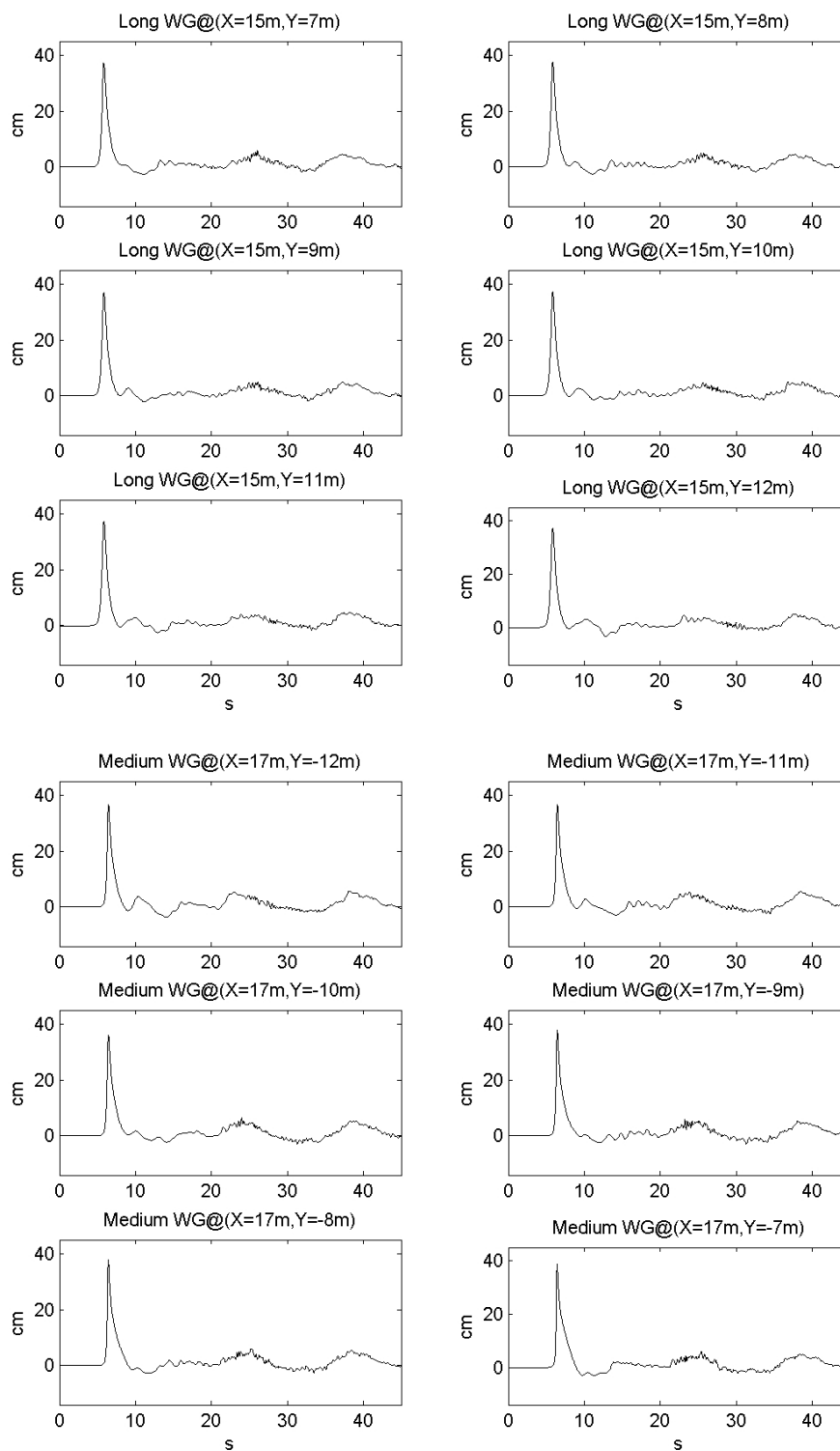
Figure 54: WG timeseries including X=15m, Y=7m to X=17m, Y=-7m.
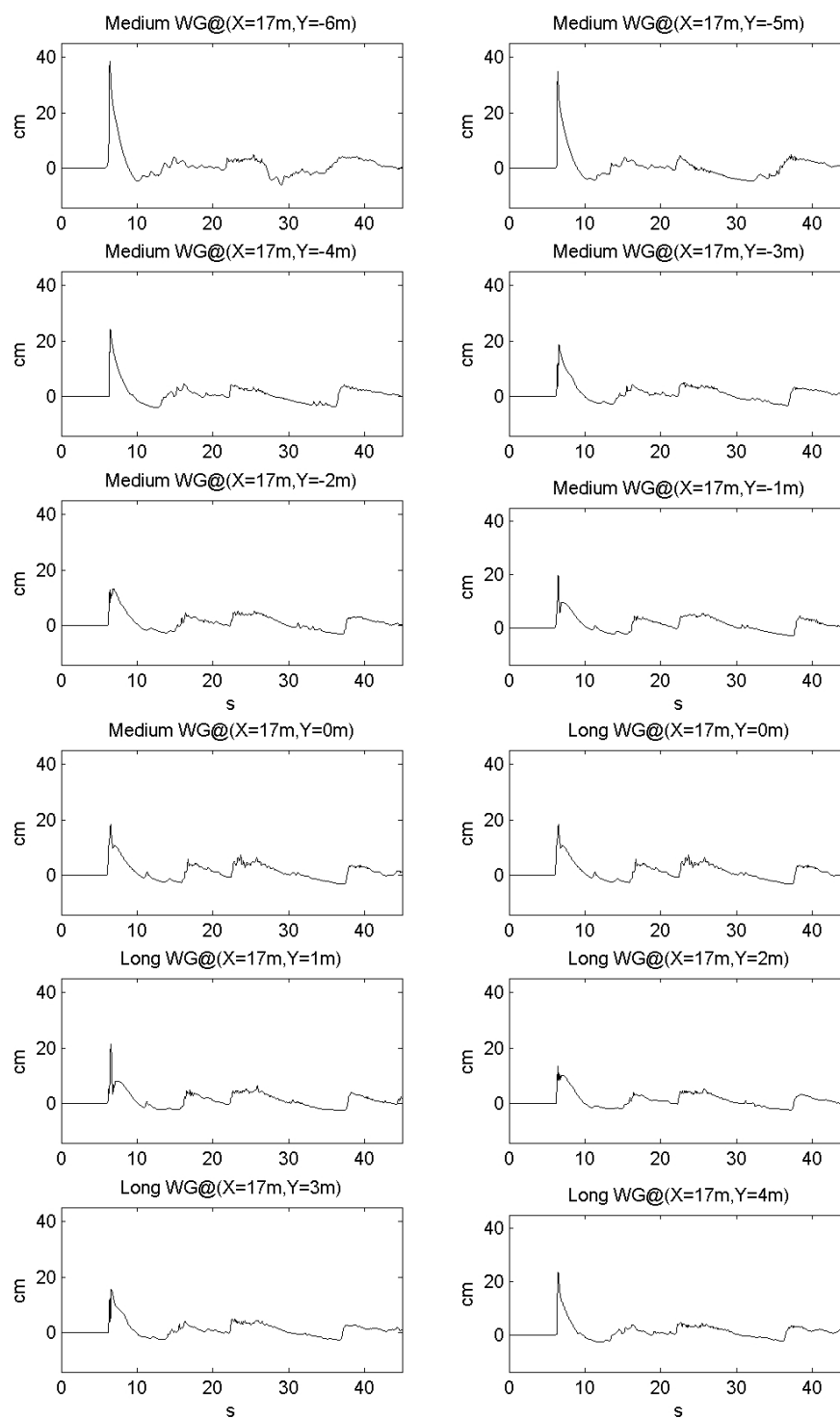
Figure 55: WG timeseries including X=17m, Y=-6m to X=17m, Y=4m.
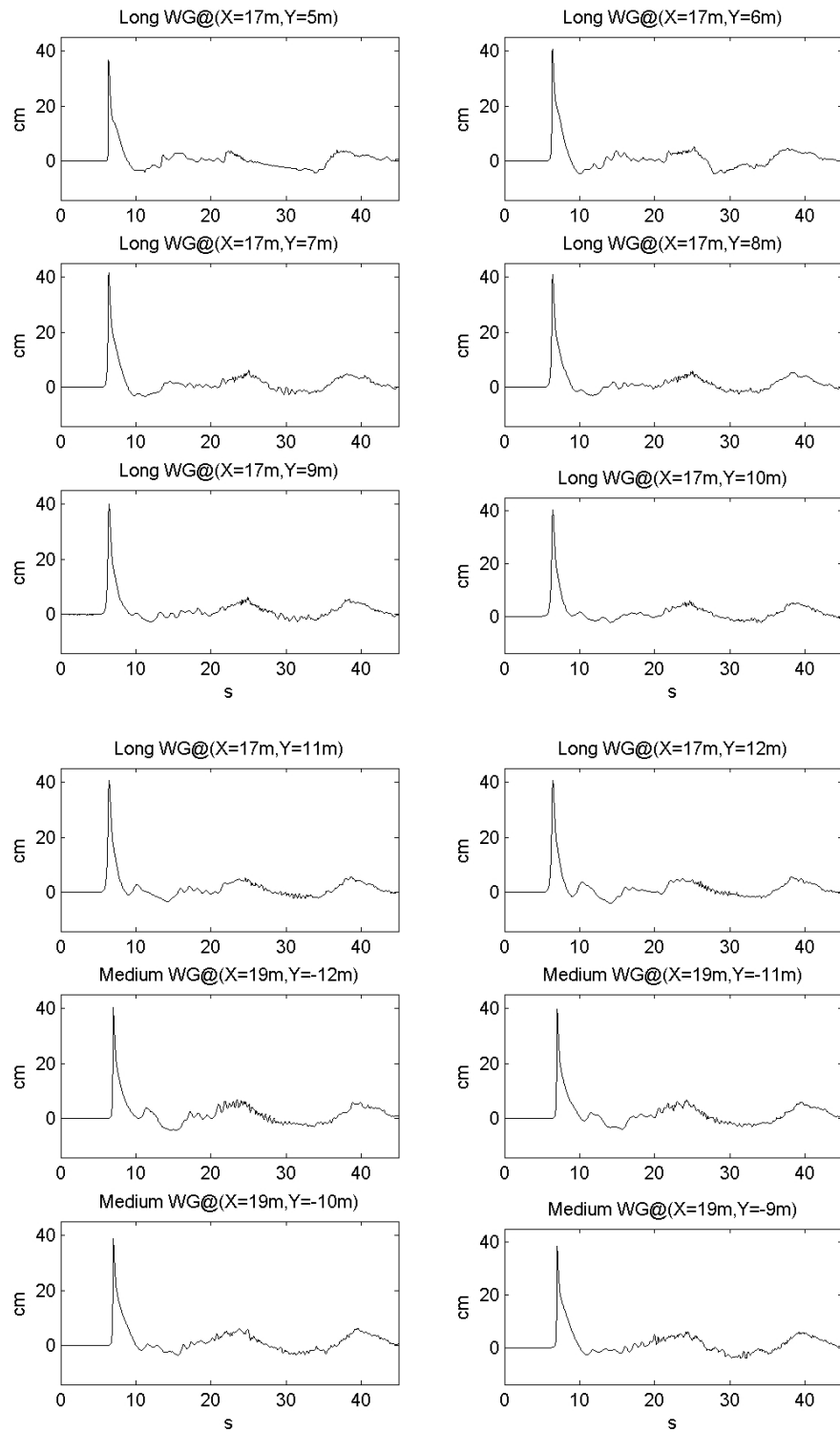
Figure 56: WG timeseries including X=17m, Y=5m to X=19m, Y=-9m.
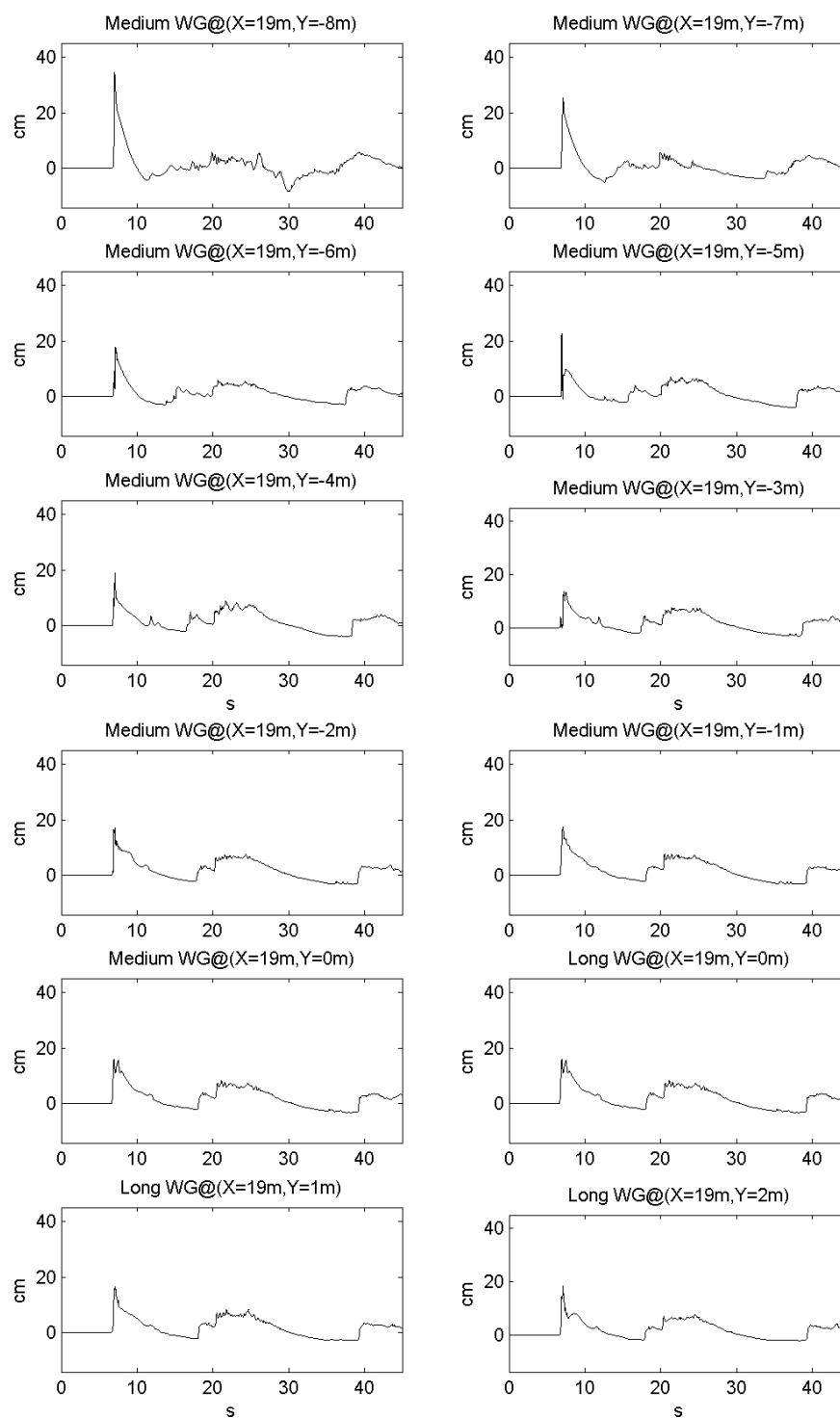
Figure 57: WG timeseries including X=19m, Y=-8m to X=19m, Y=2m.
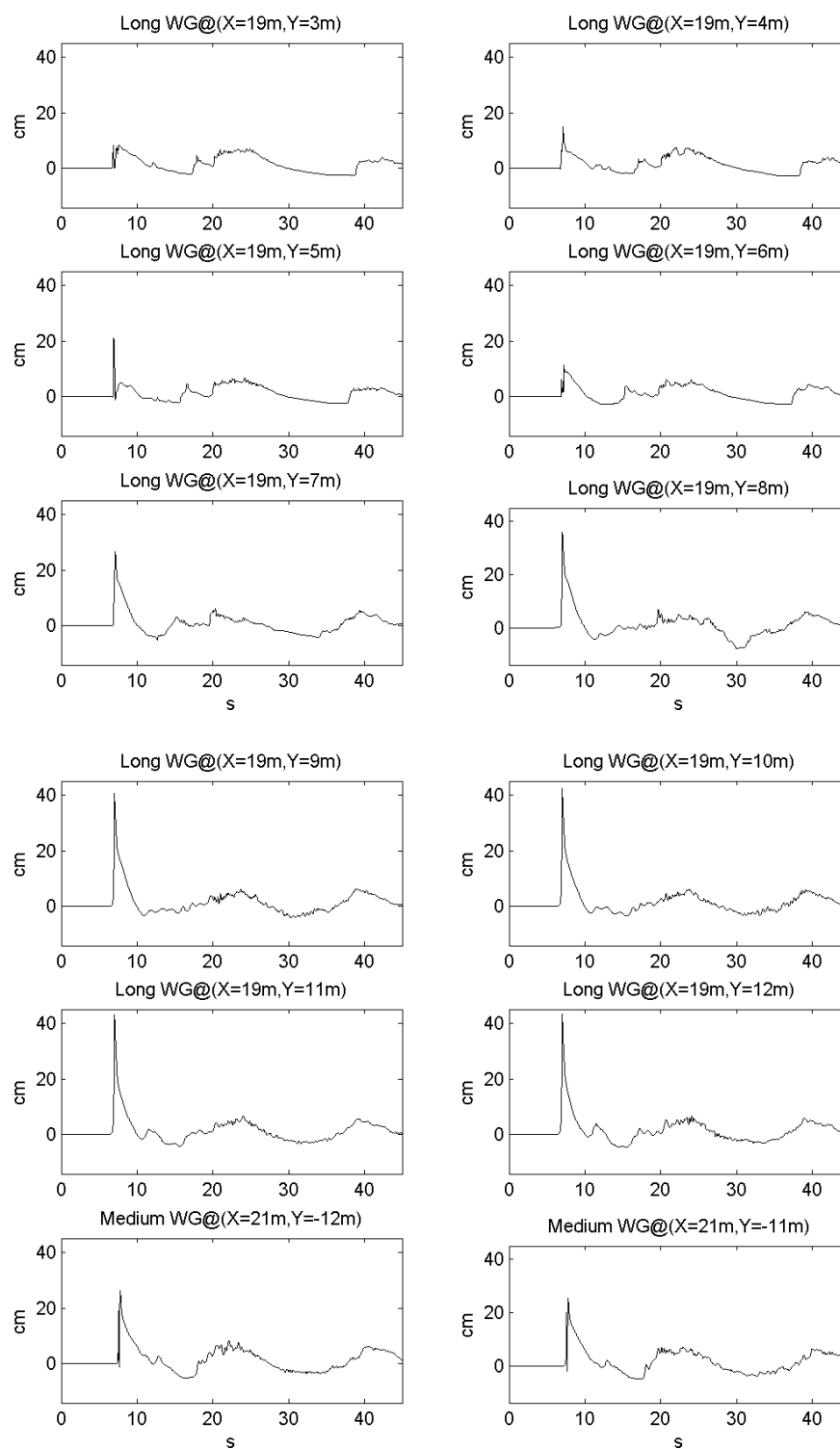
Figure 58: WG timeseries including X=19m, Y=3m to X=21m, Y=-11m.
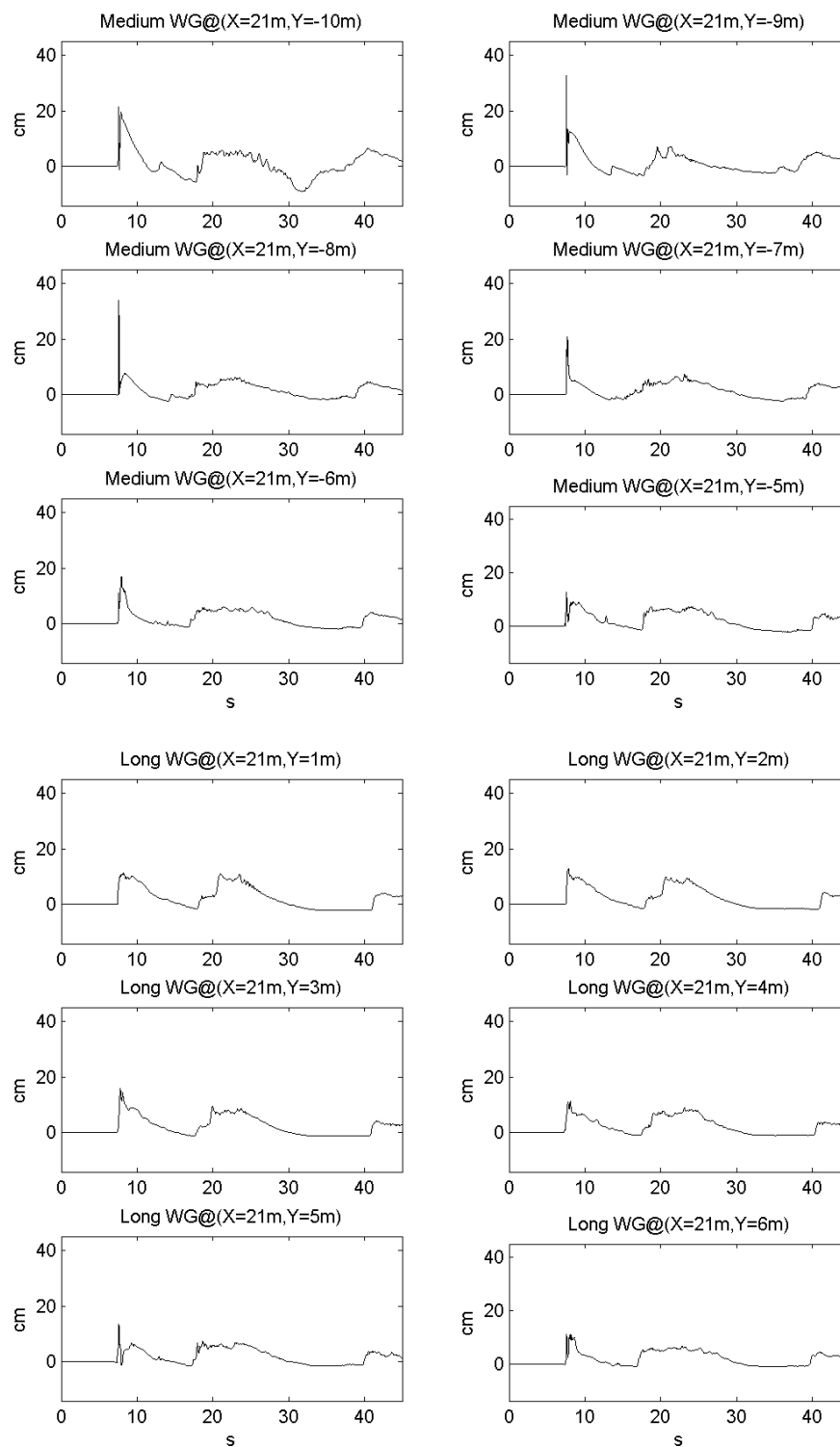
Figure 59: WG timeseries including X=21m, Y=-10m to X=21m, Y=6m.
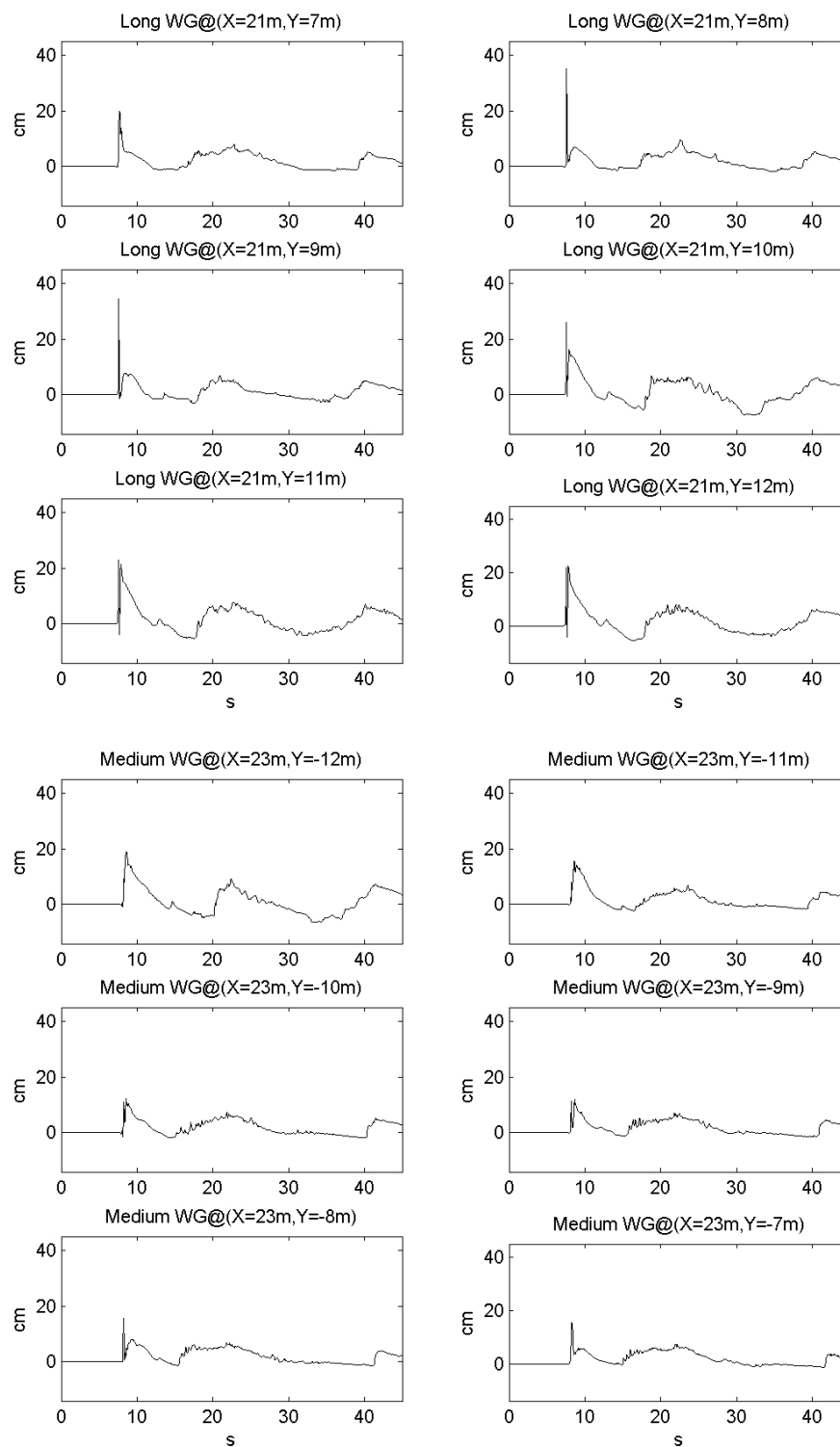
Figure 60: WG timeseries including X=21m, Y=7m to X=23m, Y=-7m.
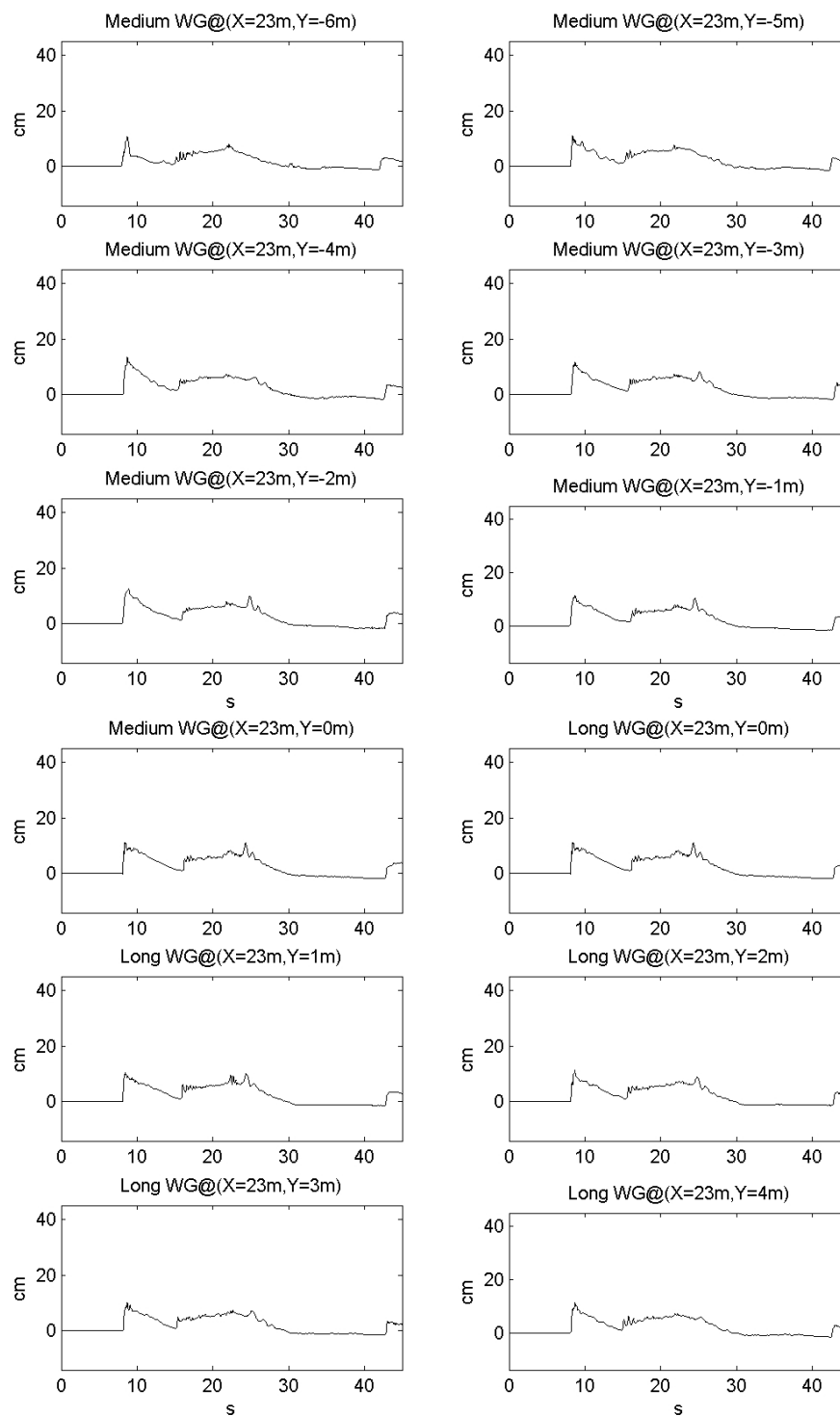
Figure 61: WG timeseries including X=23m, Y=-6m to X=23m, Y=4m.
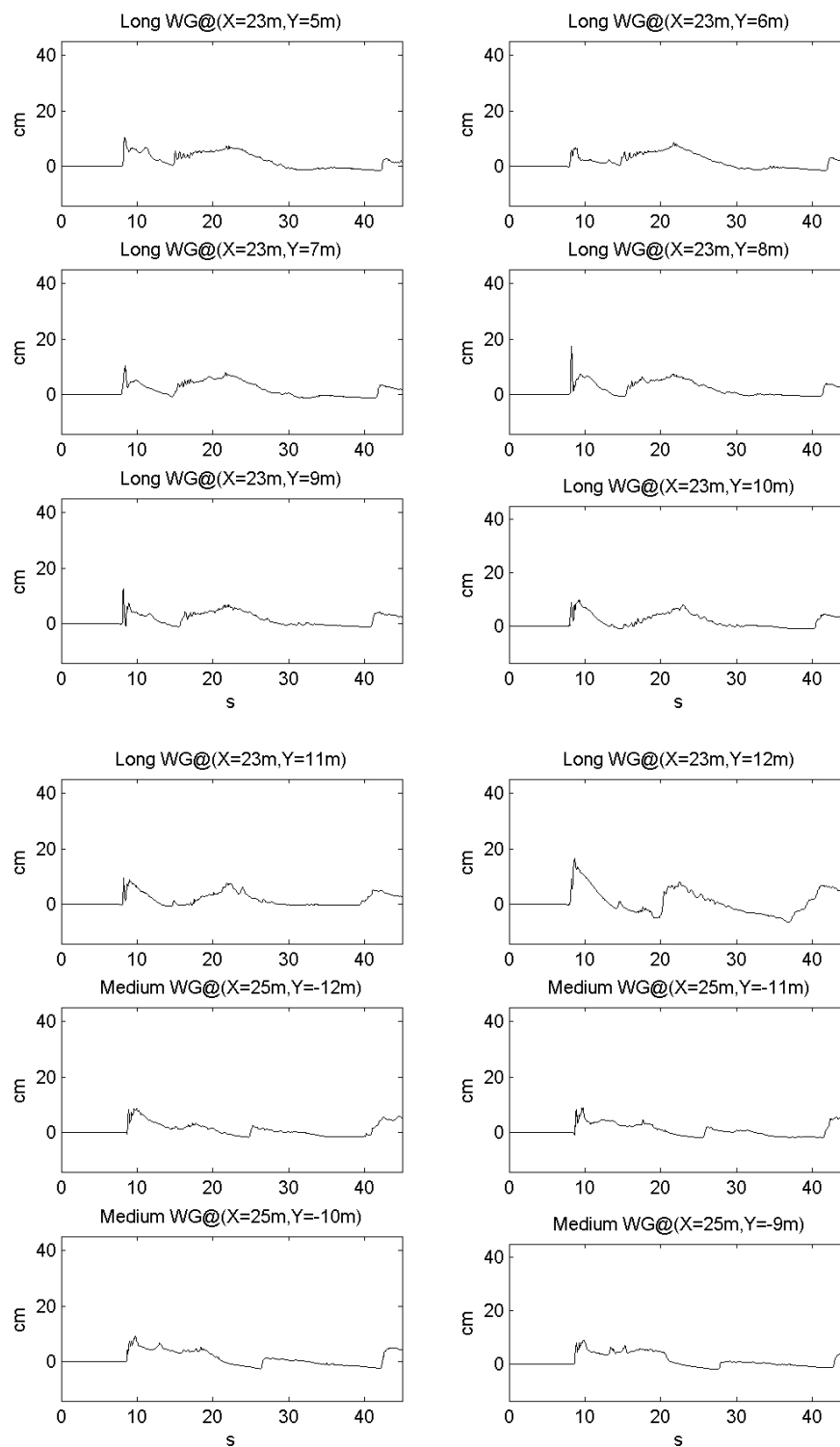
Figure 62: WG timeseries including X=23m, Y=5m to X=25m, Y=-9m.
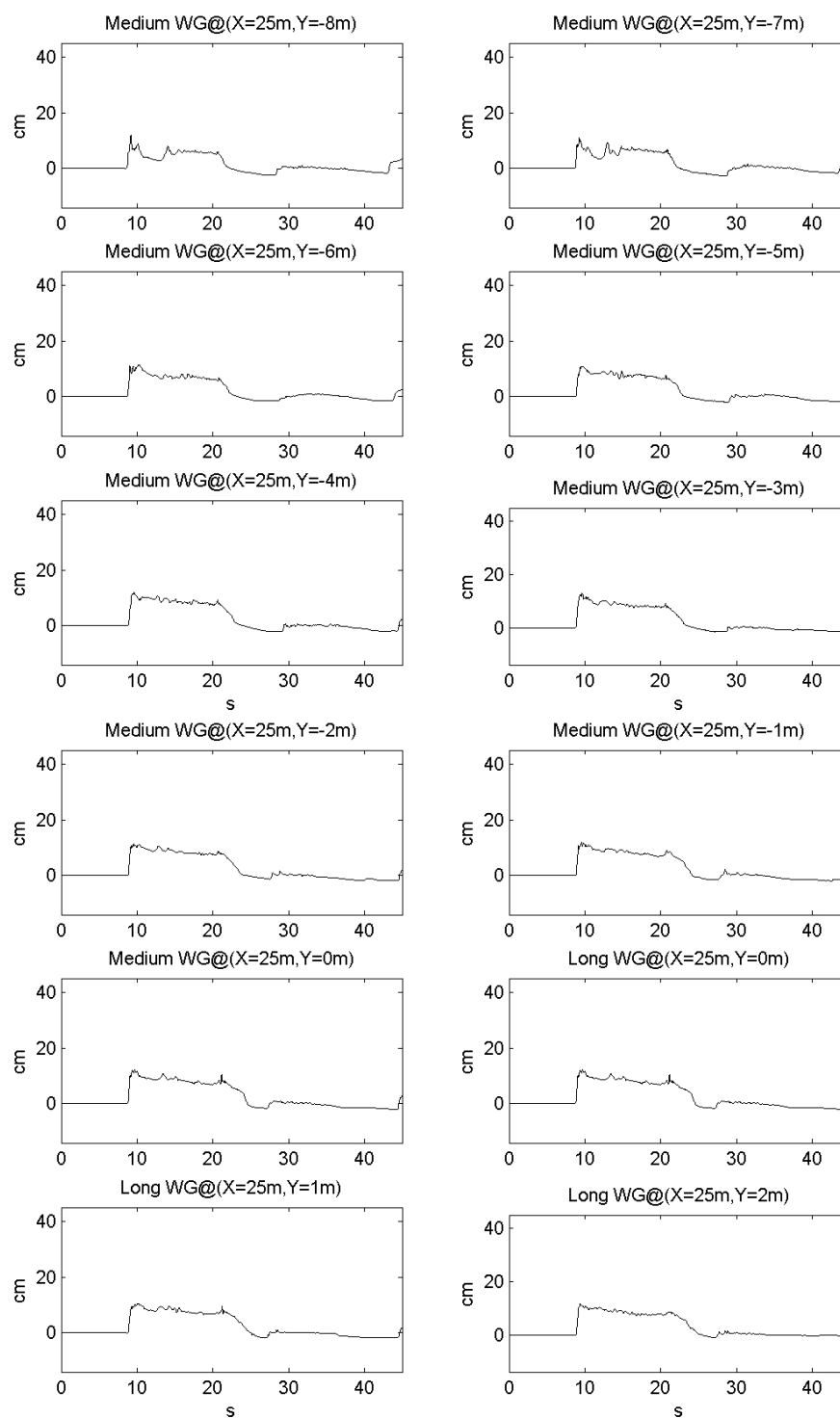
Figure 63: WG timeseries including X=25m, Y=-8m to X=25m, Y=2m.
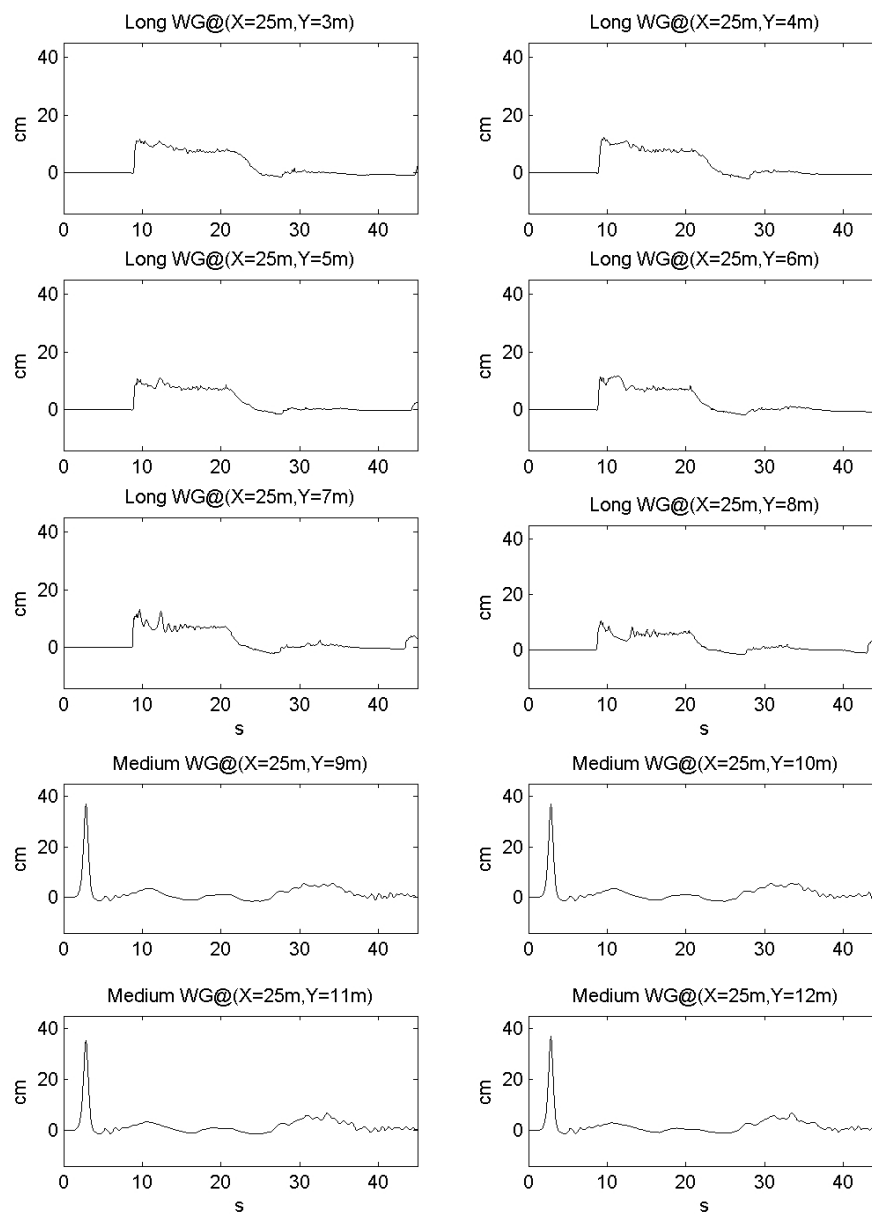
Figure 64: WG timeseries including X=25m, Y=3m to X=25m, Y=12m.

# APPENDIX II:  COMPLETE ADV PRESENTATION

The ADV timeseries presented below are organized moving in the positive longshore direction, the positive cross-shore location, and the positive vertical direction starting at X=9m, Y=0m, Z=0.43m and ending X=21m, Y=0m, Z=0.77m.
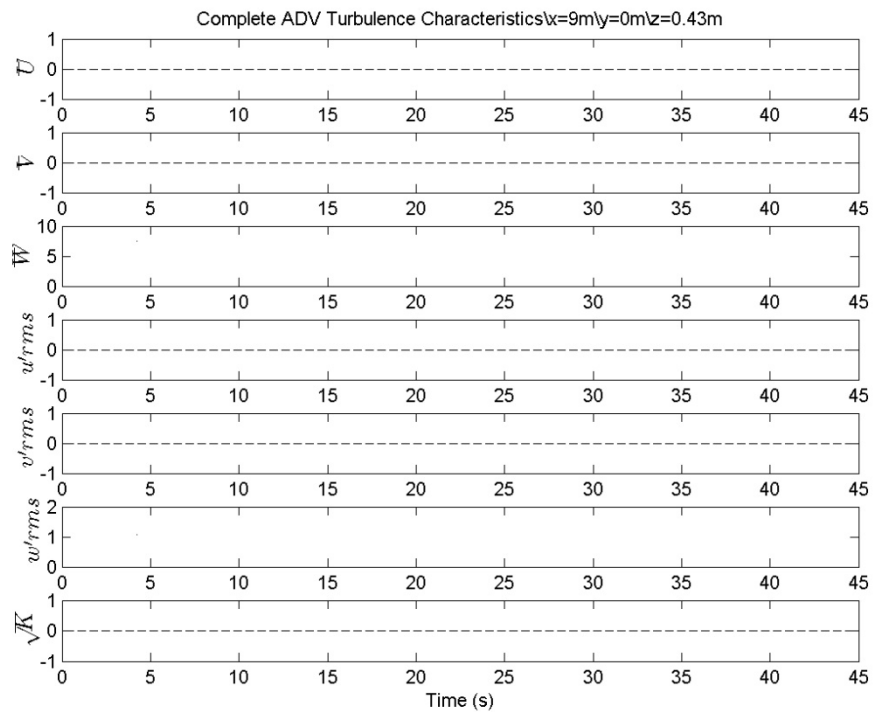


Figure 65:  Mean velocity, RMS turbulence, and $\sqrt{K}$ (cm/s) of ADV at X=9.0m, Y=0m, Z=0.43m.
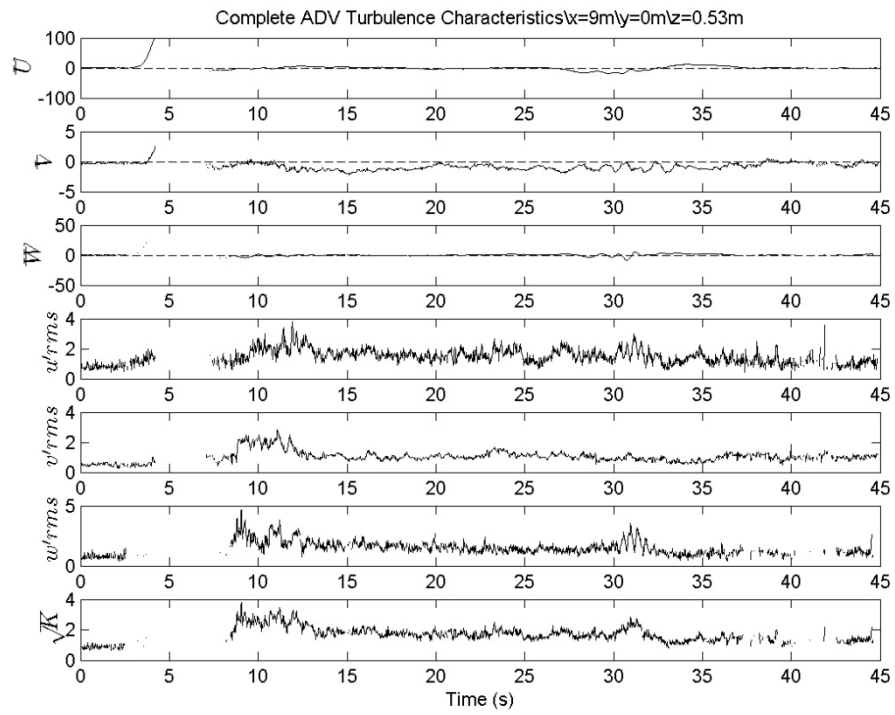
Figure 66:  Mean velocity, RMS turbulence, and $\sqrt{K}$ (cm/s) of ADV at X=9.0m, Y=0m, Z=0.53m.
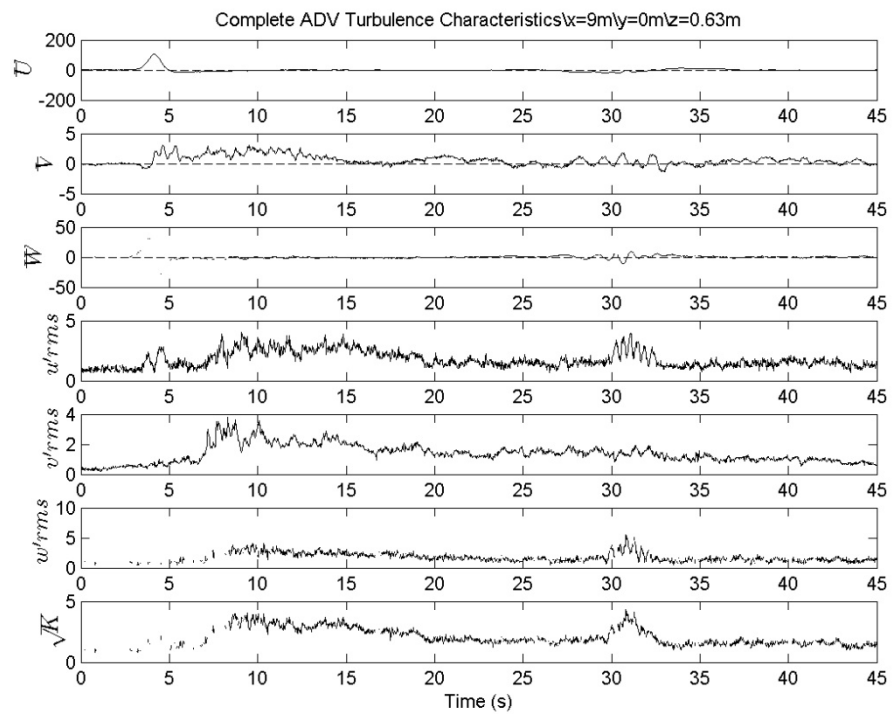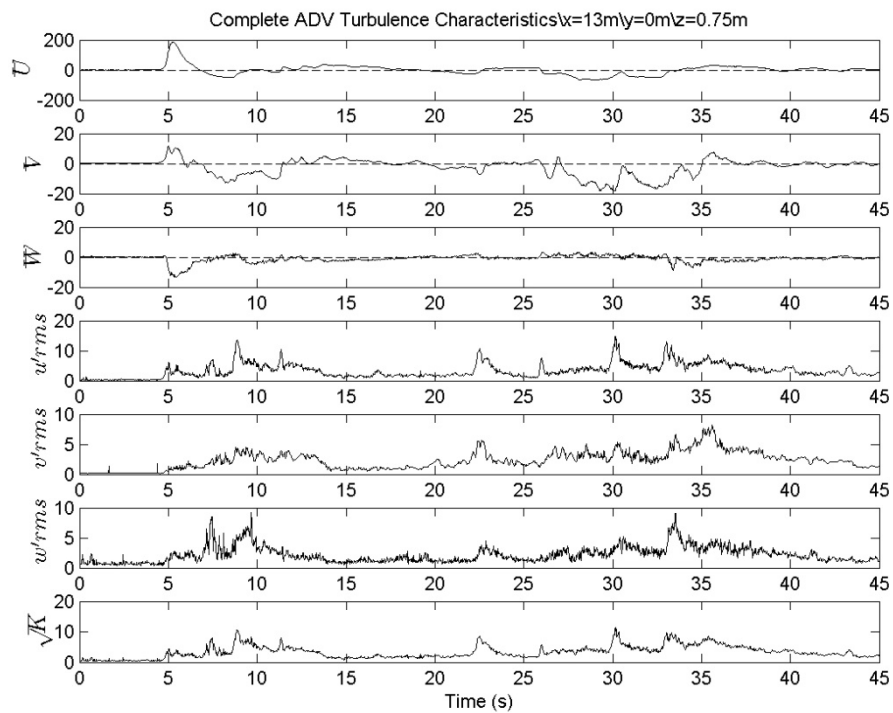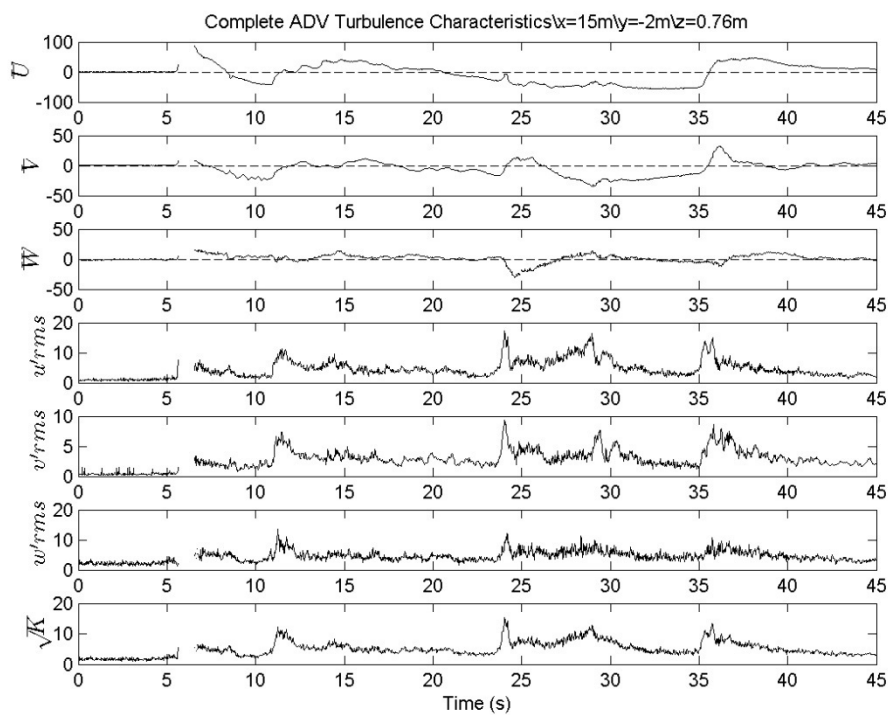


Figure 67:  Mean velocity, RMS turbulence, and $\sqrt{K}$ (cm/s) of ADV at X=9.0m, Y=0m, Z=0.63m.
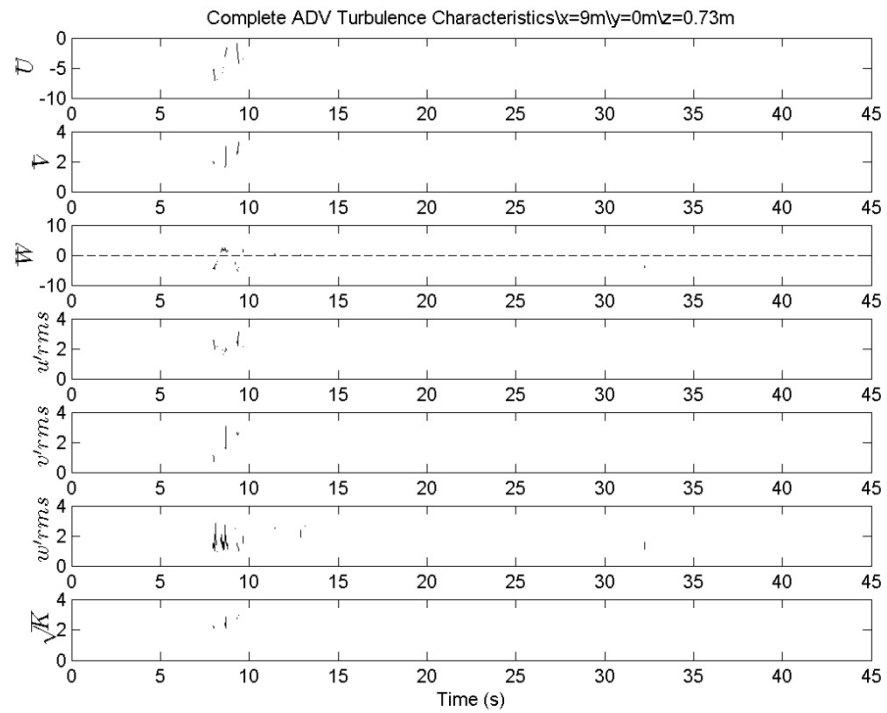
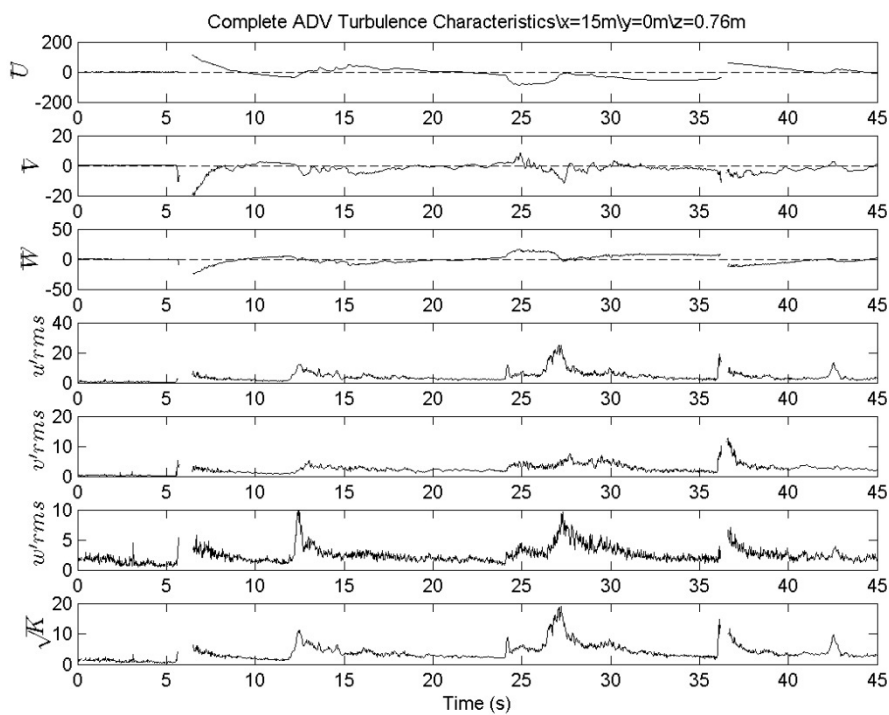Figure 68:  Mean velocity, RMS turbulence, and $\sqrt{K}$ (cm/s) of ADV at X=9.0m, Y=0m, Z=0.73m.
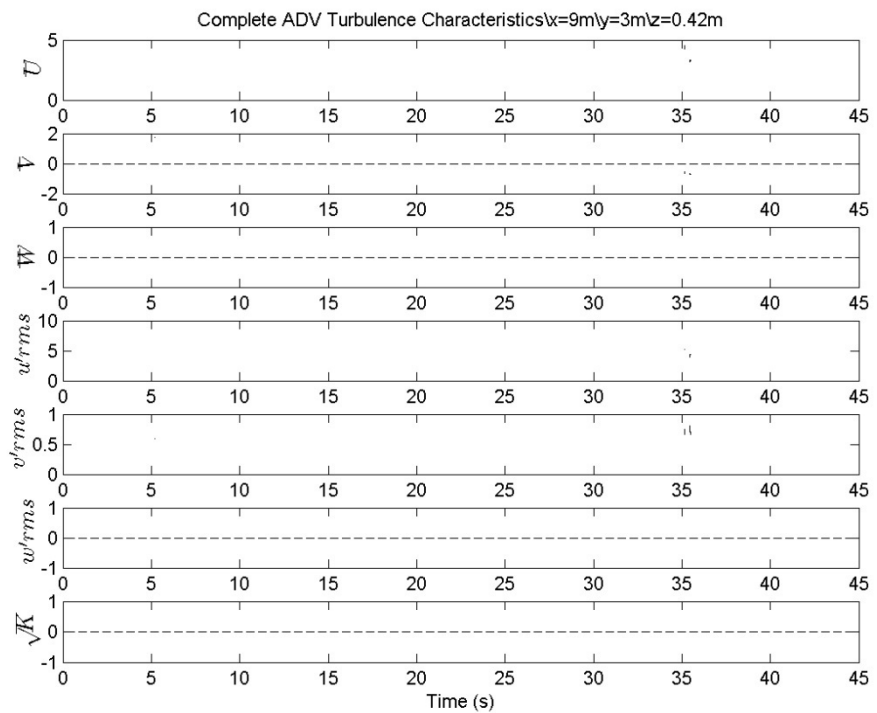


Figure 69:  Mean velocity, RMS turbulence, and $\sqrt{K}$ (cm/s) of ADV at X=9.0m, Y=3m, Z=0.42m.
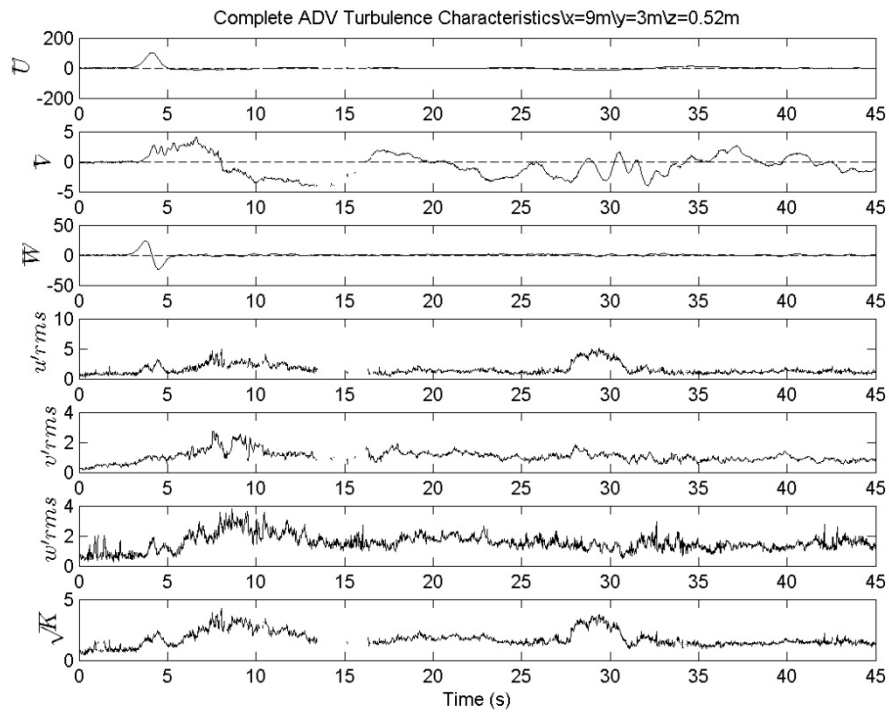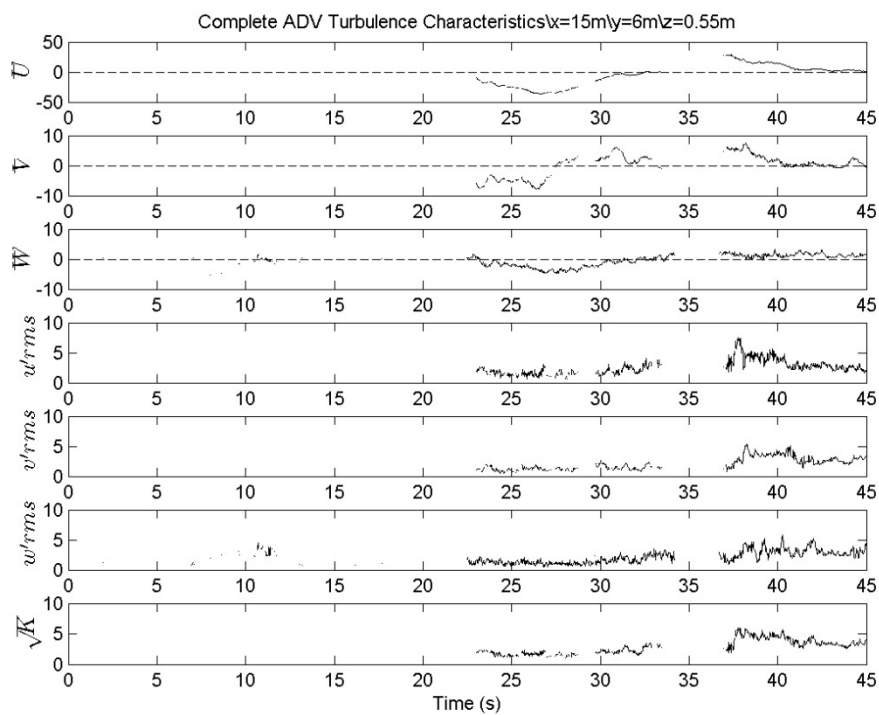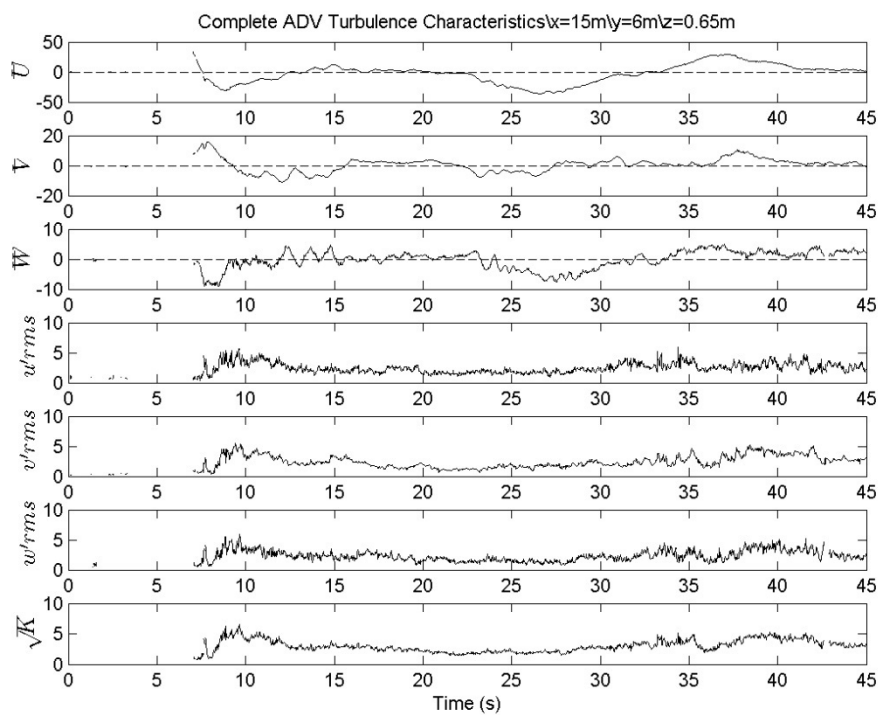
Figure 70:  Mean velocity, RMS turbulence, and $\sqrt{K}$ (cm/s) of ADV at X=9.0m, Y=3m, Z=0.52m.
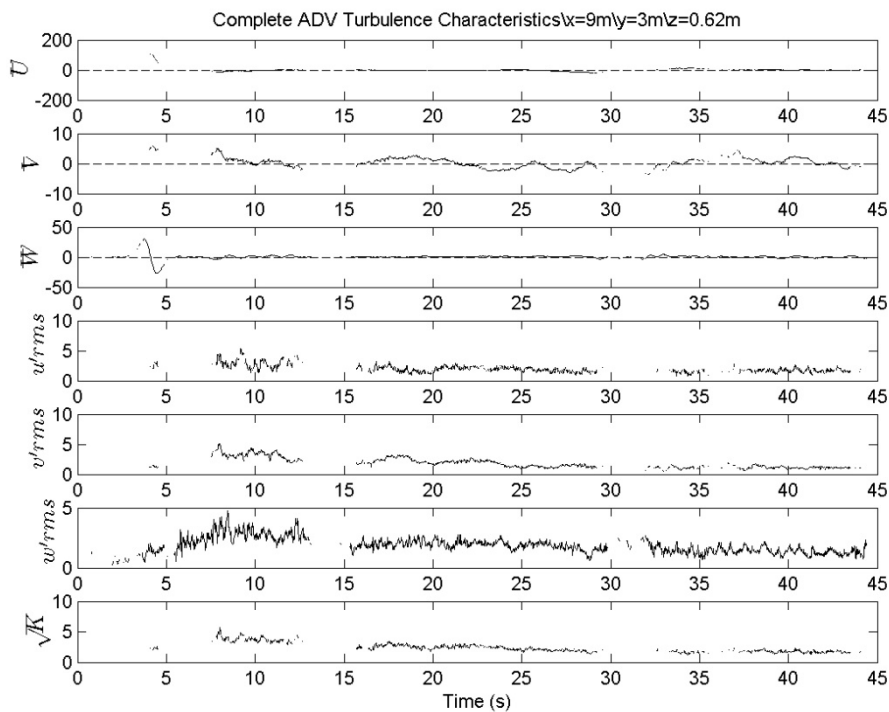


Figure 71:  Mean velocity, RMS turbulence, and $\sqrt{K}$ (cm/s) of ADV at X=9.0m, Y=3m, Z=0.62m.
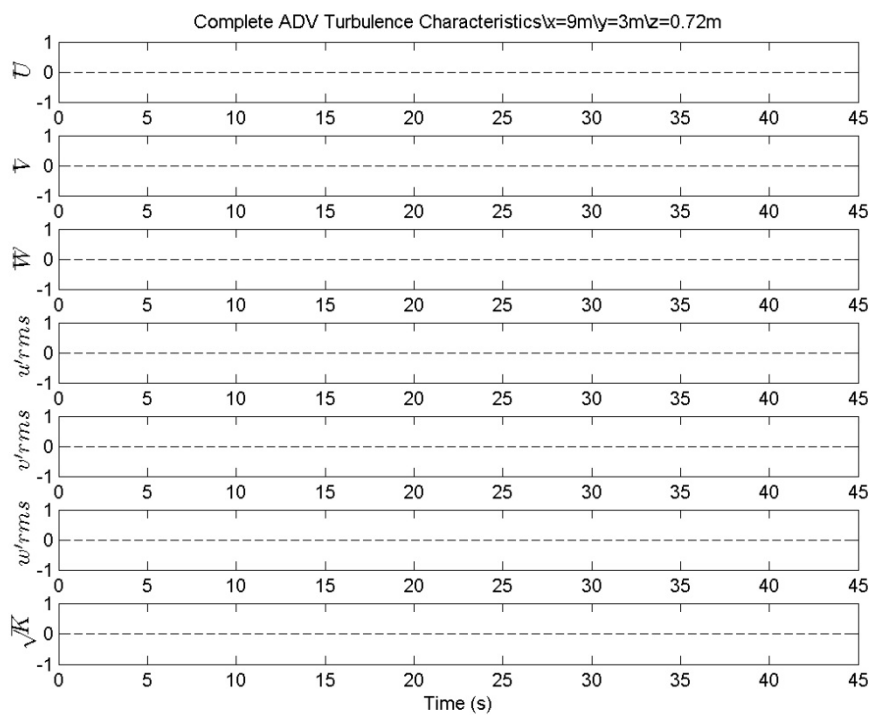
Figure 72:  Mean velocity, RMS turbulence, and $\sqrt{K}$ (cm/s) of ADV at X=9.0m, Y=3m, Z=0.72m.
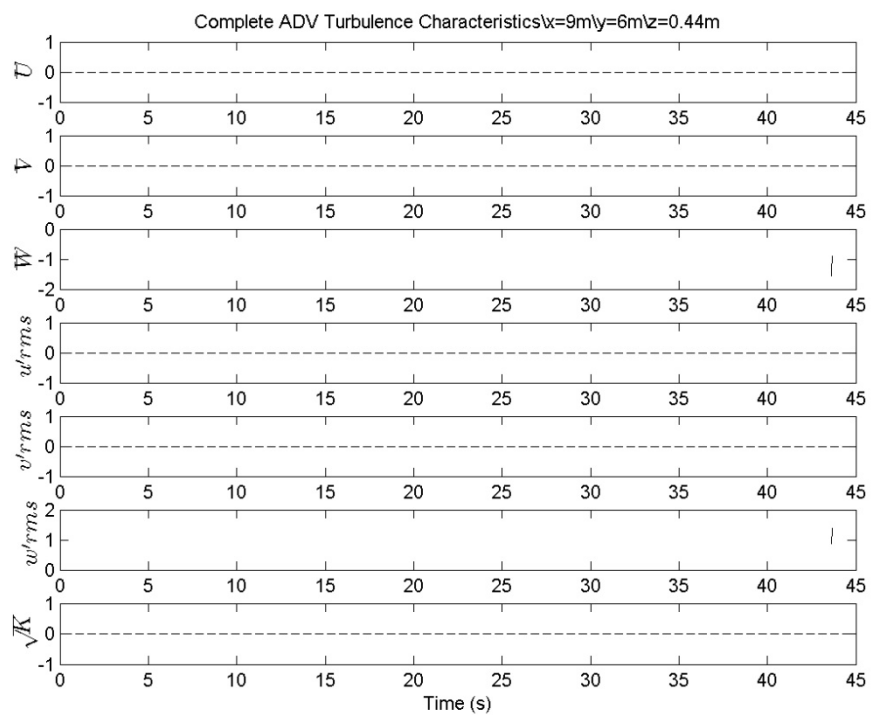


Figure 73:  Mean velocity, RMS turbulence, and $\sqrt{K}$ (cm/s) of ADV at X=9.0m, Y=6m, Z=0.44m.
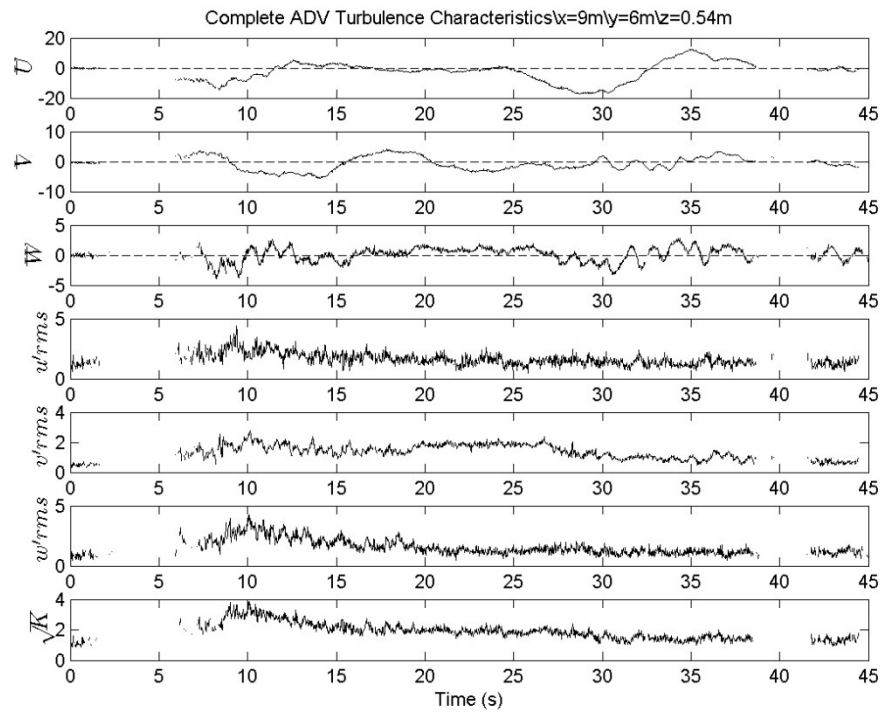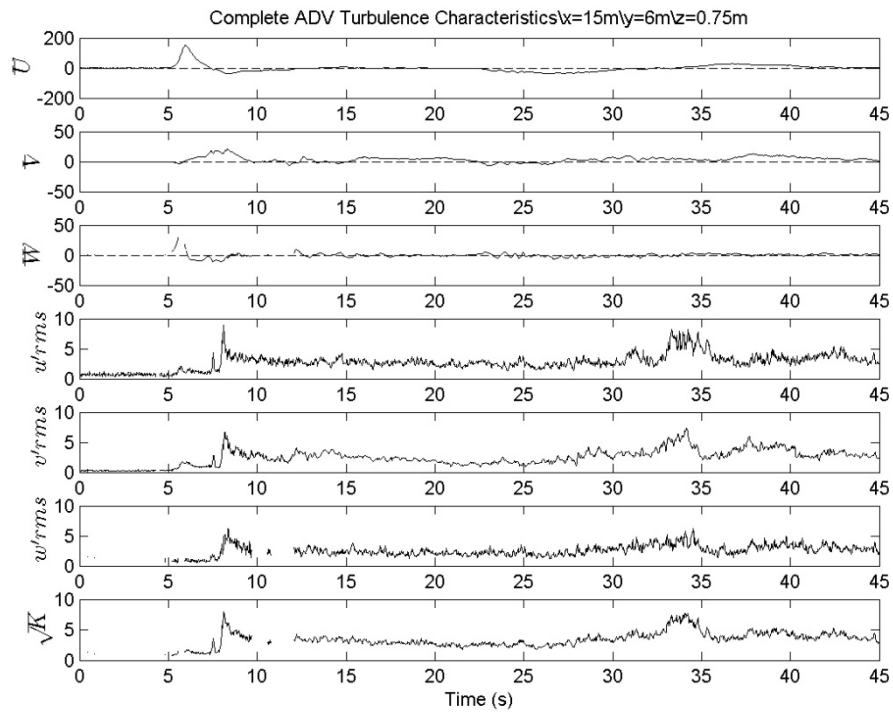
Figure 74: Mean velocity, RMS turbulence, and $\sqrt{K}$ (cm/s) of ADV at X=9.0m, Y=6m, Z=0.54m.
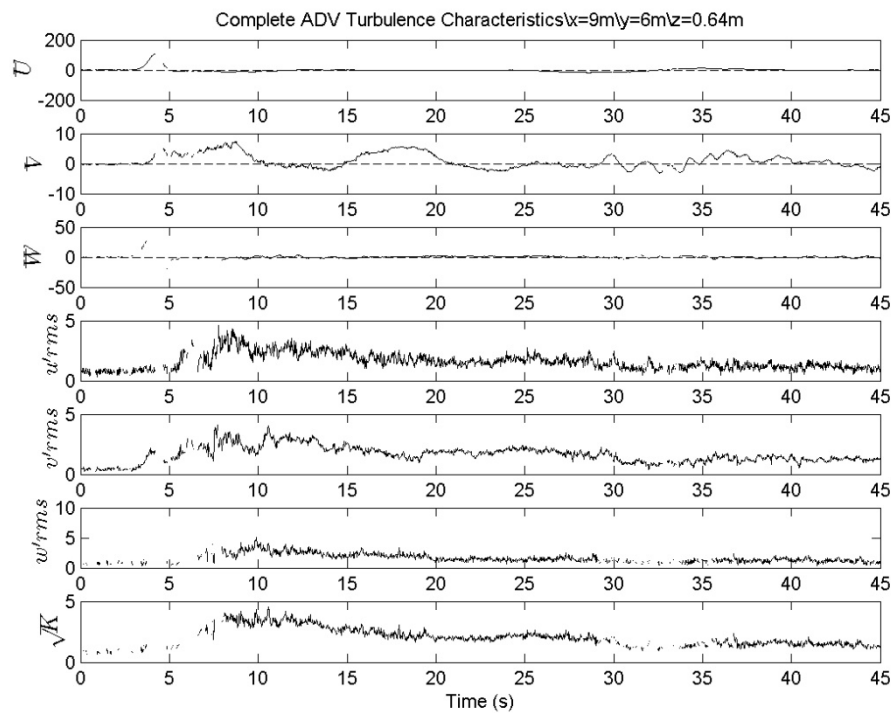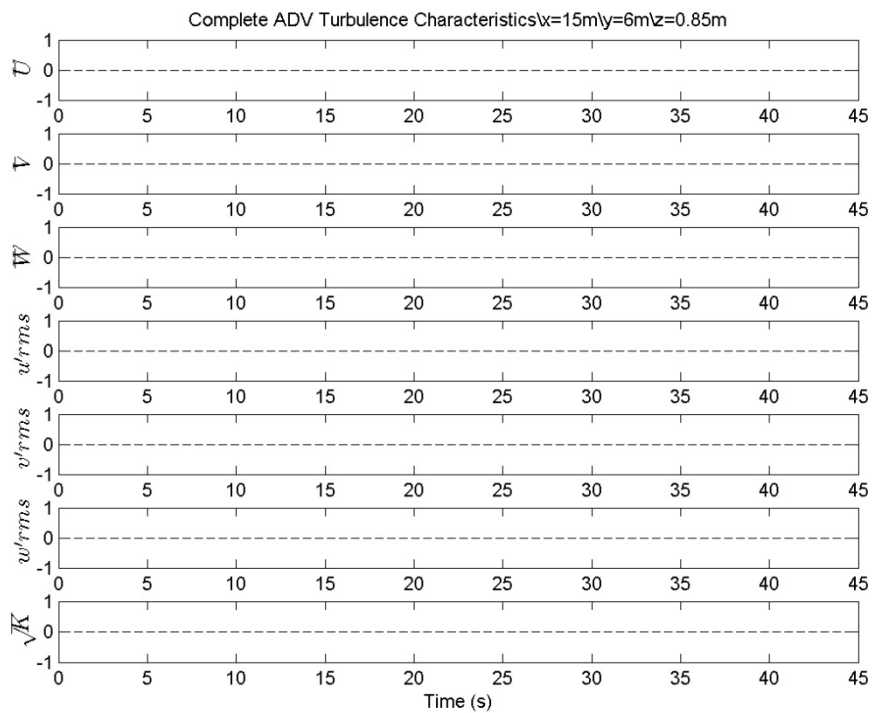


Figure 75: Mean velocity, RMS turbulence, and $\sqrt{K}$ (cm/s) of ADV at X=9.0m, Y=6m, Z=0.64m.
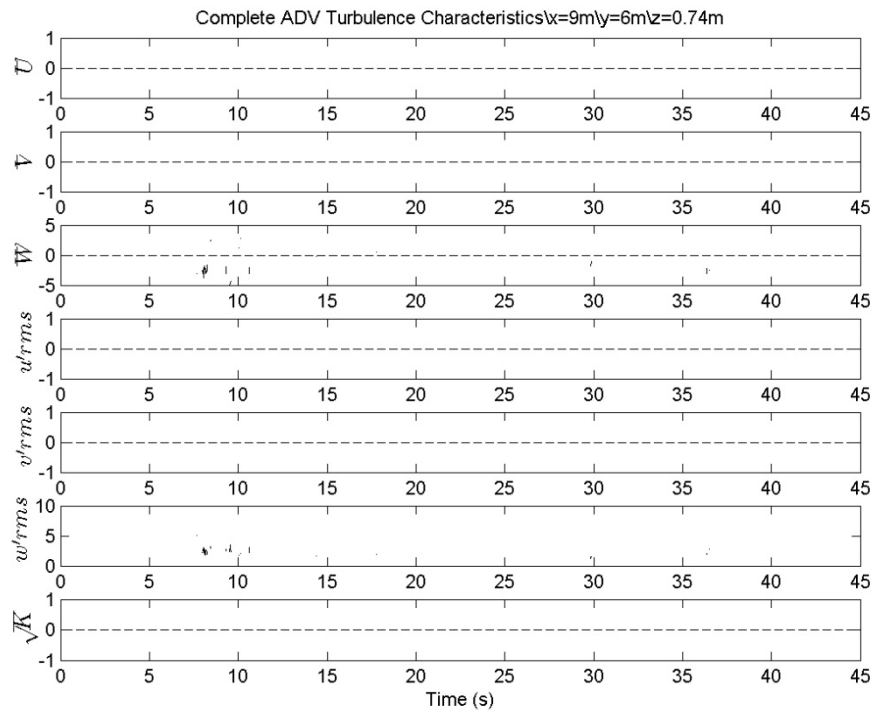
Figure 76: Mean velocity, RMS turbulence, and $\sqrt{K}$ (cm/s) of ADV at X=9.0m, Y=6m, Z=0.74m.
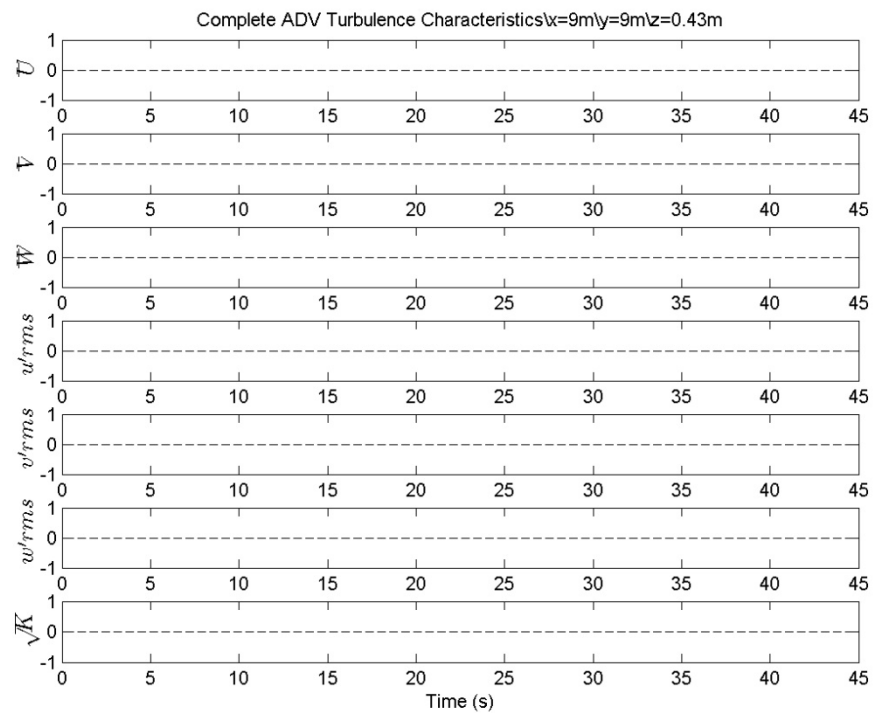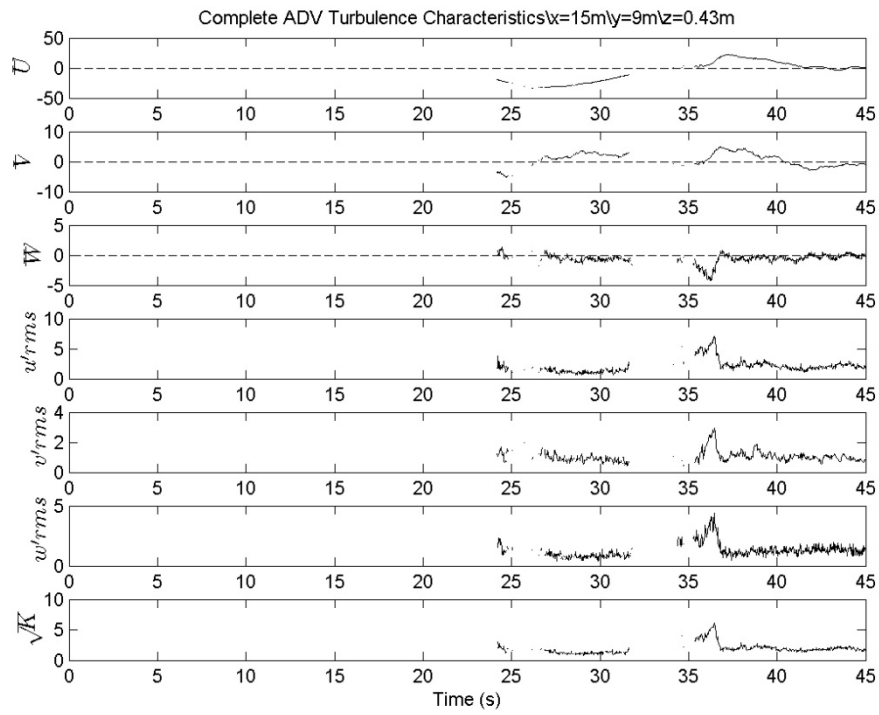


Figure 77: Mean velocity, RMS turbulence, and $\sqrt{K}$ (cm/s) of ADV at X=9.0m, Y=9m, Z=0.43m.
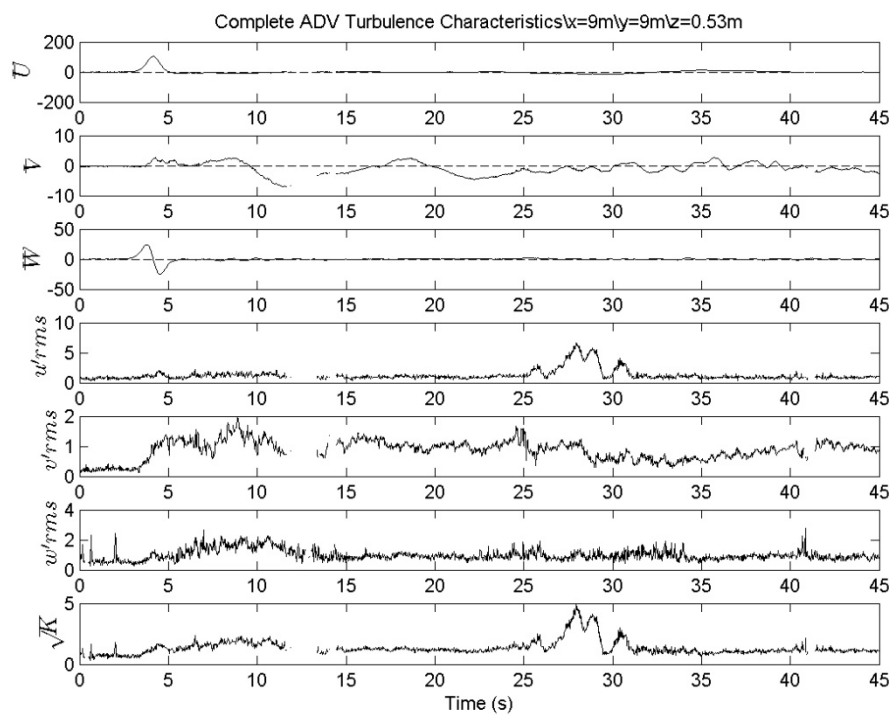
Figure 78: Mean velocity, RMS turbulence, and $\sqrt{K}$ (cm/s) of ADV at X=9.0m, Y=9m, Z=0.53m.
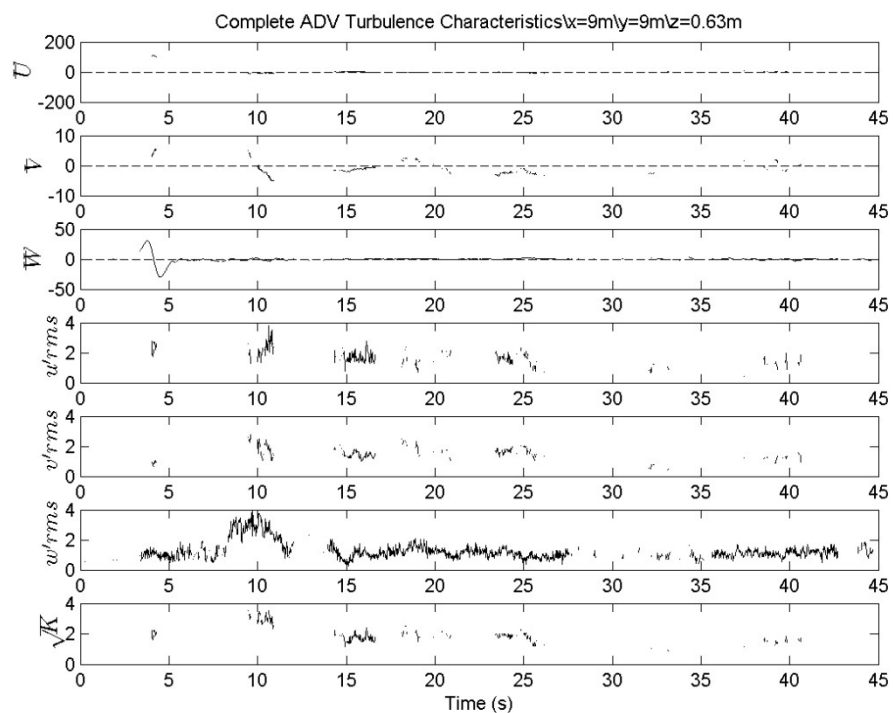


Figure 79: Mean velocity, RMS turbulence, and $\sqrt{K}$ (cm/s) of ADV at X=9.0m, Y=9m, Z=0.63m.
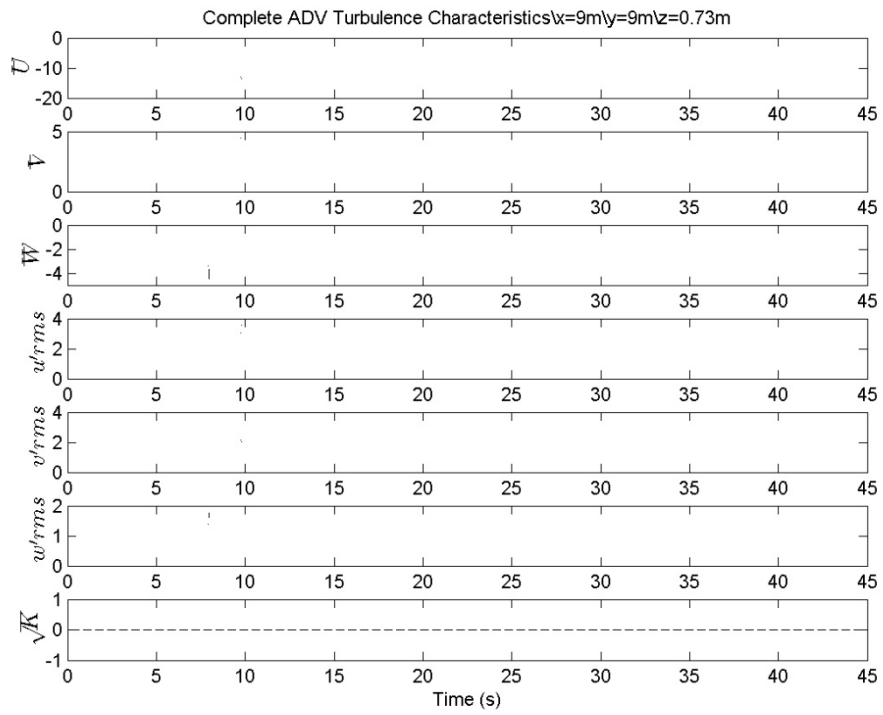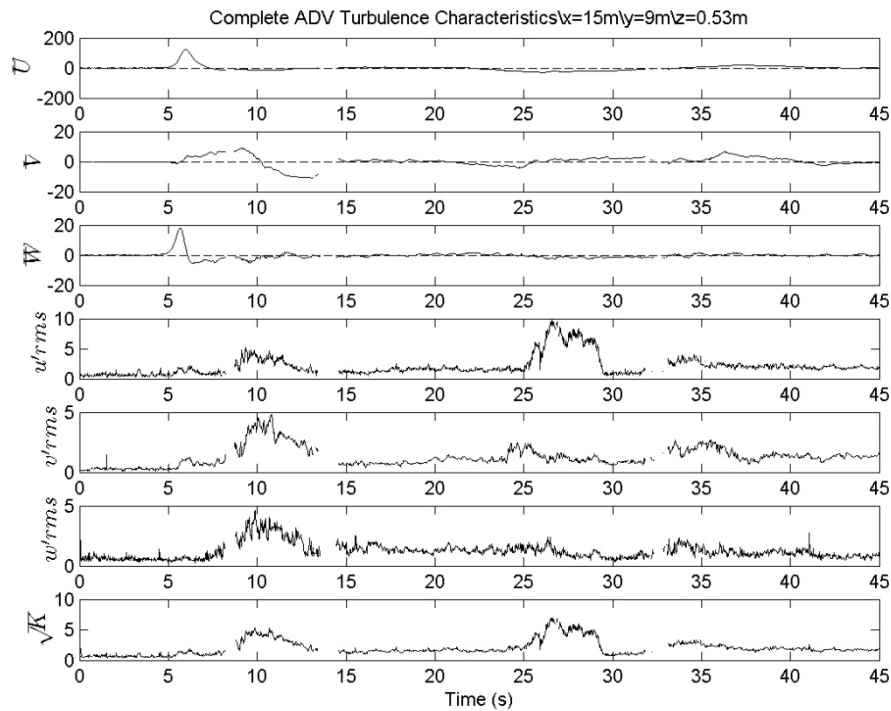
Figure 80: Mean velocity, RMS turbulence, and $\sqrt{K}$ (cm/s) of ADV at X=9.0m, Y=9m, Z=0.73m.
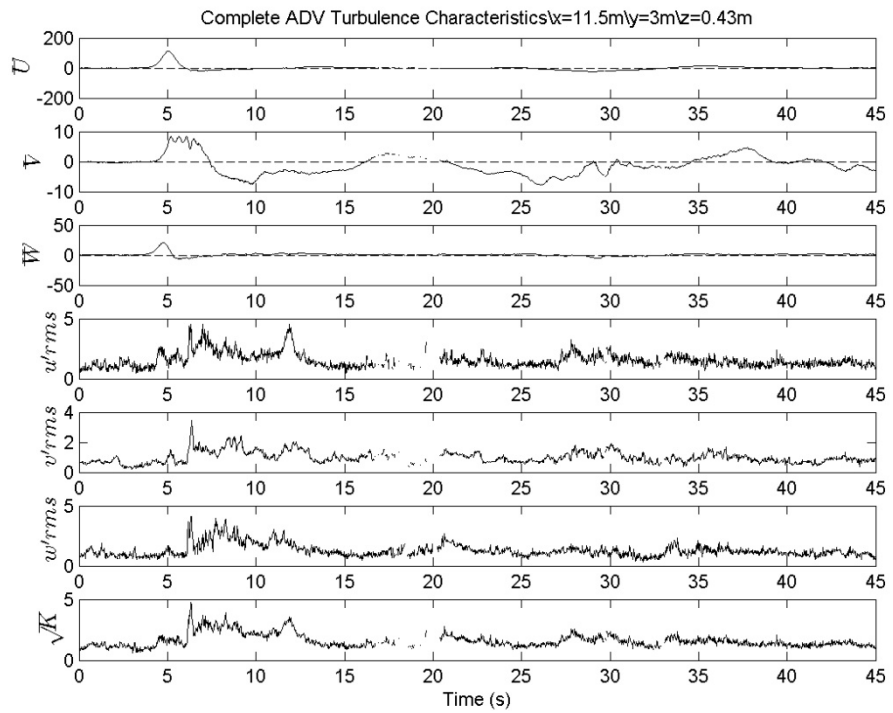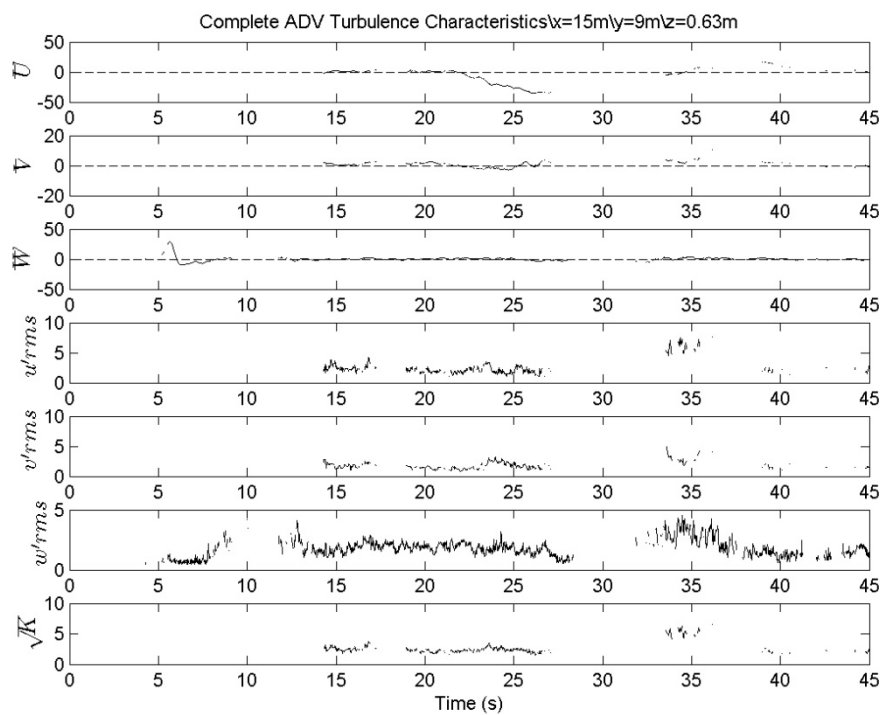


Figure 81: Mean velocity, RMS turbulence, and $\sqrt{K}$ (cm/s) of ADV at X=11.5m, Y=3m, Z=0.43m.
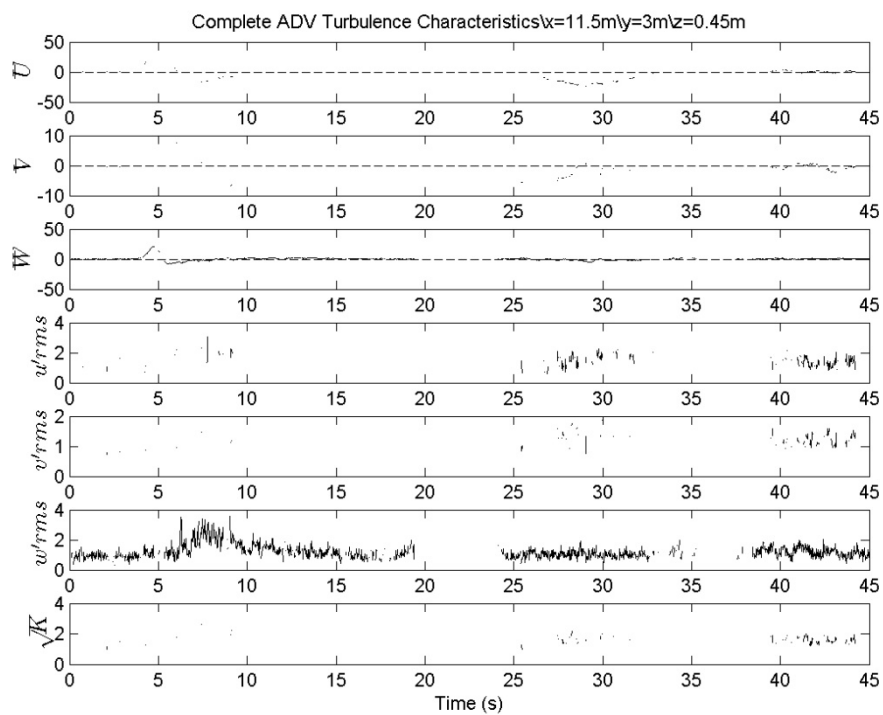
Figure 82: Mean velocity, RMS turbulence, and $\sqrt{K}$ (cm/s) of ADV at X=11.5m, Y=3m, Z=0.45m.
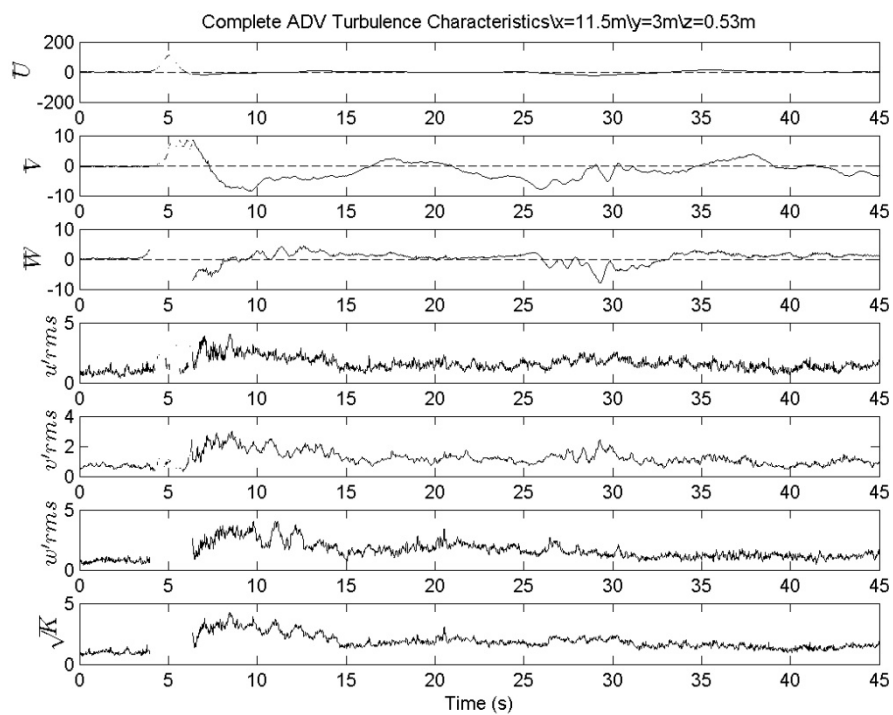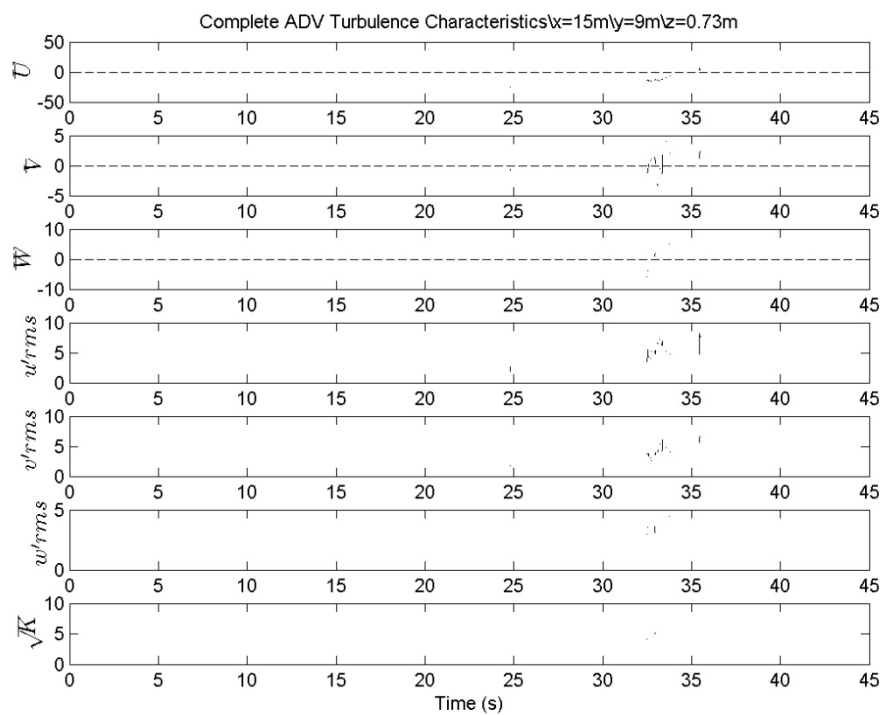


Figure 83: Mean velocity, RMS turbulence, and $\sqrt{K}$ (cm/s) of ADV at X=11.5m, Y=3m, Z=0.53m.
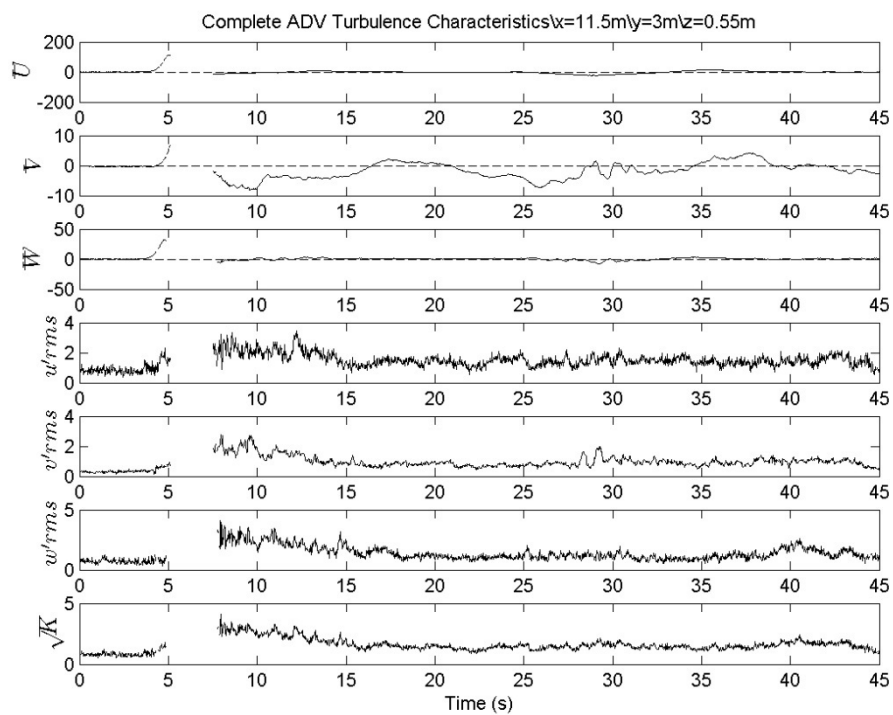
Figure 84: Mean velocity, RMS turbulence, and $\sqrt{K}$ (cm/s) of ADV at X=11.5m, Y=3m, Z=0.55m.
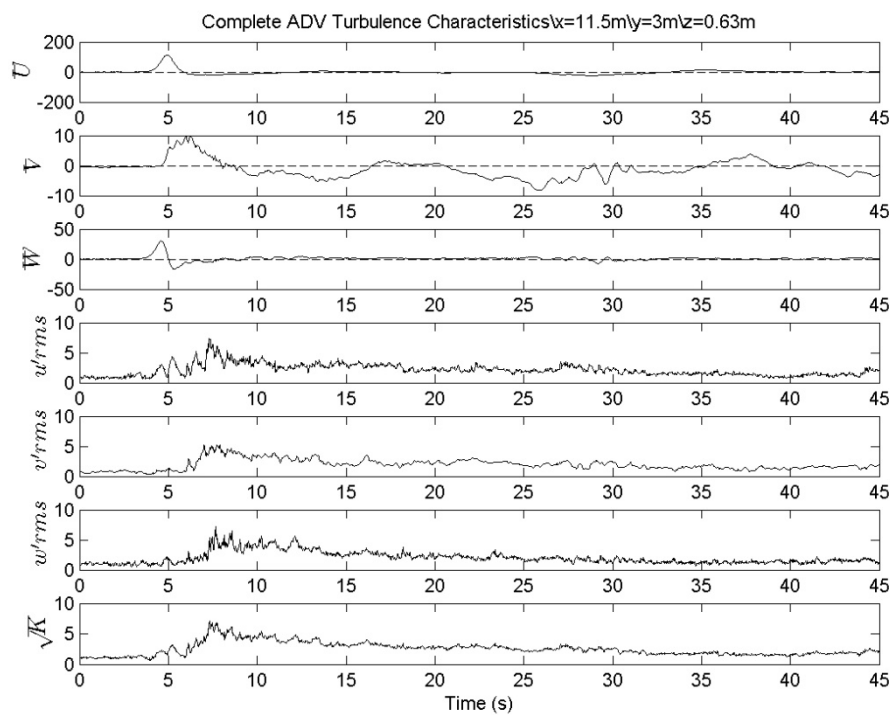


Figure 85: Mean velocity, RMS turbulence, and $\sqrt{K}$ (cm/s) of ADV at X=11.5m, Y=3m, Z=0.63m.
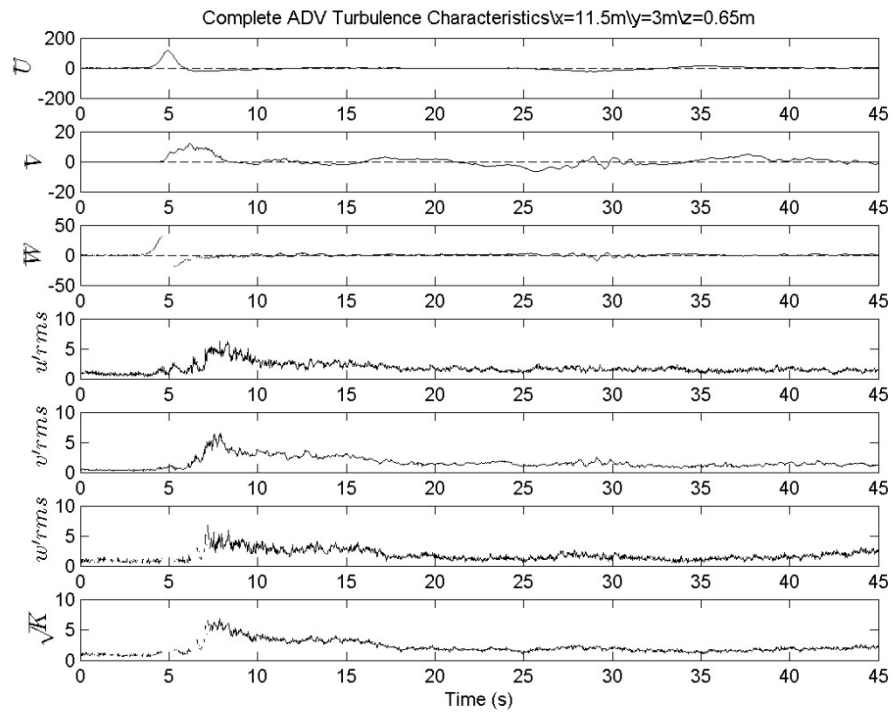
Figure 86:  Mean velocity, RMS turbulence, and $\sqrt{K}$ (cm/s) of ADV at X=11.5m, Y=3m, Z=0.65m.
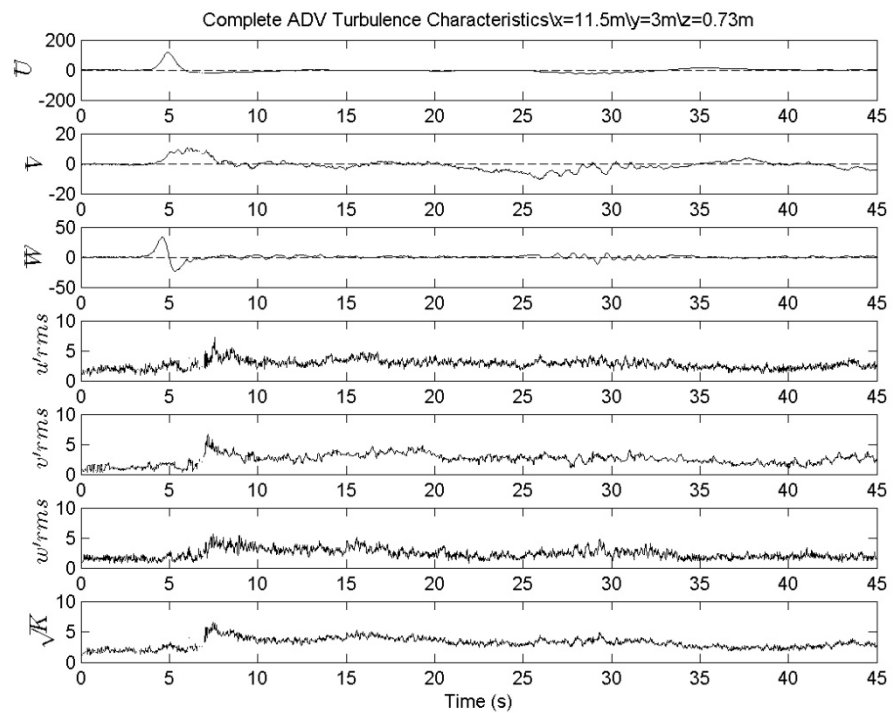


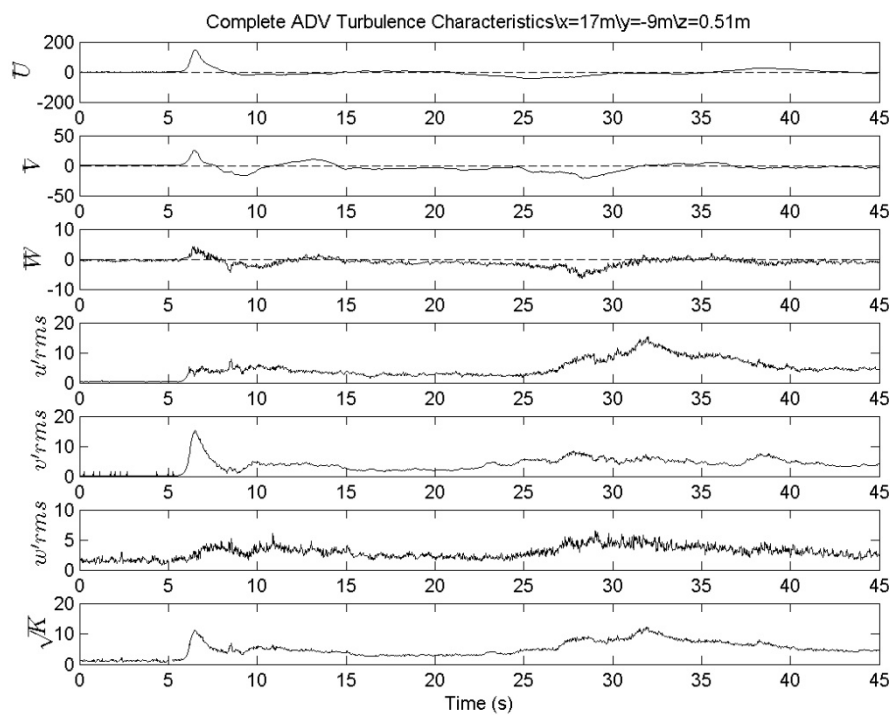Figure 87:  Mean velocity, RMS turbulence, and $\sqrt{K}$ (cm/s) of ADV at X=11.5m, Y=3m, Z=0.73m.
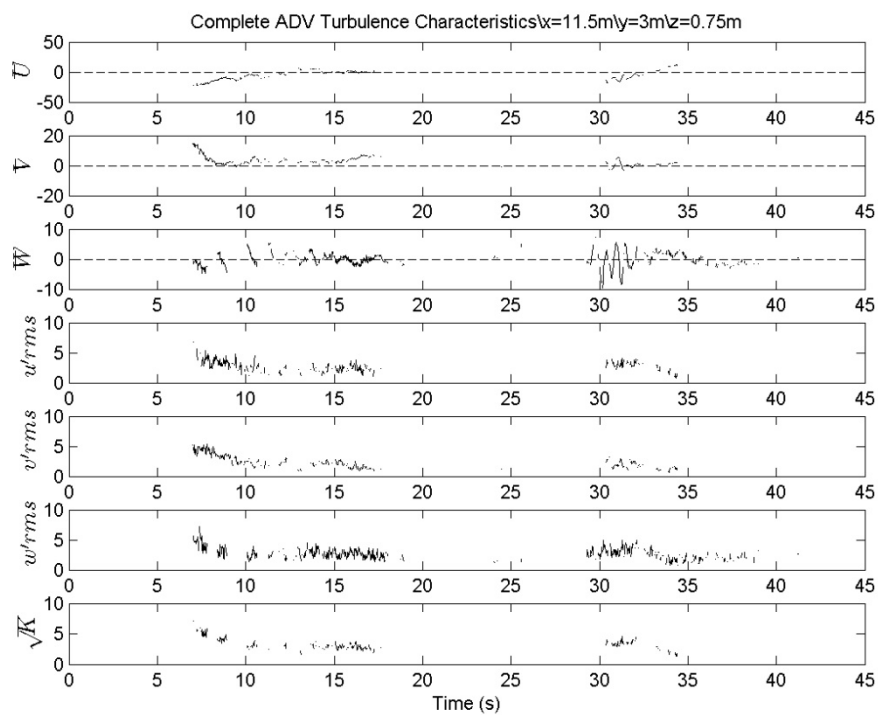
Figure 88: Mean velocity, RMS turbulence, and $\sqrt{K}$ (cm/s) of ADV at X=11.5m, Y=3m, Z=0.75m.
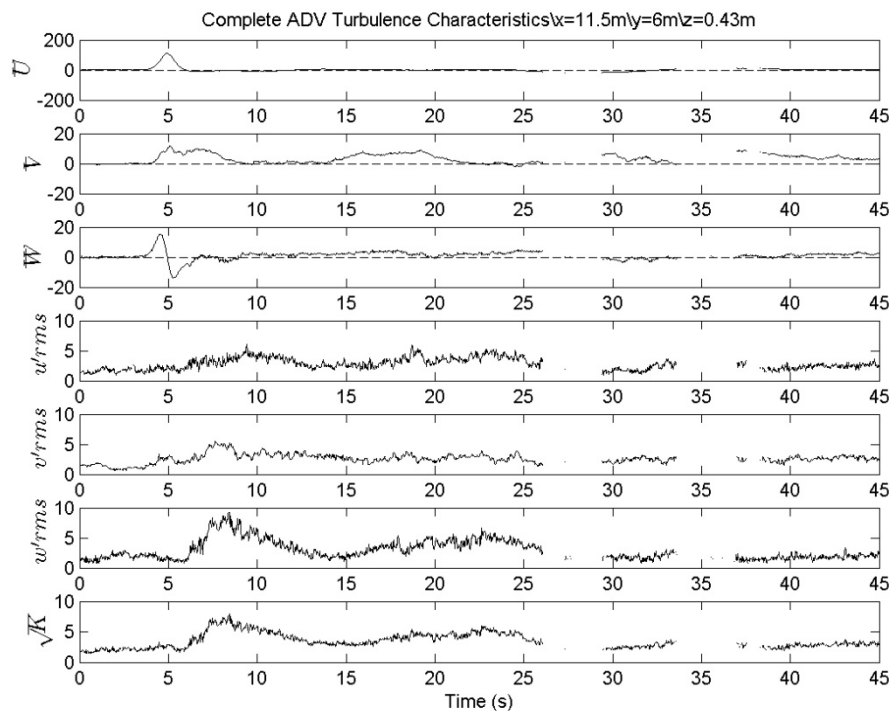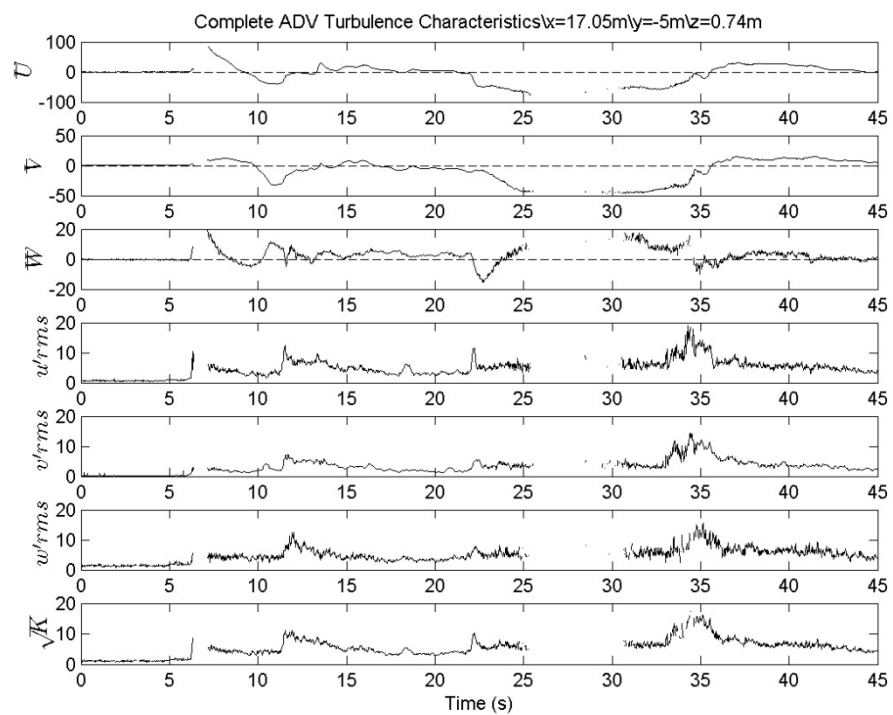


Figure 89: Mean velocity, RMS turbulence, and $\sqrt{K}$ (cm/s) of ADV at X=11.5m, Y=6m, Z=0.43m.
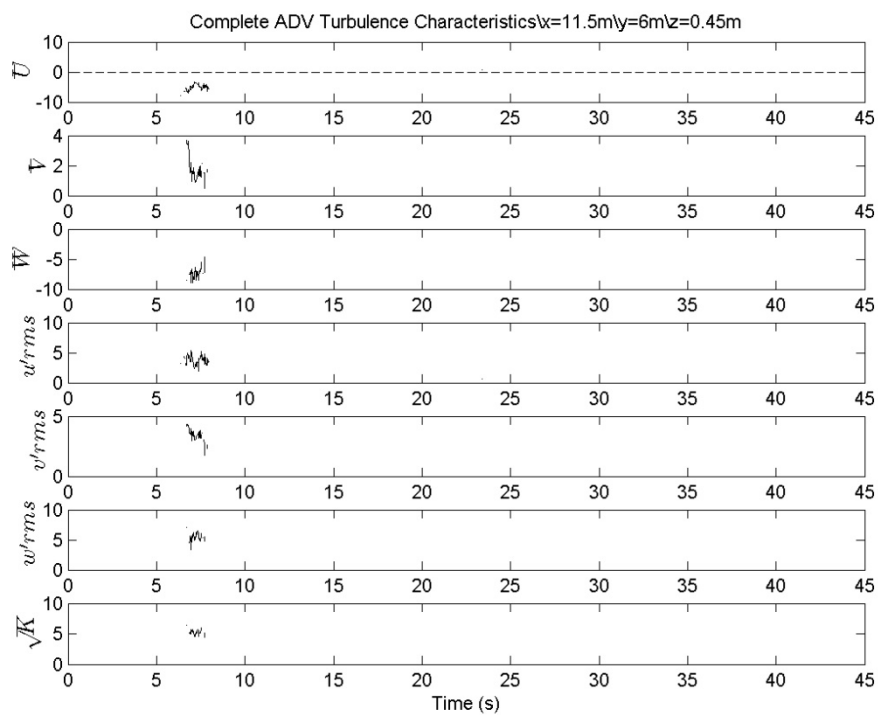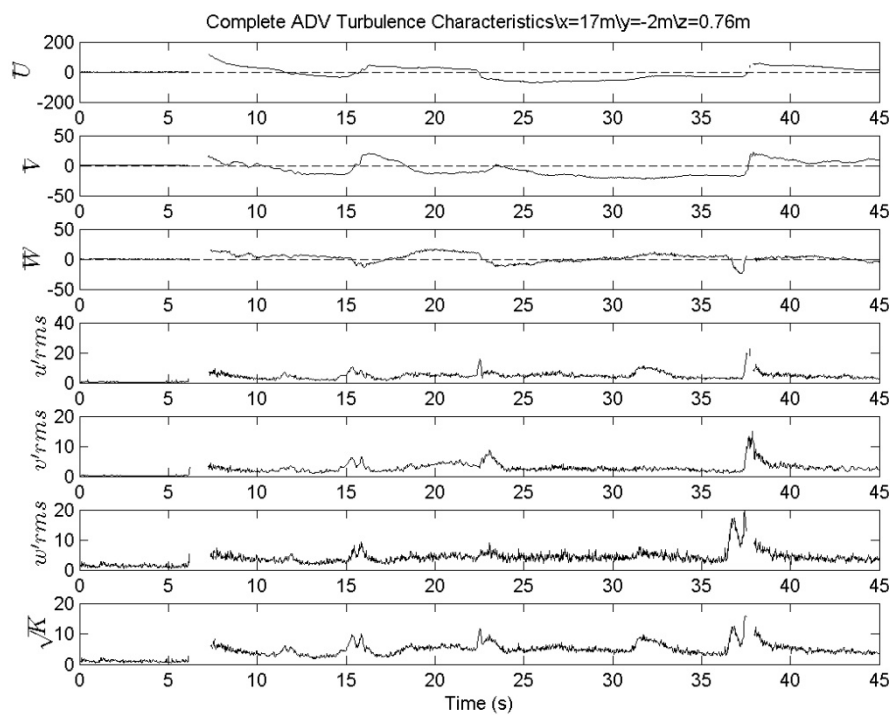
Figure 90:  Mean velocity, RMS turbulence, and $\sqrt{K}$ (cm/s) of ADV at X=11.5m, Y=6m, Z=0.45m.
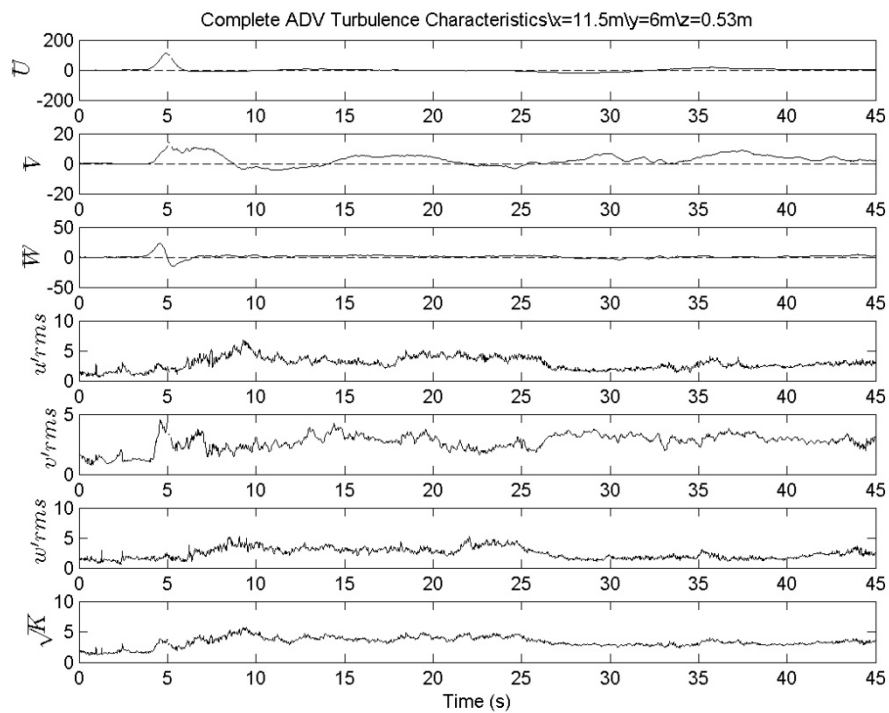


Figure 91:  Mean velocity, RMS turbulence, and $\sqrt{K}$ (cm/s) of ADV at X=11.5m, Y=6m, Z=0.53m.
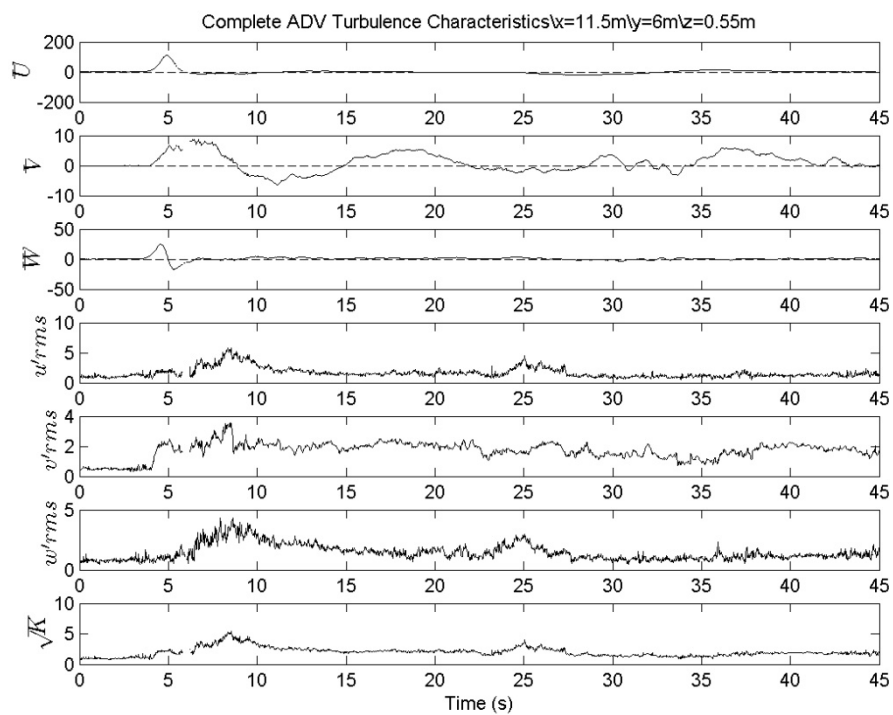
Figure 92:  Mean velocity, RMS turbulence, and $\sqrt{K}$ (cm/s) of ADV at X=11.5m, Y=6m, Z=0.55m.
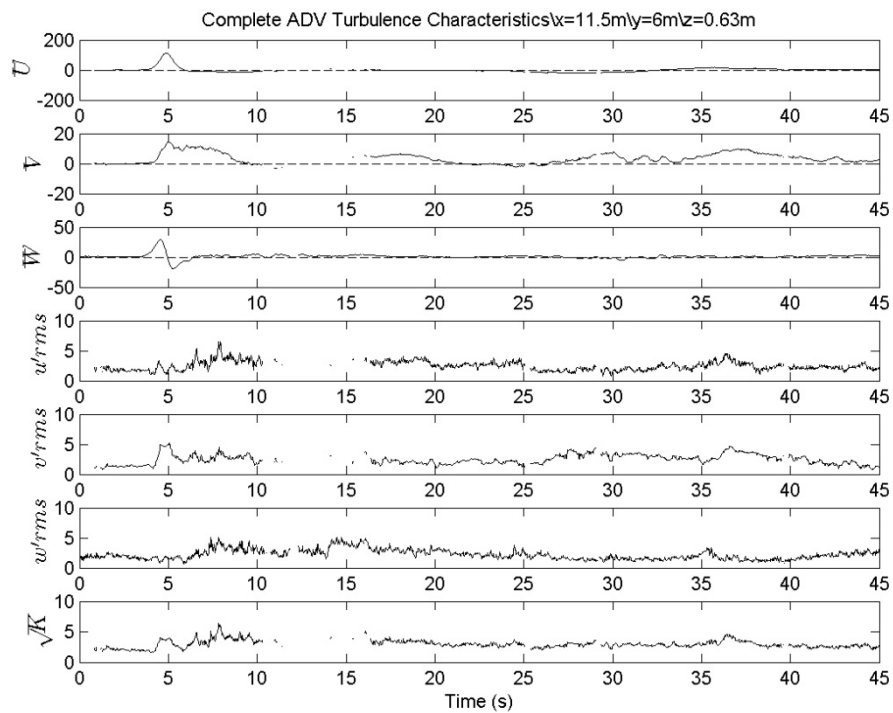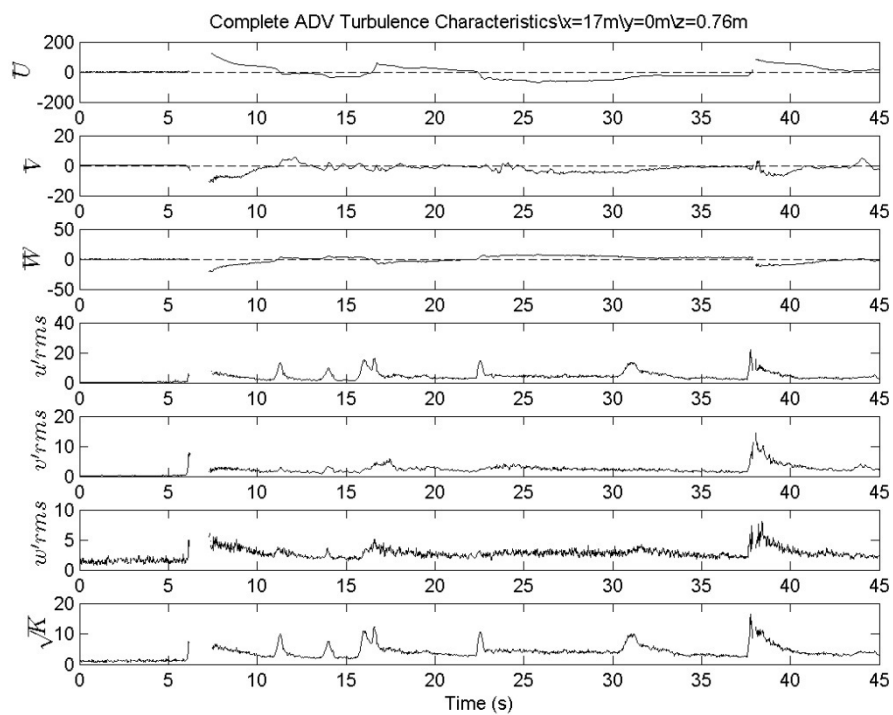


Figure 93:  Mean velocity, RMS turbulence, and $\sqrt{K}$ (cm/s) of ADV at X=11.5m, Y=6m, Z=0.63m.
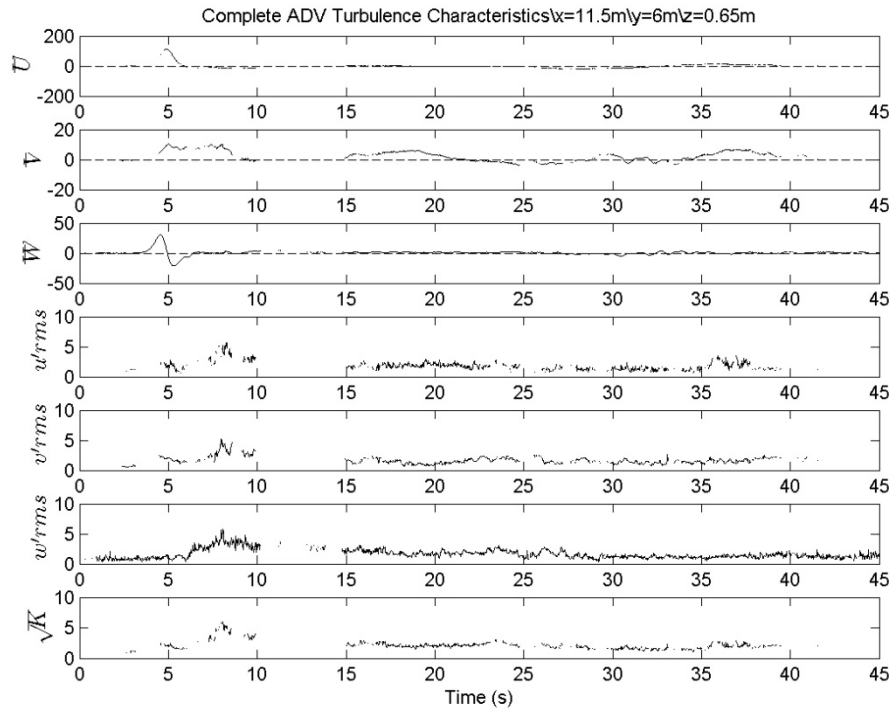
Figure 94:  Mean velocity, RMS turbulence, and $\sqrt{K}$ (cm/s) of ADV at X=11.5m, Y=6m, Z=0.65m.
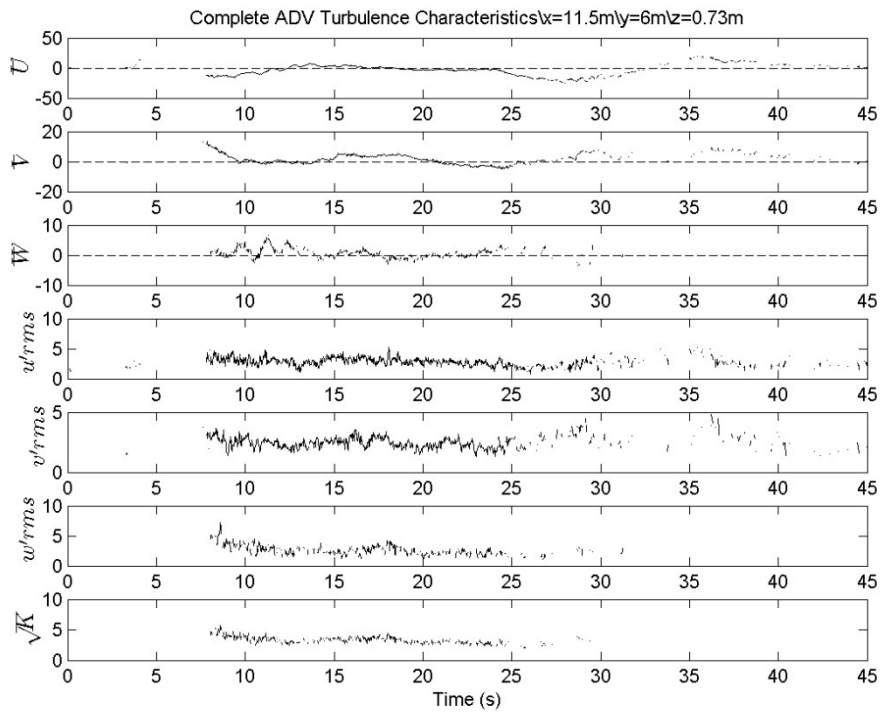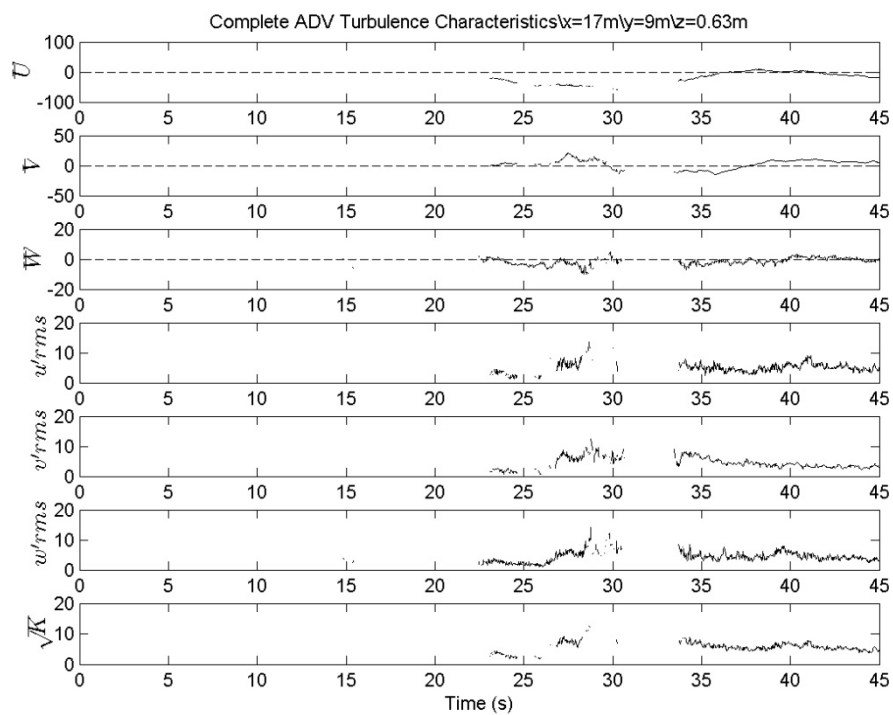


Figure 95:  Mean velocity, RMS turbulence, and $\sqrt{K}$ (cm/s) of ADV at X=11.5m, Y=6m, Z=0.73m.
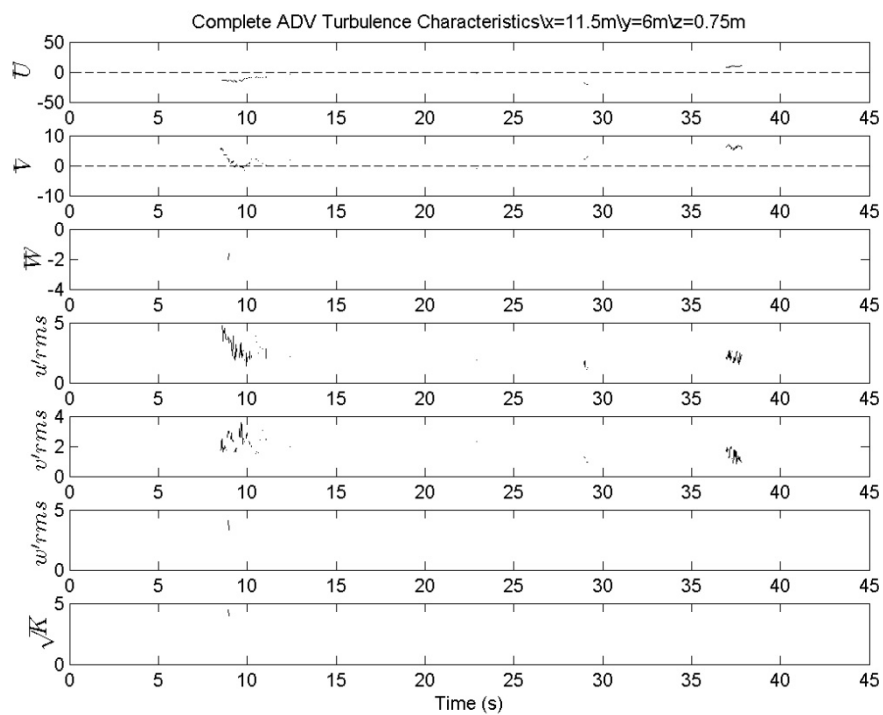
Figure 96:  Mean velocity, RMS turbulence, and $\sqrt{K}$ (cm/s) of ADV at X=11.5m, Y=6m, Z=0.75m.
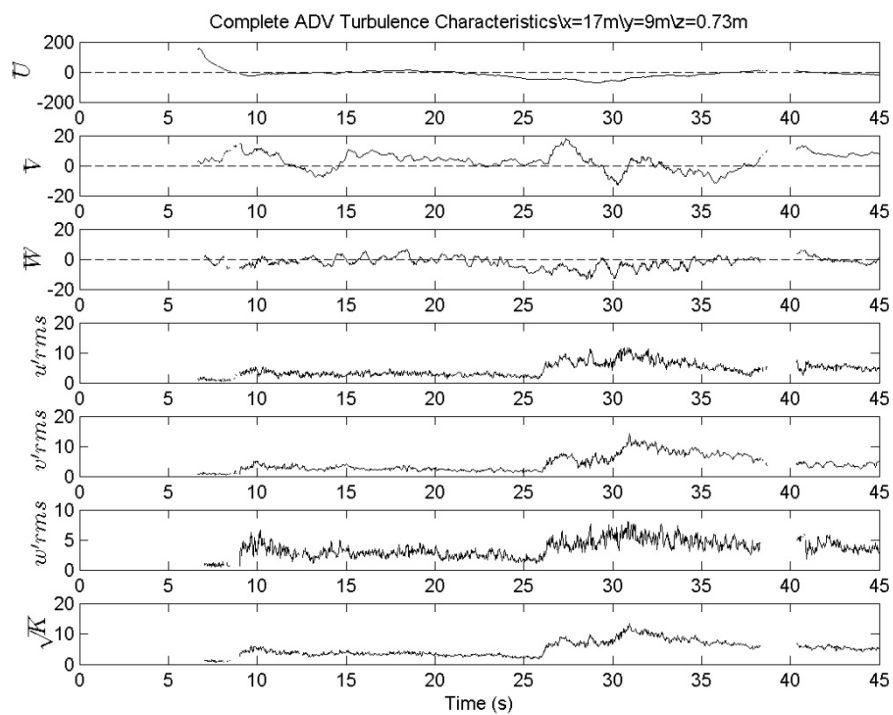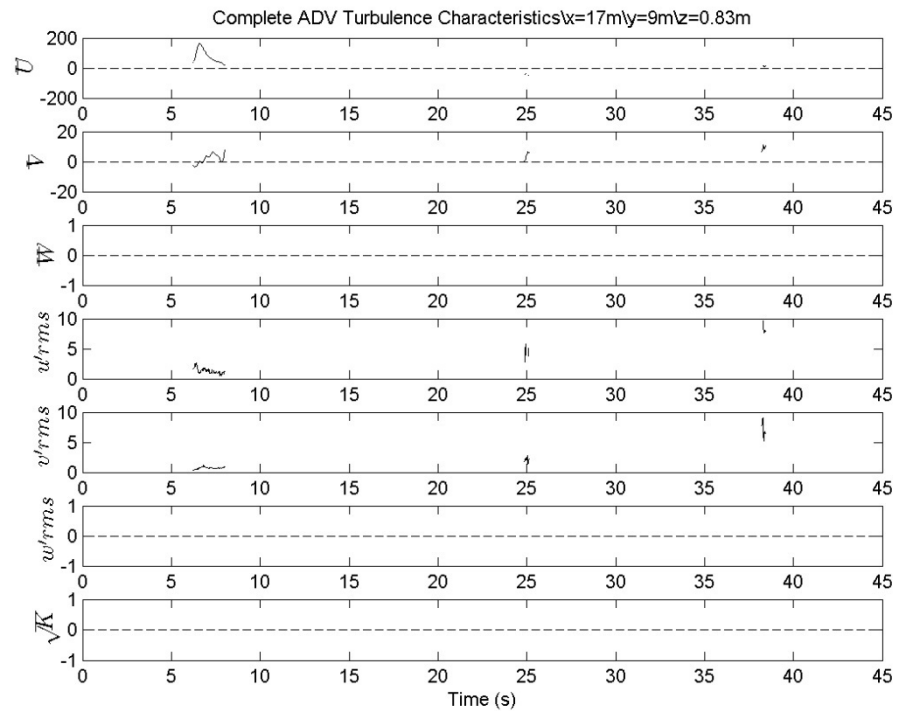


Figure 97:  Mean velocity, RMS turbulence, and $\sqrt{K}$ (cm/s) of ADV at X=13.0m, Y=0m, Z=0.75m.

Figure 98:  Mean velocity, RMS turbulence, and $\sqrt{K}$ (cm/s) of ADV at X=15.0m, Y=-2m, Z=0.76m.



Figure 99:  Mean velocity, RMS turbulence, and $\sqrt{K}$ (cm/s) of ADV at X=15.0m, Y=0m, Z=0.76m.
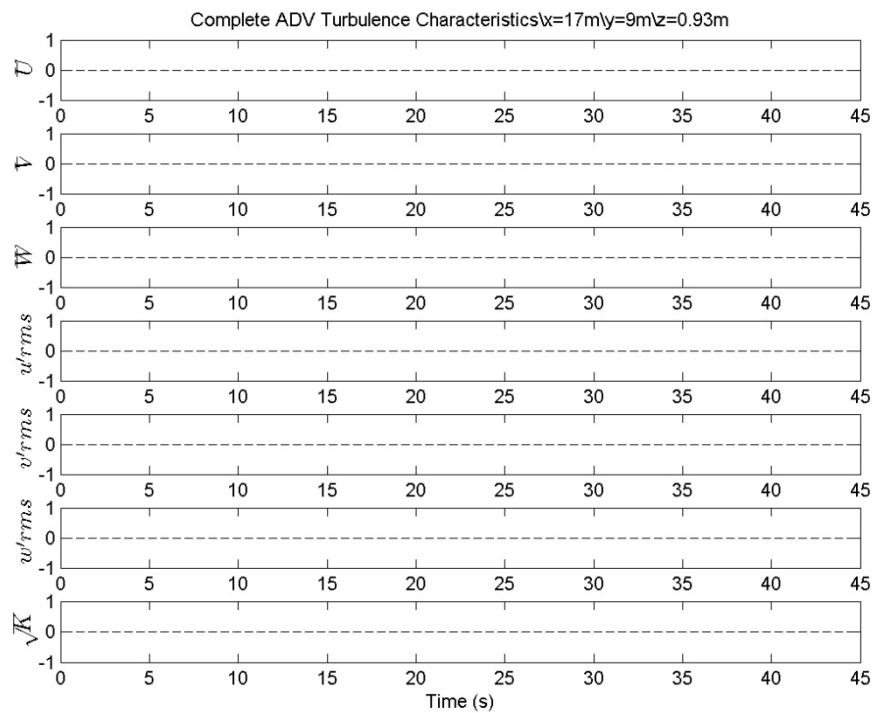
Figure 100: Mean velocity, RMS turbulence, and $\sqrt{K}$ (cm/s) of ADV at X=15.0m, Y=6m, Z=0.55m.



Figure 101: Mean velocity, RMS turbulence, and $\sqrt{K}$ (cm/s) of ADV at X=15.0m, Y=6m, Z=0.65m.

Figure 102:  Mean velocity, RMS turbulence, and $\sqrt{K}$ (cm/s) of ADV at X=15.0m, Y=6m, Z=0.75m.



Figure 103:  Mean velocity, RMS turbulence, and $\sqrt{K}$ (cm/s) of ADV at X=15.0m, Y=6m, Z=0.85m.

Figure 104:  Mean velocity, RMS turbulence, and $\sqrt{K}$ (cm/s) of ADV at X=15.0m, Y=9m, Z=0.43m.



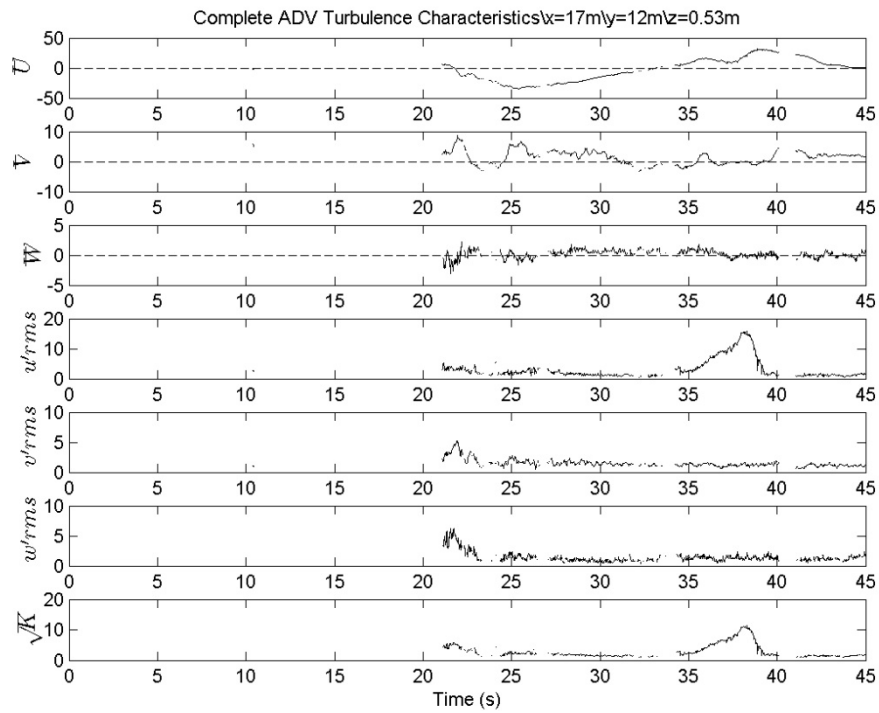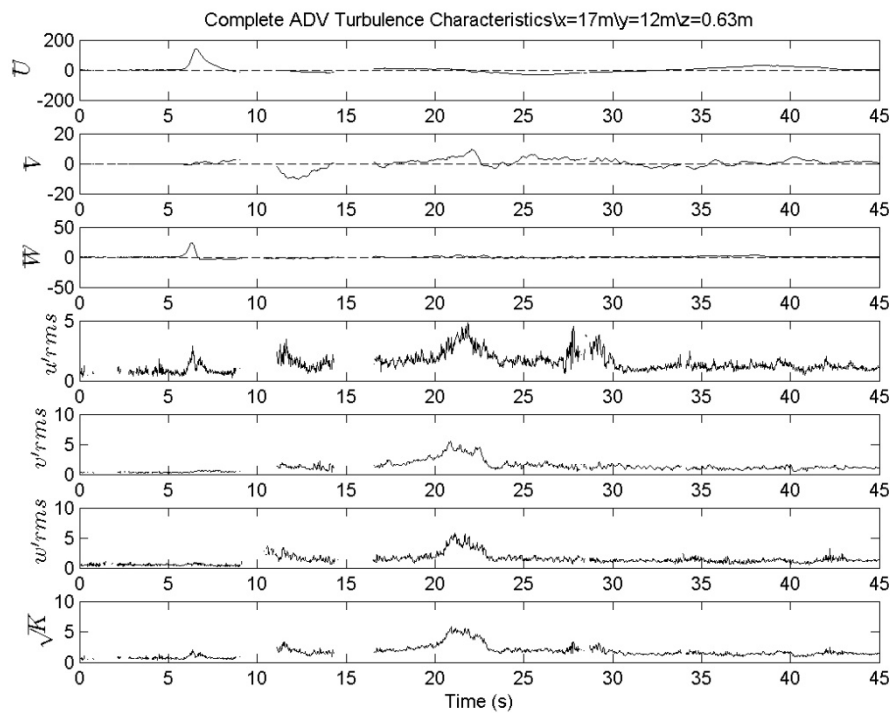Figure 105:  Mean velocity, RMS turbulence, and $\sqrt{K}$ (cm/s) of ADV at X=15.0m, Y=9m, Z=0.53m.

Figure 106:  Mean velocity, RMS turbulence, and $\sqrt{K}$ (cm/s) of ADV at X=15.0m, Y=9m, Z=0.63m.
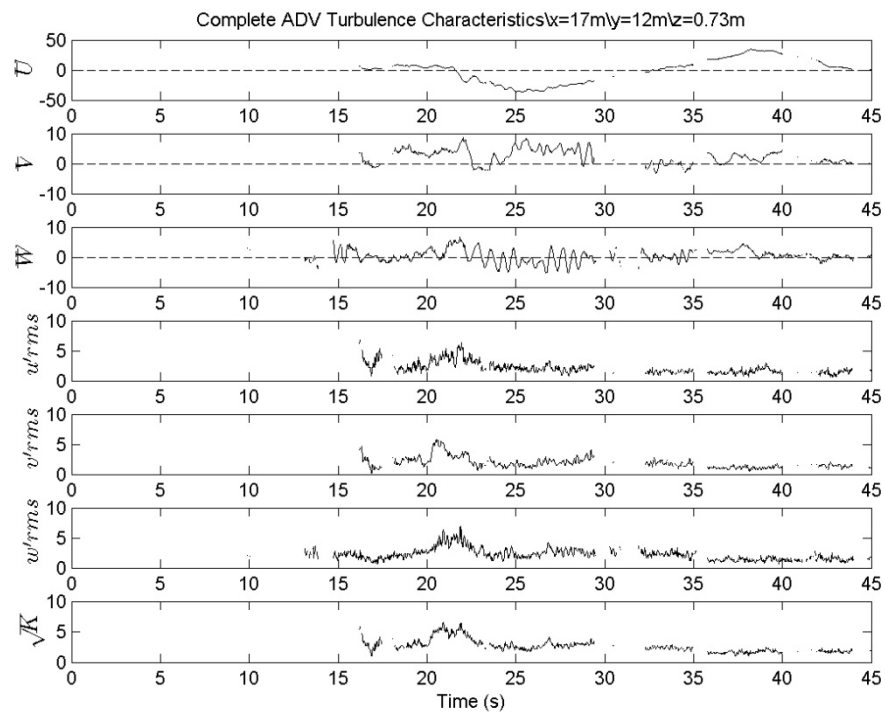


Figure 107:  Mean velocity, RMS turbulence, and $\sqrt{K}$ (cm/s) of ADV at X=15.0m, Y=9m, Z=0.73m.

Figure 108:  Mean velocity, RMS turbulence, and $\sqrt{K}$ (cm/s) of ADV at X=17.0m, Y=-9m, Z=0.51m.



Figure 109:  Mean velocity, RMS turbulence, and $\sqrt{K}$ (cm/s) of ADV at X=17.0m, Y=-5m, Z=0.74m.

Figure 110:  Mean velocity, RMS turbulence, and $\sqrt{K}$ (cm/s) of ADV at X=17.0m, Y=-2m, Z=0.76m.



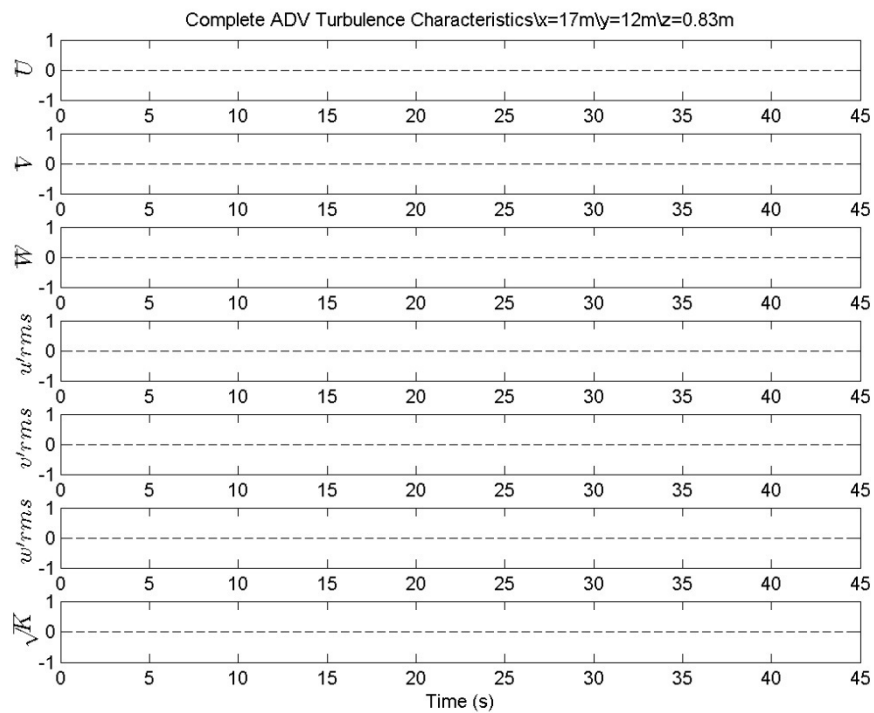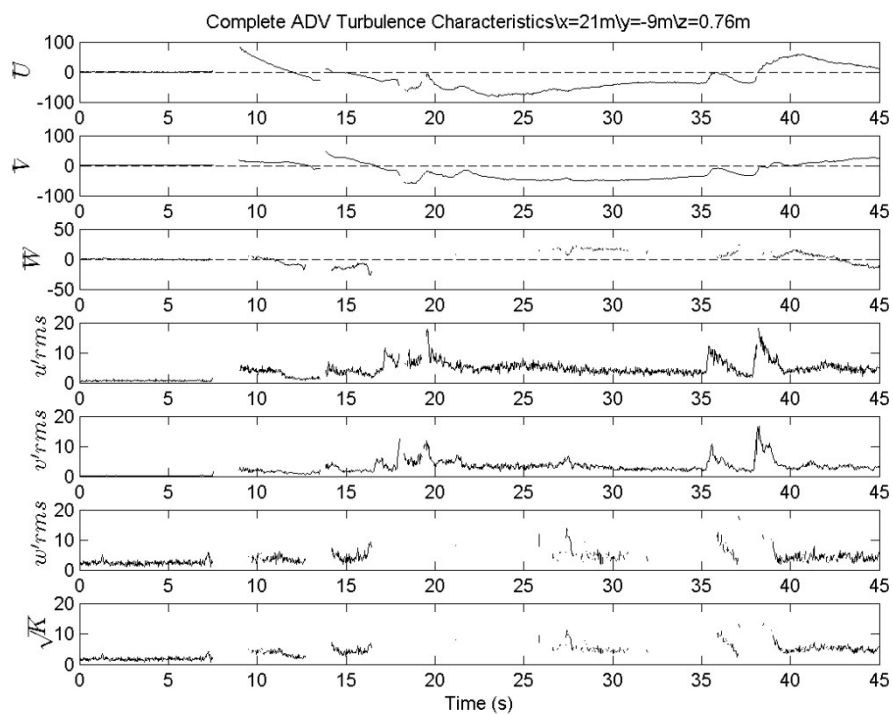Figure 111:  Mean velocity, RMS turbulence, and $\sqrt{K}$ (cm/s) of ADV at X=17.0m, Y=0m, Z=0.76m.

Figure 112: Mean velocity, RMS turbulence, and $\sqrt{K}$ (cm/s) of ADV at X=17.0m, Y=9m, Z=0.63m.
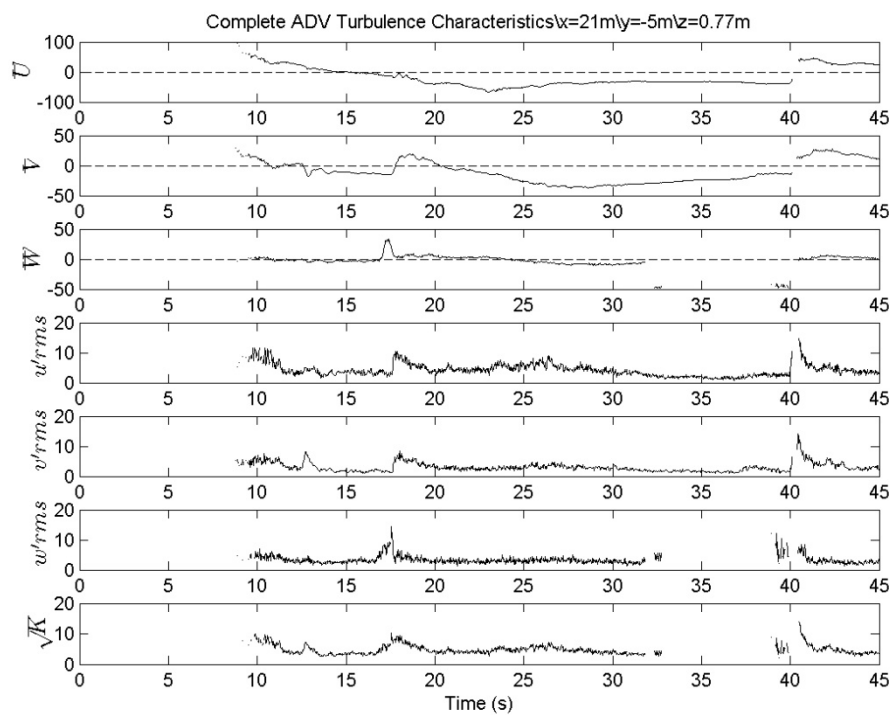


Figure 113: Mean velocity, RMS turbulence, and $\sqrt{K}$ (cm/s) of ADV at X=17.0m, Y=9m, Z=0.73m.

Figure 114:  Mean velocity, RMS turbulence, and $\sqrt{K}$ (cm/s) of ADV at X=17.0m, Y=9m, Z=0.83m.
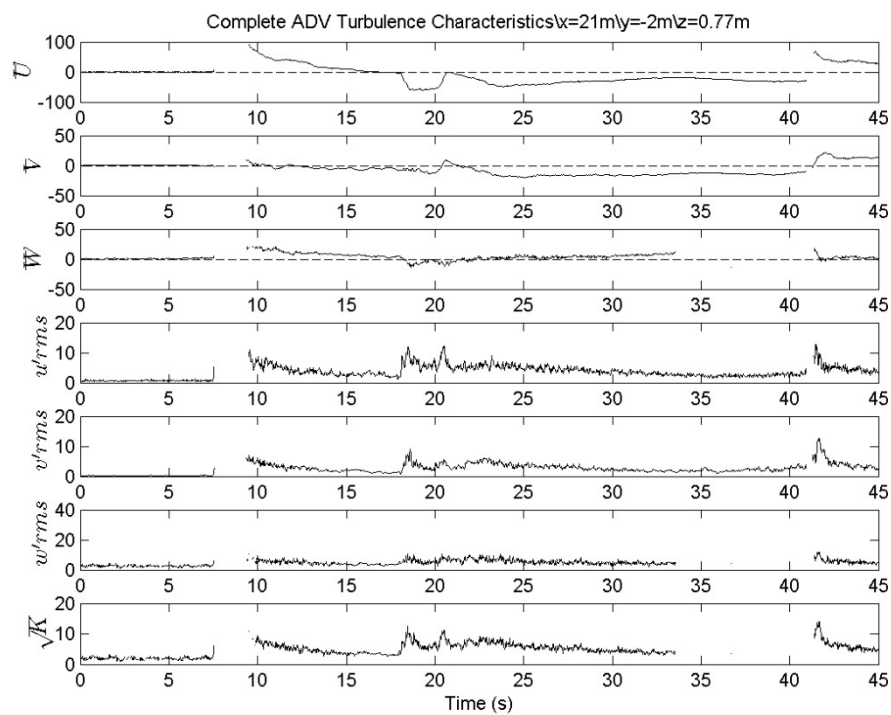


Figure 115:  Mean velocity, RMS turbulence, and $\sqrt{K}$ (cm/s) of ADV at X=17.0m, Y=9m, Z=0.93m.

Figure 116:  Mean velocity, RMS turbulence, and $\sqrt{K}$ (cm/s) of ADV at X=17.0m, Y=12m, Z=0.53m.



Figure 117:  Mean velocity, RMS turbulence, and $\sqrt{K}$ (cm/s) of ADV at X=17.0m, Y=12m, Z=0.63m.

Figure 118:  Mean velocity, RMS turbulence, and $\sqrt{K}$ (cm/s) of ADV at X=17.0m, Y=12m, Z=0.73m.



Figure 119:  Mean velocity, RMS turbulence, and $\sqrt{K}$ (cm/s) of ADV at X=17.0m, Y=12m, Z=0.83m.

Figure 120: Mean velocity, RMS turbulence, and $\sqrt{K}$ (cm/s) of ADV at X=21.0m, Y=-9m, Z=0.76m.



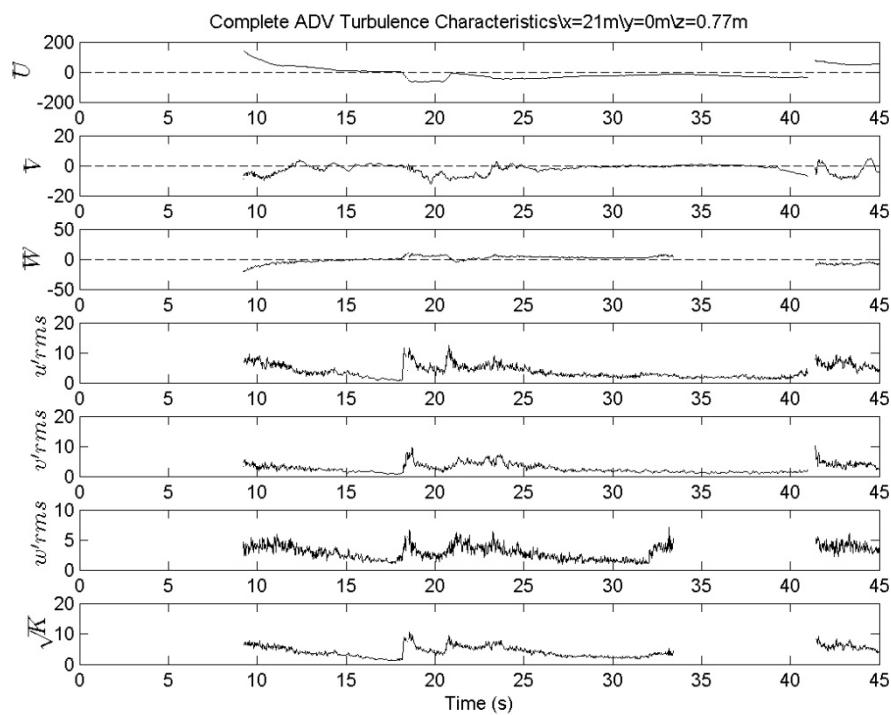Figure 121: Mean velocity, RMS turbulence, and $\sqrt{K}$ (cm/s) of ADV at X=21.0m, Y=-5m, Z=0.77m.

Figure 122: Mean velocity, RMS turbulence, and $\sqrt{K}$ (cm/s) of ADV at X=21.0m, Y=-20m, Z=0.77m.



Figure 123: Mean velocity, RMS turbulence, and $\sqrt{K}$ (cm/s) of ADV at X=21.0m, Y=0m, Z=0.77m.

# APPENDIX III: COMPLETE usWG PRESENTATION

The usWG timeseries presented below are organized moving in the positive longshore direction and in the positive cross-shore direction starting at X=23m, Y=0m and ending at X=39m, Y=10m
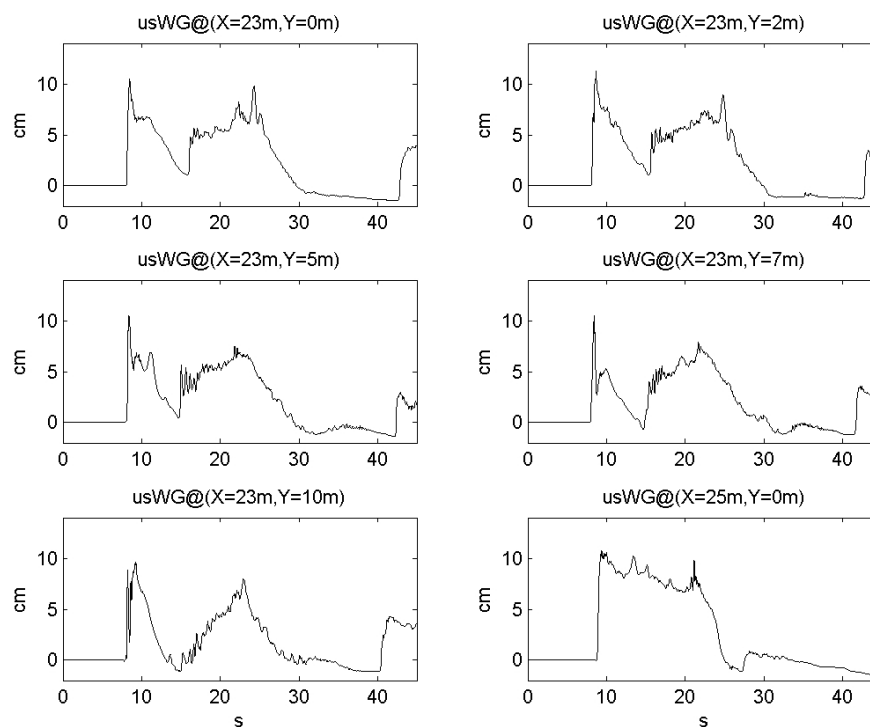


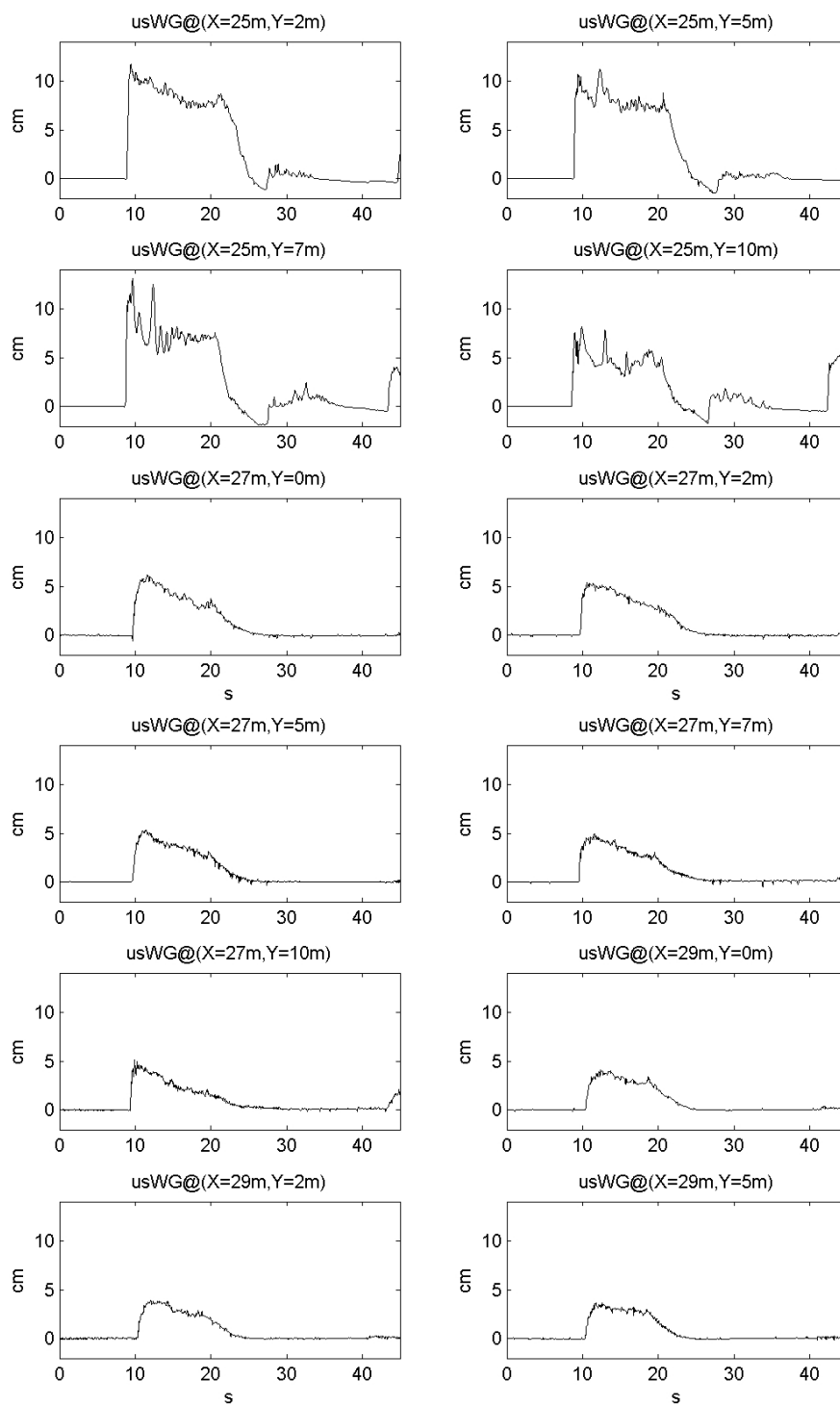Figure 124:  usWG timeseries including X=23m, Y=0m to X=25m, Y=0m.

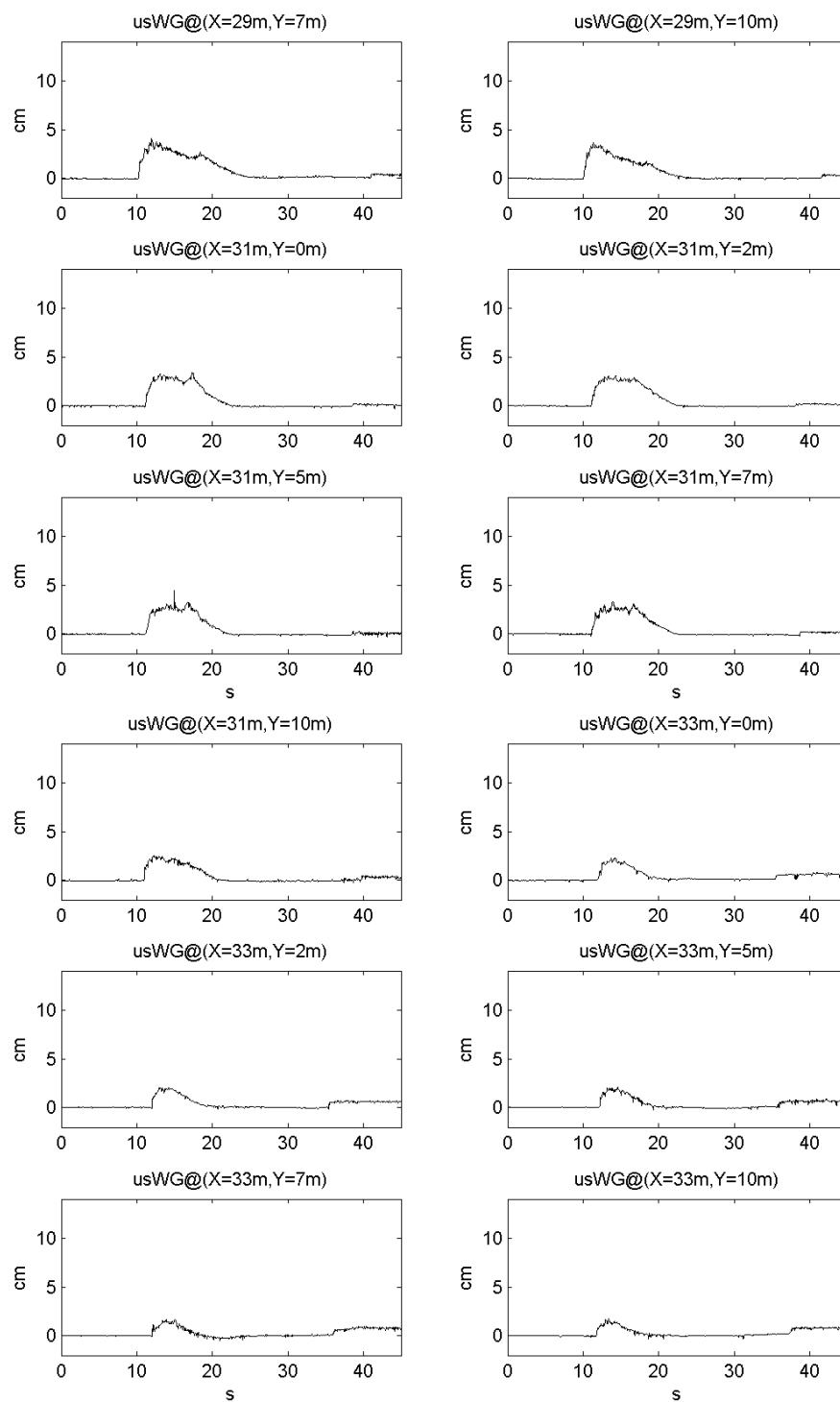Figure 125:  usWG timeseries including X=25m, Y=2m to X=29m, Y=5m.

Figure 126:  usWG timeseries including X=29m, Y=7m to X=33m, Y=10m.
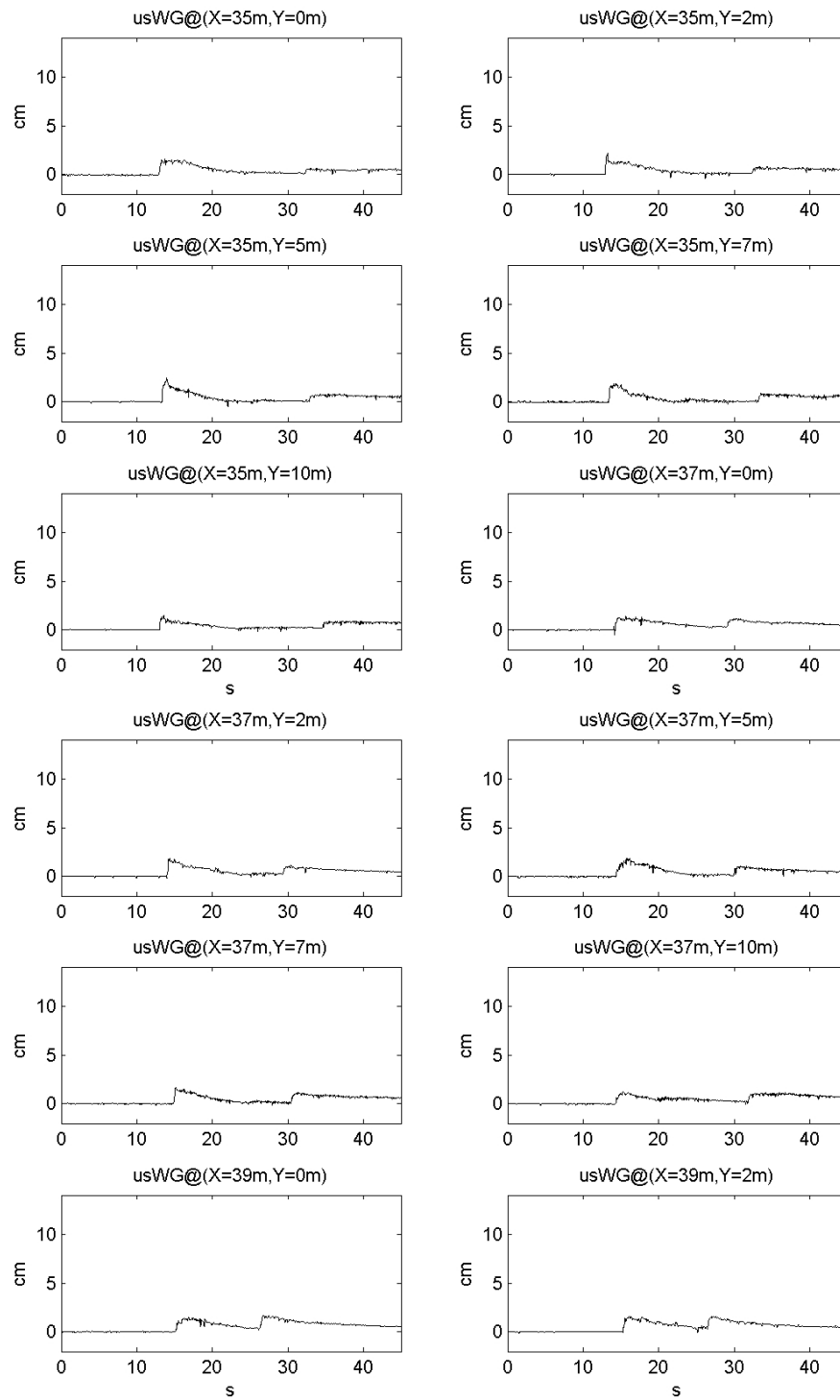
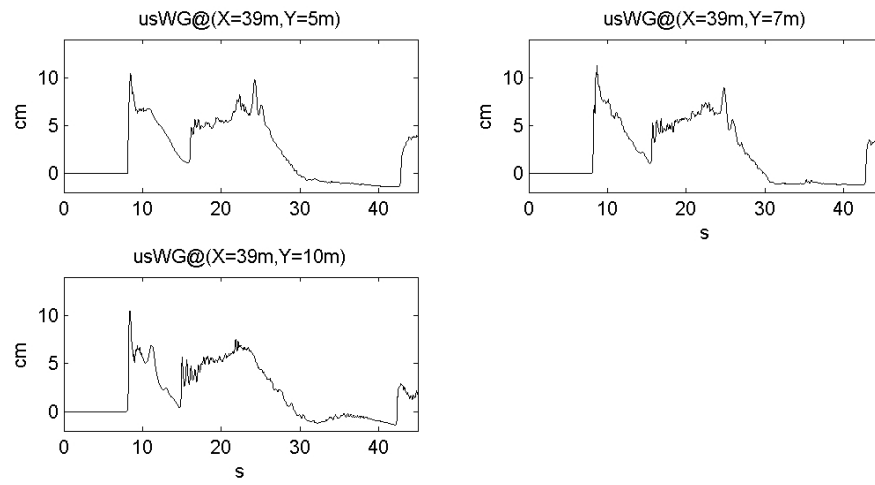Figure 127:  usWG timeseries including X=35m, Y=0m to X=39m, Y=2m.

Figure 128:  usWG timeseries including X=39m, Y=5m to X=39m, Y=10m.